Modeling polarimetric radar scattering from the lunar surface: Study on the effect of physical properties of the regolith layer

Wenzhe Fa, Mark Wieczorek, Essam Heggy

Modeling polarimetric radar scattering from the lunar surface: Study on the effect of physical properties of the regolith layer

Wenzhe Fa,[1] Mark A. Wieczorek,[1] and Essam Heggy[1,2]

Received 10 May 2010; revised 21 November 2010; accepted 15 December 2010; published 5 March 2011.

[1] A theoretical model for radar scattering from the lunar regolith using the vector radiative transfer theory for random media has been developed in order to aid in the interpretation of Mini-SAR data from the Chandrayaan-1 and Lunar Reconnaissance Orbiter missions. The lunar regolith is represented as a homogeneous fine-grained layer with rough upper and lower parallel interfaces that possesses embedded inclusions with a different dielectric constant. Our model considers five scattering mechanisms in the regolith layer: diffuse scattering from both the surface and subsurface, volume scattering from buried inclusions, and the interactions of scattering between buried inclusions and the rough interfaces (both the lunar surface and subsurface). Multiple scattering between buried inclusions and coherent backscatter opposite effect are not considered in the current model. The modeled radar scattering coefficients are validated using numerical finite difference time domain simulations and are compared with incident angle–averaged Earth-based radar observations of the Moon. Both polarized and depolarized radar backscattering coefficients and the circular polarization ratio (CPR) are calculated as a function of incidence angle, regolith thickness, surface and subsurface roughness, surface slope, abundance and shape of buried rocks, and the $FeO+TiO_2$ content of the regolith. Simulation results show that the polarized (opposite sense) radar echo strength at S and X bands is mostly dominated by scattering from the rough surface and buried rocks, while the depolarized (same sense) radar echo strength is dominated by scattering from buried rocks or ice inclusions. Finally, to explore the expected polarimetric signature of ice in the polar permanently shadowed areas, four parametric regolith models are considered and the possibility of detecting diffuse ice inclusions by the CPR is addressed. Our study suggests that detection of ice inclusions at the lunar poles using solely the CPR will be difficult given the small dielectric contrast between the regolith and ice.

Citation: Fa, W., M. A. Wieczorek, and E. Heggy (2011), Modeling polarimetric radar scattering from the lunar surface: Study on the effect of physical properties of the regolith layer, *J. Geophys. Res.*, *116*, E03005, doi:10.1029/2010JE003649.

1. Introduction

[2] Radar imaging is a powerful tool in lunar and planetary surface and subsurface exploration due to its ability to penetrate loose desiccated sediments such as dust and regolith, and such observations give information that is complementary to data obtained in the visible, infrared, and thermal infrared regimes. Since the early 1960s, a series of radar images of the Moon's nearside hemisphere have been obtained using the Earth-based radars at MIT's Lincoln Laboratory, Millstone Hill, Arecibo, Haystack and Goldstone observatory [e.g., *Evans and Pettengill*, 1963; *Thompson*, 1974, 1987; *Zisk et al.*, 1974; *Margot et al.*, 1999; *Campbell et al.*, 2007]. Extensive past work using these radar data includes studies of lunar impact crater morphology [*Thompson et al.*, 1974], mare lava flow ilmenite content [*Schaber et al.*, 1975], analysis of regional pyroclastic deposits [*Zisk et al.*, 1977], regolith composition and structure [*Campbell et al.*, 1997], mapping of the lunar surface topography [*Zisk*, 1972; *Margot et al.*, 1999] and estimation of the thickness of the lunar regolith layer [*Shkuratov and Bondarenko*, 2001].

[3] One particular interest is to use the received radar circular polarization ratio (CPR) to search for potential ice deposits where regions of the Moon are permanently shadowed near the poles [*Stacy et al.*, 1997; *Campbell et al.*, 2003]. Previously, the Clementine bistatic radar experiment reported finding evidence of ice in the vicinity of Shackleton crater [*Nozette et al.*, 1996], whereas Earth-based Arecibo radar observations suggested no significant differences between the sunlit and permanently shadowed walls of this crater [*Campbell et al.*, 2006]. Therefore, from a radar standpoint, the presence of ice deposits at the poles of the Moon is currently unresolved. In an attempt to reduce the ambiguities on these previous observations, two orbital miniature synthetic aperture radars (Mini-SAR and Mini-RF) on the Chandrayaan-1

[1] Institut de Physique du Globe de Paris, Sorbonne Paris Cité, Paris, France.
[2] Now at Jet Propulsion Laboratory, California Institute of Technology, Pasadena, California, USA.

0148-0227/11/2010JE003649

and Lunar Reconnaissance Orbiter (LRO) missions, have imaged the lunar surface (and will continue to do so over the next two years for LRO), with the principle objective of detecting the polarimetric signature of ice in the shallow lunar subsurface in the lunar polar areas [*Bussey et al.*, 2007; *Spudis et al.*, 2010].

[4] Knowledge about radar wave penetration, reflection, and scattering in the lunar regolith layer is critical to interpreting the received radar echoes and identifying potential ice deposits. Radar scattering from the lunar surface is complicated, since we must consider the transmission, attenuation, reflection and scattering of radar waves at both the lunar surface and base of the regolith layer, but also scattering from buried rocks and their interactions with the surface and base of the regolith. Using Earth-based observations of radar echoes and their variation as a function of the incidence angle, *Evans and Hagfors* [1964] proposed an empirical quasi-specular and diffuse component radar scattering model, where the quasi-specular component is the echo from relatively large and smooth surfaces that are perpendicular to the radar's line of sight and the diffuse component is attributed to scattering from wavelength-sized rocks, either on the surface or buried in lunar regolith. *Hagfors* [1964] modeled the quasi-specular component using the physical optics approximation (i.e., the Kirchhoff approach, which assumes that the radius of curvature of the surface relief is large with respect to the incident radar wavelength). *Hagfors* [1967] pointed out that rocks were responsible for the diffuse scattering component, and that their nonspherical shape led to the observed partial polarization. *Burns* [1969] suggested that most of the scattering resulted from single scattering by rocks that were either on the lunar surface or buried in the regolith. *Thompson et al.* [1970] modeled the single scattering behavior of rocks using Mie theory and suggested that models with single scattering by surface rocks or multiple scattering between buried rocks were capable of accounting for several observed properties of the diffuse component. *Pollack and Whitehill* [1972] used Mie scattering theory and the matrix doubling method [e.g., *Fung*, 1994, chap. 8] to calculate the single and multiple scattering from lunar rocks within the ejecta blanket of fresh young craters, and found that multiple scattering made a significant contribution to the partial depolarization of the reflected signal, while single scattering was also very important. Based on numerical simulations of radio wave scattering by rocks that were buried, partly buried, or on top of the regolith using numerical finite difference time domain (FDTD) techniques, *Baron et al.* [1996] found that radar scattering from a buried rock would be much weaker than the case where the rock was resting on the surface, although under some conditions partially buried rocks could scatter more strongly than rocks fully exposed on the surface. Using a buried substrate model and the Mie scattering theory, *Campbell et al.* [1997] analyzed the influence on the 70 cm radar echoes from the abundance of rocks in the regolith, the regolith thickness, and the dielectric properties of the regolith and rocks. *Thompson et al.* [2011] used a two-component mixing model with quasi-specular and diffuse components to estimate the scattering differences associated with slopes, surface roughness and pure ice deposits, and proposed an empirical method for separating the enhanced diffuse scattering of the near-surface ice layer from that due to the rough surface and buried rocks.

[5] In this study, a theoretical model for radar scattering from the lunar regolith layer is developed using vector radiative transfer (VRT) theory of random media [*Tsang et al.*, 1985; *Jin*, 1994]. The lunar regolith layer is modeled as a homogeneous fine-grained layer possessing rough upper and lower interfaces with randomly embedded inclusions. Vector radiative transfer theory is used to give the quantitative relations between polarimetric radar echoes and the physical properties of the regolith layer. The integral equation method (IEM) for rough surface scattering [*Fung*, 1994, chap. 4] is used to calculate radar wave scattering and penetration at each rough interface. Biaxial ellipsoidal particles are used to model the buried rocks, with their scattering properties depending upon their orientation, size and shape. An iterative method is used to obtain the Mueller matrix solution of the VRT equation, which gives the fully polarimetric radar scattering coefficients for any transmit/receive polarization. The derived Mueller matrix solution contains five scattering mechanisms for the regolith layer: diffuse scattering from both the rough surface and the rough interface between the regolith and underlying bedrock, direct scattering from inclusions embedded in the regolith, and the interactions of scattering between inclusions and the rough upper and lower surfaces of the regolith layer.

[6] Our modeled radar scattering coefficients are validated by numerical finite difference time domain (FDTD) simulations of radar wave propagation and are compared with incident angle–averaged Earth-based radar observation of the Moon. Polarimetric radar scattering from the lunar surface, as well as CPRs, are calculated using the VRT model as a function of incidence angle, regolith thickness, surface and subsurface roughness, surface slope, abundance and shape of buried rocks, and $FeO+TiO_2$ content in regolith, among other parameters. Finally, the possibility to detect ice inclusions in the polar permanently shadowed areas of the Moon using radar data is analyzed and discussed using our validated VRT model.

[7] The principal distinction between our radar scattering model using VRT theory and other previous models is that our model is an analytical model based on physical wave propagation principles, whereas most previous models are empirical in nature. The most widely used approach makes use of the physical optics approximation for rough surface scattering [*Hagfors*, 1964]; while not empirical, this model cannot take into account volume scattering from buried rocks, nor the interactions between a rough surface and the buried rocks. Numerical approaches (such as FDTD or the Method of Moments [e.g., *Harrington*, 1993]) can give a rigorous solution for complex problems, but the extensive computation usually only allows a limited number of scenarios to be investigated. In addition, our model is a fully polarimetric scattering model for both monostatic and bistatic radar observations, which allows us to calculate both the backscattering and bistatic radar scattering coefficient for any desired transmit/receive polarization.

[8] In section 2, we introduce a two-layer model of the lunar surface and discuss the parameters that can affect radar echoes, such as regolith thickness, regolith bulk density, surface roughness, dielectric constant, and the size frequency distribution of buried inclusions. The vector radiative

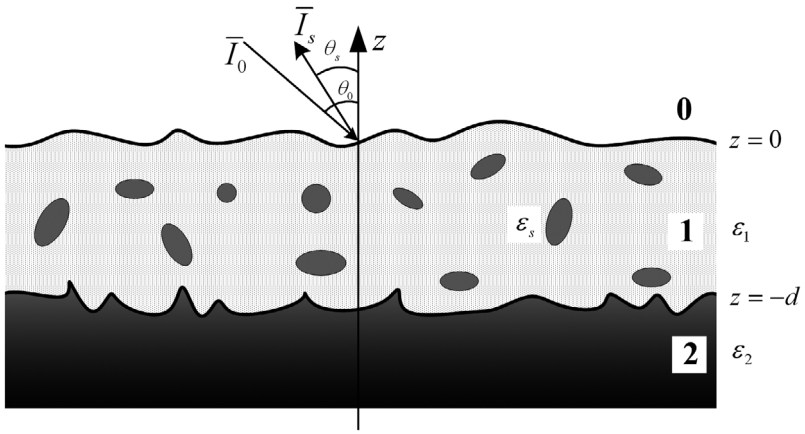

Figure 1. Schematic diagram of the lunar surface that consists of a regolith, embedded rocks, and underlying bedrock. The regolith thickness is d, the roughness of the lunar surface and of the interface between the regolith and bedrock is described by RMS heights and correlation lengths, δ_1 and l_1 for the surface, and δ_2 and l_2 for the subsurface, respectively. Buried inclusions are described by their shape, size, orientation, and fractional volume. The dielectric permittivity of the regolith, buried inclusions, and the underlying bedrock are ε_1, ε_s, and ε_2, respectively. The Stokes vector $\bar{I}_i$ with associated incidence angle θ_i represents the intensity and polarization state of the incident radar wave, $\bar{I}_s$ represents the intensity and polarization state of the scattered radar wave with scattering angle θ_s. Azimuthal scattering angle shown here is $\phi_s = 180°$.

transfer (VRT) equation for radar scattering from the lunar surface is given in section 3, and the Mueller matrix solution is then derived using an iterative method, from which radar scattering coefficients and the CPR can be calculated analytically. A tilted regolith model is also introduced in order to take into account the influence of large-scale surface slopes. In section 4, our radar scattering model is validated by finite difference time domain (FDTD) numerical simulations of radar wave propagation using the same input parameters. In section 5, we compare our model predictions with incident angle–averaged Earth-based radar observations of the Moon. Polarimetric radar scattering coefficients from the lunar surface, including CPRs, are calculated and discussed as a function of regolith properties in section 6. To explore the expected polarimetric signature of ice in the polar permanently shadowed areas of the Moon using radar, four parametric regolith models are considered and the possibility of detecting ice inclusions by radar data is analyzed and discussed using our VRT model in section 7. In section 8, limitations of our radar scattering model are discussed and its future applications in lunar exploration are presented. Several of the more mathematical aspects of this paper, including the rough surface scattering matrix based on IEM, some aspects of our Mueller matrix derivation, and effects of large surface slopes are presented in Appendices A, B, C and D, respectively.

2. Two-Layer Lunar Surface Model

[9] Previous investigations have shown that, with few exceptions, almost the entire lunar surface consists of a regolith layer that completely covers the underlying bedrock [e.g., *McKay et al.*, 1991]. In general, the median particle size of the regolith is from 40 to 130 μm, with an average of 70 μm. These grain sizes are considerably smaller than radar observation wavelengths, allowing one to treat the regolith (excluding larger rocks) as a continuous medium. The lunar regolith is a byproduct of the continuous impact of large and small meteoroids with the lunar surface, and consists largely of fragmented materials such as a surface dust layer, unconsolidated rock materials, breccias, and glass fragments. The physical characteristics of the regolith not only provide important information concerning significant questions in lunar geology, but are also critical for quantifying potential resources for future lunar exploration (such as ice or helium-3) and engineering constrains for human outposts and rover trafficability.

[10] Figure 1 shows a schematic diagram of our simplified model of the lunar regolith that consists of a homogenous fine-grained layer of thickness d with embedded inclusions and whose surface and base are rough (a summary of the parameters in our model is given in Table 1). Though we will often refer to the embedded inclusions simply as "rocks," we emphasize that these could also be composed of ice. The complex dielectric permittivity of the regolith, inclusions and the underlying bedrock are indicated by ε_1, ε_s, and ε_2, respectively. The roughness of the surface and subsurface are characterized by their root mean square (RMS) height and correlation length, with δ_1 and l_1 for the surface and δ_2 and l_2 for the interface between the regolith and bedrock, respectively. The differential fractional volume of inclusions with radius r to $r + dr$, $df_s(r)$, or equivalently the differential number of the inclusions per unit volume $dn(r)$, is used to describe the population of inclusions in the regolith layer. These two quantities are related by the expression $df_s(r) = dn(r) \cdot v(r)$, where $v(r)$ is the volume of a single inclusion with radius r. Given the lower and upper bounds on the size of inclusions considered, the total fractional volume of the inclusions f_s (or the number of the inclusions per unit volume n) can be obtained by integrating $df_s(r)$ (or $dn(r)$) over r.

[11] The regolith layer has experienced continuous impacting by large and small meteoroids over billions of years and its thickness is estimated to vary from a few meters to

Table 1. Model Parameters

Parameters	Definition	Typical Value	Reference
d	regolith thickness	4–5 m for the maria, 10–15 m for the highlands	*McKay et al.* [1991]
δ_1, l_1	root mean square height and correlation length of surface	not available	
δ_2, l_2	root mean square height and correlation length of subsurface	not available	
$s_1 = \sqrt{2}\delta_1/l_1$	1-D root mean square slope of surface	2°–4° for the maira, 6°–8° for the highlands	*Tyler and Howard* [1973]
$s_2 = \sqrt{2}\delta_2/l_2$	1-D root mean square slope of subsurface	not available	
f_s	fractional volume of buried inclusions	0–0.1 based on rocks at the Surveyor landing sites	*Thompson et al.* [1970]
c, a	semimajor and semiminor axes of the buried inclusions	several mm to tens of cm	*Thompson et al.* [1970]
ε_1, ε_2, ε_s	dielectric constant of regolith, underlying bedrock, and rocks	bulk density and composition dependent	*Carrier et al.* [1991]
ε_{ice}	dielectric constant of ice	3.15 + i(0.0001–0.1)	*Cumming* [1952], *Evans* [1965], and *Ray* [1972]
ρ	regolith bulk density	1.3–2.0 g/cm^3	*Carrier et al.* [1991]
S	FeO+TiO_2 abundance of regolith	0–30 (wt. %)	*Lucey et al.* [2000], *Lawrence et al.* [2002], and *Prettyman et al.* [2006]

tens of meters [e.g., *McKay et al.*, 1991]. In general, the thickness of the regolith correlates with the age of the lunar surface: the older the age, the greater the thickness. Based on direct measurements made during the Apollo and Luna missions (such as from seismic experiments at the Apollo 11, 12, and 14–17 landing sites [*Nakamura et al.*, 1975] and multifrequency electromagnetic probing at the Apollo 17 landing site [*Strangway et al.*, 1975]), as well as studies of impact crater morphology and crater size-frequency distributions [*Oberbeck and Quaide*, 1967, 1968; *Quaide and Oberbeck*, 1968], the average thickness of the regolith is believed to be about 4–5 m in the mare and 10–15 m in the older highland regions [e.g., *McKay et al.*, 1991]. A study of Earth-based 70 cm radar data for the nearside of the Moon estimated that the regolith thickness varies from 1.5 to 10 m for the mare, and from 1 to 18 m for the highlands [*Shkuratov and Bondarenko*, 2001]. Recently, an analysis of the Chang-E 1 radiometer data suggested that the average thickness of the regolith is 4.5 m for the mare and 7.6 m for the equatorial highlands (<60° latitude) [*Fa and Jin*, 2010].

[12] Surface roughness at scales comparable to the illuminating radar wavelength is one of the most important factors that influence the radar echo. The statistical properties of a random rough surface are here described by the RMS height δ and the correlation length l (here defined using 1-D profiles), which determine the vertical and horizontal scale of the roughness for a given surface, respectively. Surface height variations as a function of horizontal scale are described by the correlation function, with some commonly used functions being the Gaussian correlation function, the exponential correlation function, and the 1.5-power correlation function [e.g., *Fung*, 1994, chap. 2; *Jin*, 2005, chap. 5 and 6]. For a Gaussian random rough surface for 1-D profiles, the RMS slope $s = \sqrt{2}\delta/l$ is often referred to as the representative statistical property of the roughness [e.g., *Jin*, 1994, chap. 9; *Tsang et al.*, 2000, chap. 9; *Shepard et al.*, 2001]. For an exponential correlation function, an analytic expression for the RMS slope does not exist [*Tsang et al.*, 2000, chap. 9]; for purposes of comparison, we will use the same relation as for Gaussian surfaces. The use of this Gaussian relationship for exponential surfaces does not affect our roughness scattering calculation using IEM, since this only requires the correlation length l and RMS height δ.

[13] The surfaces of the maria are relatively smooth since they are relatively young and contain only a few large impact craters. In contrast, the highlands are more rugged because they are older and have experienced a larger number of large impact events. Using bistatic radar observations during Apollo 14 and 15, *Tyler and Howard* [1973] suggested that the lunar surface is gently undulating with 1-D RMS slopes on the order of 2° to 4° in the maria and 6° to 8° in the highlands on decimeter to hundred meter scales.

[14] Subsurface roughness is another potential factor that could affect the received radar echo, and the magnitude of this effect depends upon the dielectric loss of the incident radar wave in the regolith, which correlates with both the FeO+TiO_2 content and regolith thickness. Unfortunately, little is known about the subsurface roughness and in this study the subsurface roughness is assumed to be of the same magnitude as that of the lunar surface.

[15] A rough surface can also be considered as a self-affine (fractal) surface, which means that the roughness (both the RMS height and correlation length) depends on the length scale over which it is measured [*Shepard et al.*, 2001]. Little is known about the scale dependence of the lunar surface roughness, though this will certainly change considerably following the analysis of data from recent and ongoing missions. Regardless, if the power spectrum of the surface relief (i.e., the Fourier transform of the surface autocorrelation function) were to be described by a self-affine fractal surface, radar scattering from such a surface could be calculated using the same approach as described in Appendix A.

[16] The cumulative size-frequency distribution of rocks at the lunar surface is available at certain locations from photographs taken at the Surveyor landing sites [see *Shoemaker and Morris*, 1968]. The differential volumetric rock population is obtained by means of Rosiwal's principle, which states that the fractional area covered by surface rocks equals the fractional volume occupied by buried rocks [*Rosiwal*, 1898]. Table 2 lists the power law fits of the rock populations at the Surveyor sites, where the first column is the

Table 2. Surface and Volumetric Size Distribution Functions of Rocks at the Surveyor Landing Sites[a]

Surveyor	$N(r)$ (m^{-2})	$dN(r)$ (m^{-3})	$dn(r)$ (m^{-4})	Upper Bound of Rock Size (m)
1	$5.4 \times 10^{-4} r^{-2.11}$	$1.1 \times 10^{-3} r^{-3.11}$	$8.6 \times 10^{-4} r^{-4.11}$	0.50
3	$1.2 \times 10^{-4} r^{-2.56}$	$3.0 \times 10^{-4} r^{-3.56}$	$2.2 \times 10^{-4} r^{-4.56}$	0.35
5	$2.2 \times 10^{-5} r^{-2.65}$	$5.9 \times 10^{-5} r^{-3.65}$	$4.4 \times 10^{-5} r^{-4.65}$	0.20
6	$9.9 \times 10^{-5} r^{-2.51}$	$2.5 \times 10^{-4} r^{-3.51}$	$1.9 \times 10^{-4} r^{-4.51}$	0.32
7, $r < 0.25$ m	$7.8 \times 10^{-3} r^{-1.82}$	$1.4 \times 10^{-2} r^{-2.82}$	$1.1 \times 10^{-2} r^{-3.82}$	1.74
7, $r > 0.25$ m	$9.1 \times 10^{-4} r^{-2.95}$	$2.7 \times 10^{-3} r^{-3.95}$	$2.0 \times 10^{-3} r^{-4.95}$	1.74

[a] $N(r)$ is the cumulative number of rocks per m^2 as a function of radius derived from *Shoemaker and Morris* [1968], $dN(r)$ is the differential number of rocks per m^2, and $dn(r)$ is the differential number of rocks per m^3, with radii are in meters. The lower bound of rock debris is 0.05 mm and the fourth column shows the upper bound of the rock size r. Both $N(r)$ and $dN(r)$ are commonly quoted incorrectly in the literature.

cumulative distribution of rock per m^2, $N(r)$, as a function of radius r that derived from *Shoemaker and Morris* [1968]. By differentiating $N(r)$ with respect to r, the second column shows the corresponding differential distribution of rock sizes per m^2, $dN(r)$. Finally, using Rosiwal's principle, the third column lists the differential number of rocks per m^3, $dn(r)$. The lower bound of the rock debris is 0.05 mm, and the fourth column lists the upper bound of the rock size r at each Surveyor landing site. We note both $N(r)$ and $dN(r)$ are often quoted incorrectly in the literature.

[17] Figures 2a and 2b show the total fractional volume of buried rocks $f_s(r_l \le r \le r_u)$ as a function of lower and upper bounds of the rocks sizes, where $r_u = 1$ m for Figure 2a and $r_l = 0.05$ m for Figure 2b. Though typical values of the fractional volume of buried rocks are between 0 and 0.02, the Surveyor 7 landing site is found to have a relatively larger number of buried rocks with a fractional volume above 0.1. Since the fractional volume of buried rocks is generally below 0.1 (except in the most extreme cases), multiple scattering between buried rocks in a lossy medium can be ignored [*Tsang et al.*, 1985, chap. 2; *Jin*, 1994, chap. 8]. For our calculations, based on these results, we will consider fractional volumes of rock between 0 and 0.1. (We note that this range might not be representative for ice inclusions in the permanently shadowed craters.)

[18] Rocks on the lunar surface and buried in the regolith are in general not spherical, as assumed in Table 2. Nevertheless, many studies have treated rocks as spheres since this is a relatively simple and tractable approach from the viewpoint of radar scattering [*Thompson et al.*, 1970; *Pollack and Whitehill*, 1972; *Campbell et al.*, 1997]. In this study, we will treat buried and surface rocks as nonspherical oblate or prolate spheroids, because nonspherical rock shapes could be a significant source of radar depolarization [*Hagfors*, 1967]. The sphericity is defined as the ratio of the semimajor and semiminor axes, c/a, where a value of unity is a sphere, values larger than unity are prolate spheroids (needles), and values smaller than unity represent oblate spheroids (flattened disks).

[19] We do not explicitly consider the effects of rocks lying on the lunar surface in this study, since it is not possible to calculate the scattering of partly buried rocks with our analytical approach. Indeed, the only method that can accurately model this is by direct numerical simulation [e.g., *Baron et al.*, 1996; *Ye and Jin*, 2010]. As an approximation, we will thus assume that the effect of rocks lying on a surface is equivalent to an increased surface roughness.

[20] Laboratory measurements of lunar regolith samples show that the real part of the dielectric permittivity, ε_1', is strongly dependent upon bulk density ρ and is largely independent of chemical composition [*Olhoeft and Strangway*, 1975]. Above 1 MHz, it is also independent of frequency and temperature variations within the range of expected lunar surface temperature variations (~90 to 400 K). The loss tangent, $\tan\delta \equiv \varepsilon_1''/\varepsilon_1'$, which is the ratio of the imaginary part ε_1'' to the real part ε_1' of the complex dielectric permittivity, is strongly dependent on the bulk density, composition (in particular, the abundance of ilmenite), frequency and temperature [*Olhoeft and Strangway*, 1975]. According to *Carrier et al.* [1991], the real part of the dielectric permittivity and the loss tangent of the lunar regolith can be expressed as

$$\varepsilon_1' = 1.919^{\rho} \tag{1a}$$

$$\tan\delta = 10^{0.038S + 0.312\rho - 3.260} \tag{1b}$$

where the bulk density, ρ, is given in g/cm^3 and S = FeO+TiO_2 is in wt. %. Based on the Apollo in situ mea-

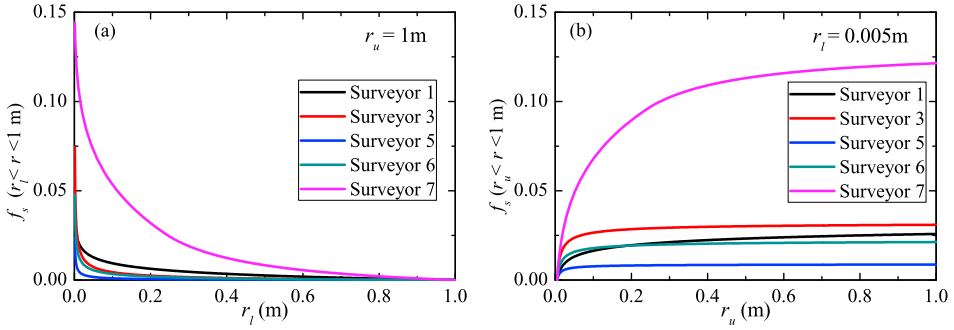

Figure 2. Fractional volume of buried rocks f_s as a function of (a) lower r_l and (b) upper r_u bounds of the rock sizes.

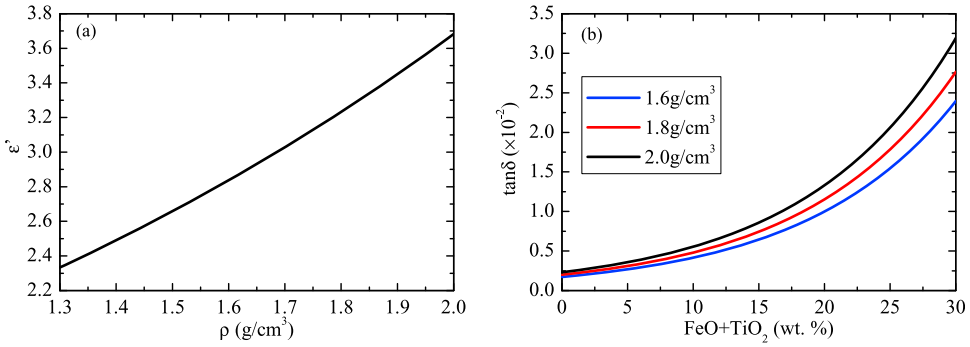

Figure 3. (a) Real part of dielectric permittivity of the lunar regolith as a function of bulk density from equation (1a) and (b) loss tangent of lunar regolith as a function of $FeO+TiO_2$ content in the regolith from equation (1b).

surements, the bulk density of the regolith varies from about 1.3 g/cm^3 at the lunar surface to a maximum value of about 1.9 g/cm^3 at a depth of 3 m [*Carrier et al.*, 1991]. The regolith bulk density is also expected to depend on composition, with a difference of a factor of about 1.2 between the mare and highlands, but for simplicity, we will here use a single value for the entire Moon. The $FeO+TiO_2$ content of the lunar regolith can be obtained using different remote sensing techniques, such as gamma ray, neutron, X-ray and optical spectroscopy. Both Clementine UV-VIS spectral reflectance and Lunar Prospector gamma ray spectrometer data have shown that the $FeO+TiO_2$ content of the lunar regolith varies from approximately 0 to 30 wt. % across the lunar surface [*Lucey et al.*, 2000; *Lawrence et al.*, 2002; *Prettyman et al.*, 2006]. For the polar areas of the Moon, there is little iron and titanium, and S is predicted to be less than 5 wt.% for the North Pole and about 10 wt.% for the South Pole. Finally, we note that the abundances of metallic iron produced by the space weathering process are too low to affect the dielectric properties of the regolith in any significant way.

[21] Figure 3a shows the variation of the real part of dielectric permittivity as a function of bulk density predicted from equation (1a), and Figure 3b shows the predicted loss tangent of the lunar regolith as a function of $FeO+TiO_2$ content for bulk densities of 1.6, 1.8 and 2.0 g/cm^3, respectively, from equation (1b). As the $FeO+TiO_2$ content of the lunar regolith increases, the loss tangent increases and this will act to increase the attenuation of the radar wave in the regolith.

[22] The penetration depth d_0 of radar waves in a homogeneous medium (i.e., the distance at which the incident radar power decreases by a factor of e^{-1}) is [e.g., *Kong*, 2008, chap. 3]

$$d_0 = \frac{\sqrt{\varepsilon'}}{2\pi\varepsilon''}\lambda = \frac{c\sqrt{\varepsilon'}}{2\pi f\varepsilon''} \tag{2}$$

where λ and f are the wavelength and frequency of the radar wave in free space, ε' and ε'' are the real and imaginary part of the dielectric permittivity of the medium, and c is the speed of light in vacuum. Figure 4 shows the penetration depth of radar waves as a function of $FeO+TiO_2$ content in the lunar regolith layer at 2.38 GHz and 7.14 GHz (the Mini-SAR frequencies for Chandrayaan-1 and LRO, respectively). It can be seen that this depth decreases as regolith $FeO+TiO_2$ content increases. The penetration depth at S band frequencies (2.38 GHz for Chandrayaan-1 and LRO Mini-SAR) could be larger than 5 m for low $FeO+TiO_2$ abundances and about 0.5 m for high $FeO+TiO_2$ abundances, while the penetration depth at X band frequencies (7.14 GHz for Mini-SAR) is about 2 m for low $FeO+TiO_2$ abundances and about 0.1 m for high $FeO+TiO_2$ abundances.

[23] The real part of the dielectric permittivity of rocks has been measured to lie between about 4 and 8 [*Carrier et al.*, 1991], while the imaginary part of the dielectric permittivity is strongly dependent upon the composition of the rock. For example, rocks with low titanium content can have a loss

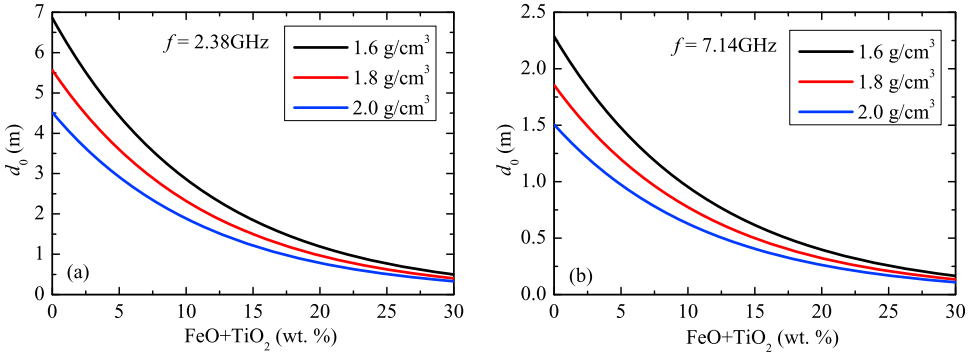

Figure 4. Penetration depth of radar waves as a function of $FeO+TiO_2$ content in the lunar regolith at (a) S and (b) X band frequencies.

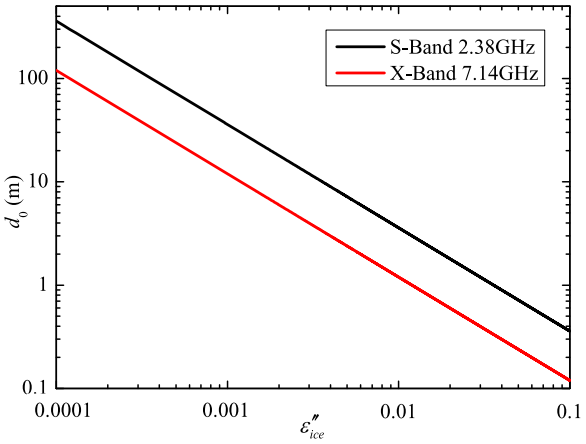

Figure 5. Penetration depth of radar waves as a function of the imaginary part of the dielectric permittivity of ice at S and X band frequencies, where the real part of the dielectric constant is assumed to be 3.2.

tangent as low as 0.0002 [*Olhoeft and Strangway*, 1975], which would give rise to penetration depths on the order of tens of meters at S and X band. The difference in dielectric properties of the lunar soils and rocks is simply due to the fact that the soils are a mixture of roughly equal parts rock and vacuum.

[24] If there is ice in the permanently shadowed areas near the lunar poles, the nature of this ice (coherent layers or particles) and its dielectric permittivity are the two factors that would most affect the received radar echoes. According to *Cumming* [1952], *Evans* [1965], and *Ray* [1972], the real part of the relative permittivity of pure freshwater ice is about 3.2 and the imaginary part varies from 10^{-4} to 0.05 at microwave frequencies. The dielectric properties of pure ice also depend on temperature and frequency, as given by the extended Debye formula of *Sadiku* [1985]. The dielectric properties of mixtures of freshwater ice, brine pockets, air bubbles, solid salts, rock particles, and organic and inorganic inclusions is rather complex and depends on the proportion of each constituent. Since brines, salts, and air are not expected to be present on the Moon in any significant abundance, rock particles and void space are probably the two major factors that could affect the effective dielectric constant of lunar ice. Figure 5 shows the penetration depth of radar waves (at both S band and X band frequencies) in a pure water-ice layer as a function of the imaginary part of the dielectric constant of ice. The penetration depth is seen to vary from several meters to several hundreds of meters, depending on the assumed value of the imaginary part of the dielectric permittivity.

[25] Note that the penetration depths in Figures 4 and 5 calculated from equation (2) are for homogeneous media. For a regolith with embedded particles such as rock or ice, the penetration depths will be less than those in Figures 4 and 5 because of additional scattering losses of the radar wave [see, e.g., *Heggy et al.*, 2006].

3. Mueller Matrix Solution of Vector Radiative Transfer Equation

[26] Electromagnetic wave propagation and scattering in a random medium are typically modeled using one of three approaches: vector radiative transfer (VRT) theory, analytic wave theory, or randomly rough surface scattering theory [*Tsang et al.*, 1985; *Jin*, 1994; *Fung*, 1994]. Vector radiative transfer theory is based on the principle of energy conservation, and is not from the Maxwell equations. In particular, though it takes into account the addition of intensity, it cannot account for wave coherence such as occurs in the coherent backscatter opposition effect [e.g., *Hapke*, 1990]. Analytic wave theory is developed from the Maxwell equations, and can explain wave coherence phenomena. Both vector radiative transfer theory and analytic wave theory treat the case of random heterogeneous media, though VRT is usually used for the case of discrete scatterers and analytic wave theory is used for random medium with dielectric fluctuations. Random rough surface scattering theory treats the case of scattering from an random interface between two different homogenous media, and analytical approaches to solving this problem mainly include the Kirchhoff approximation (physical optics), small perturbation method (SPM), and the integral equation method (IEM) (see Appendix A). Numerical approaches to electromagnetic waves propagation and scattering in random media usually include method of moments (MoM), finite element method (FEM), and finite difference time domain (FDTD) techniques [*Fung*, 1994; *Tsang et al.*, 2000; *Jin*, 2005].

[27] Given that the lunar regolith layer is well approximated by a homogenous fine-grained layer possessing rough upper and lower interfaces with randomly buried discrete inclusions, VRT theory combined with IEM for rough surface scattering is a good choice for modeling radar scattering from the lunar surface. Analytical wave theory requires knowledge of the correlation function of the dielectric permittivity in the regolith, and this is not easily constrained from in situ surface measurements. Besides, to our knowledge, analytic wave theory cannot take into account scattering from a rough surface, and its mathematical complexity prevents its application to nonspherical particles. Although numerical approaches (such as MoM, FEM, and FDTD) can give a rigorous results by directly solving the Maxwell equations, the large storage requirements and computational times often only allow one to investigate a limited range of situations, even with a modern computer.

[28] In this study, we use vector radiative transfer (VRT) theory of random media to quantify radar scattering from the lunar regolith layer. Our method is a physical-mathematical method that includes scattering, absorption and transmission of polarized electromagnetic intensity through random scatterers, and improves upon most previous radar scattering models applied to the Moon that are largely empirical in nature.

3.1. VRT Equation and Mueller Matrix Solution

[29] For an elliptically polarized monochromatic electromagnetic wave $\overline{E} = \hat{v}E_v + \hat{h}E_h$, the four-column Stokes vector $\overline{I} = [I_v, I_h, U, V]$ is defined as [e.g., *Tsang et al.*, 1985, chap. 2; *Jin*, 1994, chap. 1]

$$\overline{I} = \begin{bmatrix} I_v \\ I_h \\ U \\ V \end{bmatrix} = \begin{bmatrix} \frac{1}{\eta}\left\langle |E_v|^2 \right\rangle \\ \frac{1}{\eta}\left\langle |E_h|^2 \right\rangle \\ \frac{2}{\eta}\mathrm{Re}\left\langle E_v E_h^* \right\rangle \\ \frac{2}{\eta}\mathrm{Im}\left\langle E_v E_h^* \right\rangle \end{bmatrix} \tag{3}$$

where E_v and E_h are the electric field of an electromagnetic wave with vertical ($\hat{v}$) and horizontal ($\hat{h}$) polarization, $\eta = \sqrt{\mu/\varepsilon}$ is the wave impedance of the medium in which the wave propagates, and μ and ε are the permeability and permittivity of the medium, respectively. In equation (3) the asterisk denotes the complex conjugate, the angular brackets denote the temporal average since the electromagnetic wave is usually quasi-monochromatic with E_v and E_h randomly fluctuating with time, and Re and Im indicate the real and imaginary components of a complex value. It has been proved that the amplitude, phase and polarization state of any elliptically polarized wave can be completely characterized by the Stokes vector [e.g., *Tsang et al.*, 1985; *Jin*, 1994; *Fung*, 1994].

[30] As a polarized radar wave with frequency f impinges upon the lunar surface, as shown in Figure 1, the VRT equation applicable to the lunar regolith is [e.g., *Tsang et al.*, 1985, chap. 2; *Jin*, 1994, chap. 1]

$$\cos\theta \frac{d}{dz}\bar{I}(\theta,\phi,z) = -\bar{\bar{\kappa}}_e(\theta,\phi,z)\cdot\bar{I}(\theta,\phi,z) + \int_0^{\pi} d\theta' \sin\theta' \cdot \int_0^{2\pi} d\phi' \bar{\bar{P}}(\theta,\phi;\theta',\phi',z)\cdot\bar{I}(\theta',\phi',z) \tag{4}$$

where the Stokes vector $\bar{I}(\theta, \phi, z)$ represents the intensity and polarization state of the radar wave beneath the lunar surface. In equation (4), the incidence angle θ is defined with respect to the vertical $\hat{z}$ axis, the azimuthal angle ϕ is defined in the plane perpendicular to the $\hat{z}$ axis and the extinction matrix $\bar{\bar{\kappa}}_e$ is expressed as

$$\bar{\bar{\kappa}}_e(\theta,\phi) = \frac{2\pi}{k} n \begin{bmatrix} 2\,\mathrm{Im}\langle f_{vv}^0\rangle & 0 & \mathrm{Im}\langle f_{vh}^0\rangle & -\mathrm{Re}\langle f_{vh}^0\rangle \\ 0 & 2\,\mathrm{Im}\langle f_{hh}^0\rangle & \mathrm{Im}\langle f_{hv}^0\rangle & \mathrm{Re}\langle f_{hv}^0\rangle \\ 2\,\mathrm{Im}\langle f_{hv}^0\rangle & 2\,\mathrm{Im}\langle f_{vh}^0\rangle & \mathrm{Im}\langle f_{vv}^0 + f_{hh}^0\rangle & \mathrm{Re}\langle f_{vv}^0 - f_{hh}^0\rangle \\ 2\,\mathrm{Re}\langle f_{hv}^0\rangle & -2\,\mathrm{Re}\langle f_{vh}^0\rangle & \mathrm{Re}\langle f_{hh}^0 - f_{vv}^0\rangle & \mathrm{Im}\langle f_{vv}^0 + f_{hh}^0\rangle \end{bmatrix} \tag{5}$$

where k is the wave number. The phase matrix $\bar{\bar{P}}$, which couples the incident Stokes vector $\bar{I}(\theta', \phi', z)$ to the scattered Stokes vector $\bar{I}(\theta, \phi, z)$, is expressed as

$$\bar{\bar{P}}(\theta_s,\phi_s;\theta_i,\phi_i) = n \begin{bmatrix} \langle |f_{vv}|^2\rangle & \langle |f_{vh}|^2\rangle & \mathrm{Re}\langle f_{vv} f_{vh}^*\rangle & -\mathrm{Im}\langle f_{vv} f_{vh}^*\rangle \\ \langle |f_{hv}|^2\rangle & \langle |f_{hh}|^2\rangle & \mathrm{Re}\langle f_{hv} f_{hh}^*\rangle & -\mathrm{Im}\langle f_{hv} f_{hh}^*\rangle \\ 2\,\mathrm{Re}\langle f_{vv} f_{hv}^*\rangle & 2\,\mathrm{Re}\langle f_{vh} f_{hh}^*\rangle & \mathrm{Re}\langle f_{vv} f_{hh}^* + f_{vh} f_{hv}^*\rangle & -\mathrm{Im}\langle f_{vv} f_{hh}^* - f_{vh} f_{hv}^*\rangle \\ 2\,\mathrm{Im}\langle f_{vv} f_{hv}^*\rangle & 2\,\mathrm{Im}\langle f_{vh} f_{hh}^*\rangle & \mathrm{Im}\langle f_{vv} f_{hh}^* + f_{vh} f_{hv}^*\rangle & \mathrm{Re}\langle f_{vv} f_{hh}^* - f_{vh} f_{hv}^*\rangle \end{bmatrix} \tag{6}$$

where n is the number of buried rocks per unit volume, $f_{pq}(\theta_s, \phi_s; \theta_i, \phi_i)$ (with $p, q = v, h$, where v is for vertical polarization and h is for horizontal polarization) are the scattering amplitude functions of a single scatterer that couples the incident electric field of the radar wave to the scattered electric field, and i and s indicate the incident and scattered directions. The scattering amplitude function depends on the size, shape and orientation of the scatterer as well as the frequency of the radar wave, and this could be obtained using an analytical approach for a simple scatterer (such as a sphere or cylinder) or numerical approaches (such as FDTD, MoM or System Transfer Operator approach (T-matrix)) for a complex or irregular scatterer. In this study, buried inclusions are modeled as biaxial ellipsoidal particles and their scattering amplitude function is calculated using the T-matrix approach under the Rayleigh approximation, which requires the scatterer to be smaller than one wavelength [*Tsang et al.*, 2000, chap. 2]. The superscript "0" in equation (5) indicates the forward scattering direction, and the angular brackets in equations (5) and (6) denote the average taken over all orientations of the buried nonspherical rocks. With our convention for the angles θ ($0 \le \theta \le \pi/2$) and ϕ ($0 \le \phi \le 2\pi$), (θ, ϕ) indicates the upward direction, whereas ($\pi - \theta$, ϕ) indicates the downward direction.

[31] The first term on the right hand side of equation (4) is the attenuation of the incident radar wave as it propagates through the lunar regolith layer, which includes both scattering and absorption attenuation, and the second term is the contribution of scattering from all directions to the scattering direction (θ, ϕ).

[32] The boundary conditions at $z = 0$ (the surface) and $z = -d$ (the base of the regolith) are

$$\bar{I}(\pi-\theta,\phi,z=0) = \int_0^{2\pi} d\phi' \int_0^{\pi/2} d\theta' \sin\theta' \bar{\bar{R}}_{10}(\theta,\phi;\theta',\phi')\cdot\bar{I}(\theta',\phi',z=0) + \int_0^{2\pi} d\phi' \int_0^{\pi/2} d\theta' \sin\theta' \bar{\bar{T}}_{01}(\theta,\phi;\theta',\phi')\cdot\bar{I}_i(\pi-\theta',\phi',z=0) \tag{7a}$$

$$\bar{I}(\theta,\phi,z=-d) = \int_0^{2\pi} d\phi' \int_0^{\pi/2} d\theta' \sin\theta' \bar{\bar{R}}_{12}(\theta,\phi;\theta',\phi')\cdot\bar{I}(\pi-\theta',\phi',z=-d) \tag{7b}$$

where equation (7a) indicates that the downward Stokes vector is the sum of the scattered Stokes vector of the upward wave at the interface of the regolith (media 1) and vacuum (media 0) and the transmitted Stokes vector of the incident wave through vacuum (media 0) to the regolith (media 1), and equation (7b) indicates that the upward Stokes vector is given by the scattering of the downward wave at $z = -d$. The angular integrals in equation (7) are required as a result of the diffuse scattering and transmission through the random rough interfaces at $z = 0$ and $z = -d$.

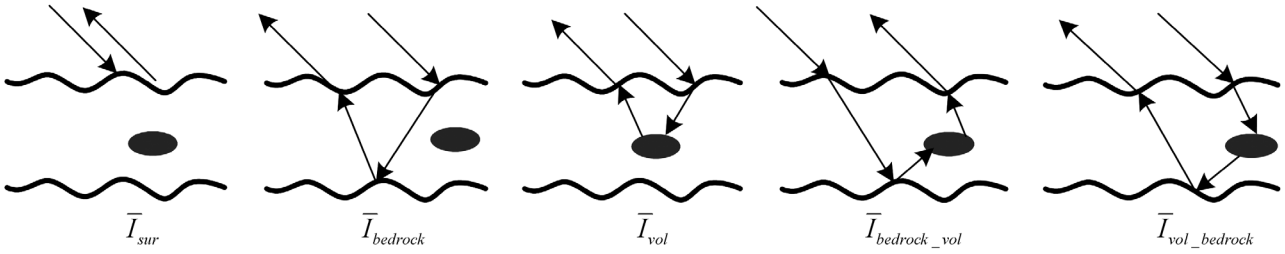

Figure 6. Five radar scattering mechanisms involving the lunar regolith. (left to right) The first term ($\overline{I}_{sur}$) represents diffuse scattering from the rough surface, the second term ($\overline{I}_{bedrock}$) is scattering from the bottom rough interface, the third term ($\overline{I}_{vol}$) is scattering from a single buried inclusion, the fourth term ($\overline{I}_{bedrock\_vol}$) is scattering at the lower interface followed by scattering from an inclusion, and the fifth term ($\overline{I}_{vol\_bedrock}$) shows the scattering from a single inclusion followed by scattering at the base of the regolith. Note that the second through fifth cases are also affected by the properties of the top interface.

[33] The received Stokes vector (in region 0) is

$$\begin{aligned}\overline{I}(\theta,\phi,z=0) = &\int_0^{2\pi} d\phi' \int_0^{\pi/2} d\theta' \sin\theta' \overline{\overline{T}}_{10}(\theta,\phi;\theta',\phi') \\ &\cdot \overline{I}(\theta',\phi',z=0) \\ &+ \int_0^{2\pi} d\phi' \int_0^{\pi/2} d\theta' \sin\theta' \overline{\overline{R}}_{01}(\theta,\phi;\theta',\phi') \\ &\cdot \overline{I}_i(\pi-\theta',\phi',z=0) \end{aligned} \tag{8}$$

In equations (7) and (8), $\overline{\overline{R}}_{ij}$ and $\overline{\overline{T}}_{ij}$ are the scattering and transmission matrices (from layer i to j), and they are obtained by using IEM for rough surface scattering (see Appendix A for more details). $\overline{I}_i(\pi-\theta,\phi,z=0) = \overline{I}_i \delta(\cos\theta - \cos\theta_i)\delta(\phi-\phi_i)$ in equation (8) is the incident Stokes vector, where the incident angle ($\pi - \theta$) is defined with respect to the vertical $\hat{z}$ axis. The Kronecker delta functions denote the incident direction, where the angles θ_i and ϕ_i denote the incidence and azimuthal angle of the incident radar wave.

[34] Using an iterative method to solve the VRT equation (4) with boundary conditions (7), the scattered Stokes vector $\overline{I}_s(\theta,\ \phi,\ z\ =\ 0)$ above the surface (in region 0) is (see Appendix B for details)

$$\begin{aligned}\overline{I}_s(\theta,\phi,z=0) = &\overline{I}_{sur}(\theta,\phi,z=0) + \overline{I}_{bedrock}(\theta,\phi,z=0) \\ &+ \overline{I}_{vol}(\theta,\phi,z=0) + \overline{I}_{bedrock\_vol}(\theta,\phi,z=0) \\ &+ \overline{I}_{vol\_bedrock}(\theta,\phi,z=0) \end{aligned} \tag{9}$$

where the subscript "s" indicates the scattered signal. Figure 6 shows schematically the five scattering mechanisms that are considered in the above equation. The first term ($\overline{I}_{sur}$) is diffuse scattering from the rough surface, the second term ($\overline{I}_{bedrock}$) is scattering from the bottom rough interface, the third term ($\overline{I}_{vol}$) is the scattering from individual buried rocks, the fourth term ($\overline{I}_{bedrock\_vol}$) is scattering at the lower interface followed by scattering from a single rock, and the fifth term ($\overline{I}_{vol\_bedrock}$) is the scattering from a single rock followed by scattering at the base of the regolith. Note that the second through fifth terms are also affected by the properties of the top interfaces. For convenience, hereafter we refer to these five terms as surface scattering, subsurface scattering, volume scattering, subsurface-volume scattering, and volume-subsurface scattering. As will be discussed more in section 4, our model does not take into account multiple scattering among rocks and is incapable of modeling the coherent backscatter opposition effect (CBOE) [e.g., *Hapke*, 1990; *Jin and Lax*, 1990; *Peters*, 1992].

[35] The five scattering terms in equation (9) are expressed as

$$\overline{I}_{sur}(\theta,\phi,z=0) = \overline{\overline{R}}_{01}(\theta,\phi;\theta_i,\phi_i)\cdot\overline{I}_i \tag{10a}$$

$$\begin{aligned}\overline{I}_{bedrock}(\theta,\phi,z=0) = &\int_0^{2\pi} d\phi' \int_0^{\pi/2} d\theta' \sin\theta' \overline{\overline{T}}_{10}(\theta,\phi;\theta',\phi') \\ &\cdot \overline{\overline{E}}(\theta',\phi')\overline{\overline{D}}[-\beta(\theta',\phi')d\sec\theta'] \\ &\cdot \overline{\overline{E}}^{-1}(\theta',\phi') \int_0^{2\pi} d\phi'' \int_0^{\pi/2} d\theta'' \\ &\cdot \sin\theta'' \overline{\overline{R}}_{12}(\theta',\phi';\theta'',\phi'')\overline{\overline{E}}(\pi-\theta'',\phi'') \\ &\cdot \overline{\overline{D}}[-\beta(\pi-\theta'',\phi'')d\sec\theta''] \\ &\cdot \overline{\overline{E}}^{-1}(\pi-\theta'',\phi'')\overline{\overline{T}}_{01}(\theta'',\phi';\theta_i,\phi_i)\overline{I}_i \end{aligned} \tag{10b}$$

$$\begin{aligned}\overline{I}_{vol}(\theta,\phi,z=0) = &\int_0^{2\pi} d\phi' \int_0^{\pi/2} d\theta' \sin\theta' \overline{\overline{T}}_{10}(\theta,\phi;\theta',\phi') \\ &\cdot \sec\theta' \int_{-d}^{0} dz' \overline{\overline{E}}(\theta',\phi') \\ &\cdot \overline{\overline{D}}[\beta(\theta',\phi')z'\sec\theta']\overline{\overline{E}}^{-1}(\theta',\phi') \\ &\cdot \int_0^{2\pi} d\phi'' \int_0^{\pi/2} d\theta'' \sin\theta'' \overline{\overline{P}}(\theta',\phi';\pi-\theta'',\phi'') \\ &\cdot \overline{\overline{E}}(\pi-\theta'',\phi'')\overline{\overline{D}}[\beta(\pi-\theta'',\phi'')z'\sec\theta''] \\ &\cdot \overline{\overline{E}}^{-1}(\pi-\theta'',\phi'')\overline{\overline{T}}_{01}(\theta'',\phi'';\theta_i,\phi_i)\overline{I}_i \end{aligned} \tag{10c}$$

$$\bar{I}_{bedrock\_vol}(\theta,\phi,z=0) = \int_0^{2\pi} d\phi' \int_0^{\pi/2} d\theta' \sin\theta' \bar{\bar{T}}_{10}(\theta,\phi;\theta',\phi') \cdot \sec\theta' \int_{-d}^{0} dz' \bar{\bar{E}}(\theta',\phi') \cdot \bar{\bar{D}}[\beta(\theta',\phi')z' \sec\theta'] \bar{\bar{E}}^{-1}(\theta',\phi') \cdot \int_0^{2\pi} d\phi'' \int_0^{\pi/2} d\theta'' \sin\theta'' \bar{\bar{P}}(\theta',\phi';\theta'',\phi'') \cdot \bar{\bar{E}}(\theta'',\phi'') \bar{\bar{D}}[-\beta(\theta'',\phi'')(z'+d)\sec\theta''] \cdot \bar{\bar{E}}^{-1}(\theta'',\phi'') \int_0^{2\pi} d\phi''' \int_0^{\pi/2} d\theta''' \sin\theta''' \cdot \bar{\bar{R}}_{12}(\theta'',\phi'';\theta''',\phi''') \bar{\bar{E}}(\pi-\theta''',\phi''') \cdot \bar{\bar{D}}[-\beta(\pi-\theta''',\phi''')d\sec\theta'''] \cdot \bar{\bar{E}}^{-1}(\pi-\theta''',\phi''') \bar{\bar{T}}_{01}(\theta''',\phi''';\theta_i,\phi_i)\bar{I}_i \tag{10d}$$

$$\bar{I}_{vol\_bedrock}(\theta,\phi,z=0) = \int_0^{2\pi} d\phi' \int_0^{\pi/2} d\theta' \sin\theta' \bar{\bar{T}}_{10}(\theta,\phi;\theta',\phi') \cdot \bar{\bar{E}}(\theta',\phi') \bar{\bar{D}}[-\beta(\theta',\phi')d\sec\theta'] \cdot \bar{\bar{E}}^{-1}(\theta',\phi') \int_0^{2\pi} d\phi'' \int_0^{\pi/2} d\theta'' \sin\theta'' \cdot \bar{\bar{R}}_{12}(\theta',\phi';\theta'',\phi'') \sec\theta'' \int_{-d}^{0} dz' \bar{\bar{E}}(\pi-\theta'',\phi'') \cdot \bar{\bar{D}}[-\beta(\pi-\theta'',\phi'')(z'+d)\sec\theta''] \cdot \bar{\bar{E}}^{-1}(\pi-\theta'',\phi'') \int_0^{2\pi} d\phi''' \int_0^{\pi/2} d\theta''' \sin\theta''' \cdot \bar{\bar{P}}(\pi-\theta'',\phi'';\pi-\theta''',\phi''') \bar{\bar{E}}(\pi-\theta''',\phi''') \cdot \bar{\bar{D}}[\beta(\pi-\theta''',\phi''')z'\sec\theta'''] \cdot \bar{\bar{E}}^{-1}(\pi-\theta''',\phi''') \bar{\bar{T}}_{01}(\theta''',\phi''';\theta_i,\phi_i)\bar{I}_i \tag{10e}$$

where $\bar{\bar{D}}$ $[\beta(\theta, \phi)z\sec\theta]$ is a 4 × 4 diagonal matrix with the diagonal elements given by $\exp[\beta_i(\theta, \phi)z\sec\theta]$, and $\bar{\bar{E}}$ and $\beta_i(\theta, \phi)$ (i = 1, 2, 3, 4) are the eigenvector matrix and eigenvalues of the extinction matrix $\bar{\bar{K}}_e$, respectively. For additional details related to the calculation of these terms, the reader is referred to *Tsang et al.* [1985] and *Jin* [1994].

[36] Equation (9) contains multiple integrals (as high as sevenfold) and these angular integrals are required because of the diffuse scattering and transmission through the random rough interfaces. Scattering and transmission at a rough surface can be decomposed into coherent and noncoherent parts, and the reflection and transmission matrices $\bar{\bar{R}}_{12}$, $\bar{\bar{T}}_{01}$, $\bar{\bar{T}}_{10}$ can be written as [*Fung*, 1994, chap. 2]

$$\bar{\bar{R}}(\theta,\phi;\theta_i,\phi_i) = \bar{\bar{R}}^n(\theta,\phi;\theta_i,\phi_i) + \bar{\bar{R}}^c(\theta,\phi;\theta_i,\phi_i) \cdot \delta(\cos\theta-\cos\theta_i)\delta(\phi-\phi_i) \tag{11a}$$

$$\bar{\bar{T}}(\theta,\phi;\theta_i,\phi_i) = \bar{\bar{T}}^n(\theta,\phi;\theta_i,\phi_i) + \bar{\bar{T}}^c(\theta,\phi;\theta_i,\phi_i) \cdot \delta\left(\cos\theta-\cos\theta_i^+\right)\delta\left(\phi-\phi_i^+\right) \tag{11b}$$

where the Kronecker delta functions $\delta(\cos\theta - \cos\theta_i)\delta(\phi - \phi_i)$ and $\delta(\cos\theta - \cos\theta_i^+)\delta(\phi - \phi_i^+)$ denote coherent scattering and transmission at specular or diffraction directions, respectively. (θ_i^+, ϕ_i^+) indicates the diffraction angle of the incident wave (θ_i, ϕ_i) and the superscripts c and n denote the coherent and noncoherent components, respectively. The first term on the right hand side of equation (11) dominates if the surface boundary is very rough, while the second term dominates for a smooth surface with a low-dielectric contrast at the boundary interface.

[37] Because the lunar surface is relatively flat over large scales (with RMS slopes of 2–4° for the maria and 6–8° for the highlands on the scales of decimeters to a hundred meters) and because the regolith dielectric permittivity is small ($\varepsilon_1' \sim 3$), noncoherent scattering from the surface is negligible compared with coherent scattering. Substituting equation (11) into equation (9), and ignoring the scattering mechanisms that involve more than one noncoherent scattering event, the Stokes vector of the received radar echo $\bar{I}_s(\theta, \phi, z = 0)$ can be expressed as

$$\bar{I}_s(\theta,\phi,z=0) = \bar{\bar{M}}(\theta,\phi;\pi-\theta_i,\phi_i)\cdot\bar{I}_i(\pi-\theta_i,\phi_i) \tag{12}$$

where the Mueller matrix $\bar{\bar{M}}(\theta, \phi; \pi - \theta_i, \phi_i)$ is

$$\bar{\bar{M}}(\theta,\phi;\pi-\theta_i,\phi_i) = \bar{\bar{M}}_{sur}(\theta,\phi;\pi-\theta_i,\phi_i) + \bar{\bar{M}}_{bedrock}(\theta,\phi;\pi-\theta_i,\phi_i) + \bar{\bar{M}}_{vol}(\theta,\phi;\pi-\theta_i,\phi_i) + \bar{\bar{M}}_{bedrock\_vol}(\theta,\phi;\pi-\theta_i,\phi_i) + \bar{\bar{M}}_{vol\_bedrock}(\theta,\phi;\pi-\theta_i,\phi_i) \tag{13}$$

where $\bar{\bar{M}}_{sur}$, $\bar{\bar{M}}_{bedrock}$, $\bar{\bar{M}}_{vol}$, $\bar{\bar{M}}_{bedrock\_vol}$, and $\bar{\bar{M}}_{vol\_bedrock}$ are the Mueller matrices for the surface scattering, subsurface scattering, volume scattering, subsurface-volume scattering and volume-subsurface scattering terms, respectively. Appendix C gives the expressions of the Mueller matrices for these five scattering terms.

3.2. Influence of Surface Slope

[38] Lunar surface slopes, such as those resulting from crater walls and lava channels, can change the received radar echoes and CPR values since the surface slope affects both the local incidence angle and the polarization state of the incident radar wave in the local coordinate frame. Figure 7a shows a surface that is tilted with respect to our $(\hat{x}, \hat{y}, \hat{z})$ coordinate system, and where the locally flat surface is expressed by the coordinates $(\hat{x}_l, \hat{y}_l, \hat{z}_l)$.

[39] In the local coordinates $(\hat{x}_l, \hat{y}_l, \hat{z}_l)$ the Mueller matrix is expressed by equation (13), but with a transformation of the incident and scattering angles from the principal coordinates $(\hat{x}, \hat{y}, \hat{z})$ to the local coordinates $(\hat{x}_l, \hat{y}_l, \hat{z}_l)$. The polarization bases (i.e., the polarization base vectors $\hat{v}$ and $\hat{h}$) of the Mueller matrix in local coordinates are rotated (see Figure D1) in order to obtain the Mueller matrix in the principal coordinates, as follows [e.g., *Jin et al.*, 2007]:

$$\bar{\bar{M}}(\theta,\phi;\theta_i,\phi_i) = \bar{\bar{U}}(\Delta_s)\cdot\bar{\bar{M}}^l\left(\theta^l,\phi^l;\theta_i^l,\phi_i^l\right)\cdot\bar{\bar{U}}^{-1}(\Delta_i) \tag{14}$$

where the superscript l denotes the Mueller matrix, incident and scattered angles in the local coordinates, Δ_i and Δ_s are

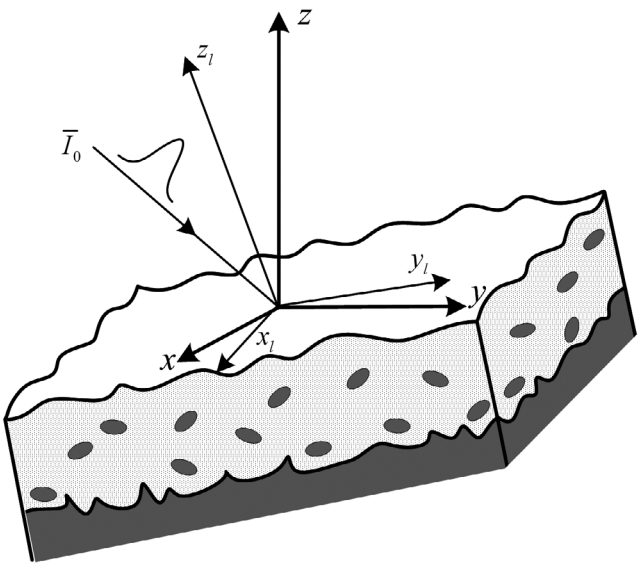

Figure 7. Schematic diagram showing the relation between local ($\hat{x}_l$, $\hat{y}_l$, $\hat{z}_l$) and principle coordinates ($\hat{x}$, $\hat{y}$, $\hat{z}$) for a surface with a large-scale slope.

the rotation angles of the incident and scattered polarization bases, and $\overline{\overline{U}}$ is the rotation matrix of the polarization bases of the Stokes vector:

$$\overline{\overline{U}}(\Delta) = \begin{bmatrix} \cos^2\Delta & \sin^2\Delta & \frac{1}{2}\sin 2\Delta & 0 \\ \sin^2\Delta & \cos^2\Delta & -\frac{1}{2}\sin 2\Delta & 0 \\ -\sin 2\Delta & \sin 2\Delta & \cos 2\Delta & 0 \\ 0 & 0 & 0 & 1 \end{bmatrix} \quad (15)$$

Appendix D describes the details concerning the calculation of the local incident and scattering angles, and the rotation angles Δ_i and Δ_s.

3.3. Polarimetric Radar Scattering Coefficient and CPR Calculation

[40] The Stokes vector in the VRT equation is a four-column vector that represents the intensity and polarization state of an arbitrary electromagnetic wave. For an incident wave with any arbitrary elliptical polarization with elliptic angle χ ($\chi \in [-\pi/4, \pi/4]$) and orientation angle ψ($\psi \in [0, \pi]$), the Stokes vector $\bar{I}_i = [I_v, I_h, U, V]^T$ can also be written as [e.g., *Tsang et al.*, 1985, chap. 2; *Jin*, 1994, chap. 1]

$$\bar{I}_i = \begin{bmatrix} I_v \\ I_h \\ U \\ V \end{bmatrix} = \begin{bmatrix} \frac{1}{2}I_0(1 - \cos 2\chi \cos 2\psi) \\ \frac{1}{2}I_0(1 + \cos 2\chi \cos 2\psi) \\ -I_0 \cos 2\chi \sin 2\psi \\ I_0 \sin 2\chi \end{bmatrix} \quad (16)$$

where $I_0 = I_v + I_h$ is the intensity of the incident radar wave. By changing the value of the elliptic and orientation angles χ and ψ, we can obtain the Stokes vector for different polarization states. $\chi < 0$ indicates a right-hand polarized wave and $\chi > 0$ indicates a left-hand polarized wave. For example, the Stokes vector for a right circular polarization (RCP) radar wave with $\chi = -45°$ is $\bar{I}_R = [0.5, 0.5, 0, -1.0]^T$, and for a left circular polarization (LCP) wave with $\chi = 45°$ is $\bar{I}_L = [0.5, 0.5, 0, 1.0]^T$. Inserting the incident Stokes vector $\bar{I}_i$ with any arbitrary polarization state into equation (12) we can compute the intensity of the received radar echo from the lunar surface.

[41] Following *Jin* [1994], the copolarized (that is, the opposite sense as the transmitted polarizations, here labeled "OC") scattered power is

$$P_n = \frac{1}{2}I_{vs}(1 - \cos 2\chi \cos 2\psi) + \frac{1}{2}I_{hs}(1 + \cos 2\chi \cos 2\psi) + \frac{1}{2}U_s \cos 2\chi \sin 2\psi + \frac{1}{2}V_s \sin 2\chi \quad (17)$$

where the subscript n denotes that the incident intensity is normalized, i.e., $I_0 = 1$ in equation (16). Therefore, the copolarized radar backscattering coefficient is

$$\sigma_{oc} = 4\pi \cos\theta_i P_n \quad (18)$$

and the depolarized (same sense as the transmitted polarization, here labeled "SC") radar backscattering coefficient is

$$\sigma_{sc} = 4\pi \cos\theta_i (I_{vs} + I_{hs} - P_n) \quad (19)$$

where θ_i is the incidence angle. From equations (18) and (19), for an incident radar wave with right circular polarization, the circular polarization ratio (CPR) μ_c can be written as

$$\mu_c = \frac{\sigma_{sc}}{\sigma_{oc}} = \frac{I_{vs} + I_{hs} - V_s}{I_{vs} + I_{hs} + V_s} \quad (20)$$

Our CPR expression of equation (20) follows the same convention as *Raney* [2007]. The CPR is an index that shows how the received radar energy is allocated between different polarization states. We note that when circularly polarized radar waves are transmitted, a single specular reflection from the surface of a planet will result in receiving a polarization with the opposite sense (i.e., the sign of χ will change).

4. Model Validation

[42] We assess the accuracy of our VRT radar scattering model by directly comparing the predicted polarimetric radar scattering coefficients with those obtained from numerical finite difference time domain (FDTD) [*Yee*, 1966] simulations of the radar wave equation with the same input parameters. FDTD is a full wave approach that solves directly Maxwell's equations of wave propagation in discrete time and space steps. In addition to allowing for the use of complex surface and subsurface geometries, this method implicitly accounts for multiple scattering among buried rocks and the coherent backscatter opposition effect [*Hapke*, 1990; *Jin and Lax*, 1990; *Peters*, 1992]. For our simulations, we used the commercial software XFDTD developed by Remcom company, which is a powerful tool for 3D electromagnetic simulations. Before attempting a validation, several simulations were run in order to verify existing analytical solutions, such as for Mie scattering from a sphere.

[43] For our simulations, the frequency of the incident radar wave was set to 2.38 GHz, which corresponds to the 12.6 cm wavelength of the Chandrayaan-1 Mini-SAR. The FDTD simulation space was chosen as a box with dimensions 1.5 × 1.5 m in the horizontal directions and 1.0 m in vertical direction. The lunar surface and subsurface were generated numerically for the case of a 3-D Gaussian rough surface according to *Kuang and Jin* [2007], where the correlation length of both surfaces was set equal to $l_1 = l_2 = 0.1$ m, and the RMS height of the lunar surface and subsurface was set to $\delta_1 = 0.15$ m and $\delta_2 = 0.1$ m, respectively. The regolith thickness was set to 0.85 m, and the bedrock layer was therefore 0.15 m thick. Buried rocks were modeled as ellipsoids with semimajor and semiminor axes of 0.03 m and 0.015 m, respectively, where the orientation of each ellipsoid was chosen randomly. The fractional volume of buried rocks for this simulation was 0.005, corresponding to 398 ellipsoids in the simulation space. The dielectric constant of the regolith, buried rocks and underlying bedrock were set to $\varepsilon_1 = 2.7 + i0.003$, $\varepsilon_s = 6.0 + i0.01$ and $\varepsilon_2 = 6.0 + i0.05$, respectively [e.g., *Olhoeft and Strangway*, 1975]. Given the FDTD stability criterion that the cell size must be less than 1/10 of the shortest radar wavelength, the cell dimension was set to 0.5 cm. Three absorbing layers (10 cells for each layer) were added to the edges of the simulation box (in both horizontal directions and the bottom of the simulation space) in order to eliminate diffraction effects from the truncated surface edges. The perfectly matched layer (PML) absorbing boundary condition was further used for absorbing the outward-propagating waves. Regardless of our attempt to minimize the influence of the finite boundary conditions on our results, we note that our radar scattering coefficients contain a minor contribution from the tops of the vertical boundary layers. After the wavefield in the simulation space (near-field zone) reached steady state, scattered fields in the far-field zone were calculated using the Huygens principle, from which the scattering coefficients were calculated.

[44] The incidence angle of the radar wave for our simulations was set equal to 35° (with an azimuthal angle of 0° with respect to the normal of one of the vertical faces of the simulation space), and the incident radar wave was vertically polarized. Figure 8 shows a comparison of the bistatic radar scattering coefficients for VV and HV polarizations for one realization (red) of the random processes (i.e., surface roughness and rock distributions), the average of 10 realizations (blue) and the average of 40 realizations (dark cyan). In Figure 8, the abscissa axis is the scattering angle θ_s and the azimuthal angle is 180° (see Figure 1), with $\theta_s = 35°$ indicating the backscattering direction. It should be noted that the VRT model represents a statistically averaged result (as is evident from the expectations in equations (4) and (5)), while each FDTD simulation result (e.g., the red curve in Figure 8) is only for a single realization of the random process generating the surface relief, subsurface relief, and buried rock positions and orientations. In the FDTD calculation, the lunar surface is divided into a large number of discrete meshes. For a given mesh, the scattering would be strong in the direction for which the radar observation direction happens to be in the specular direction of the local incident radar wave. As a single realization of a 3D random rough surface with a finite size is not totally random, the number of meshes with a given orientation angle could be larger (or smaller) than that of another given orientation angle. This effect, together with the not perfectly random orientations of the buried rocks and subsurface roughness, causes the oscillations in the FDTD simulation result. As the number of FDTD realizations that are averaged becomes larger, the oscillations become smaller and the average of the FDTD simulation approaches that of the VRT solution, as seen by the blue and cyan curves in Figure 8. We can see that the VRT model matches well with the average of 40 realizations of FDTD simulation for scattering angles less than about 60°. At larger scattering angles, the FDTD simulation result is unreliable (the gray area in Figure 8) because of the influence of our artificial absorbing layers surrounding the simulation domain and since the perfectly matched layer boundary condition is not perfectly absorbing. A smaller number of simulations were run using a larger domain size (5.0 m × 5.0 m), and these were found to more closely approximate the VRT solution than those presented here for the same number of realizations.

[45] We note that the computational time associated with one FDTD simulation was about one day on a modern computer, while it takes no more than one second to obtain the comparable result with the VRT model. As the radar frequency increases, the FDTD simulations would require a smaller cell size and, hence, longer computation times.

[46] Finally, we note that two potentially important scattering mechanisms were neglected in our VRT model: multiple scattering between buried rocks and the coherent backscatter opposition effect [e.g., *Hapke*, 1990] that occurs near zero phase angles. Since our VRT model matches the FDTD simulations to within a few dB (which is about the same as the radiometric calibration of radar measurements), this suggests that we were justified in neglecting these effects in the VRT model. The maximum expected enhancement resulting from the CBOE is only a factor of 2 at zero phase for the same sense echo strength (i.e., 3 dB), and no such enhancement is apparent in our simulations (though it should be noted that the statistical variance of our simulations is comparable to the magnitude of this effect). Nevertheless, as discussed in section 7, these scattering mechanisms could be important for nearly pure low-dielectric loss ice deposits.

5. Comparison With Earth-Based Radar Data

[47] In this section, we compare our VRT model with Earth-based radar observations of the Moon and show that VRT model is capable of reproducing the average scattering properties of the lunar surface using a reasonable set of input parameters.

[48] By transmitting a radar signal from the 305 m Arecibo telescope in Puerto Rico and receiving the radar echoes using the 100 m Robert C. Byrd Green Bank Telescope in West Virginia, *Campbell et al.* [2007] obtained radar images of the lunar nearside at 70 cm wavelength (430 MHz frequency) via a synthetic aperture radar patch-focusing reduction technique with a spatial resolution of about 400 m. The radiometric uncertainty in the absolute backscattering coefficients is quoted as being ±3 dB, which is due primarily to the uncertainty in the transmitted power at Arecibo. Using the $FeO+TiO_2$ abundances from the Lunar Prospector gamma ray spectrometer [*Prettyman et al.*, 2006] and taking 10 wt.% $FeO+TiO_2$ as the dividing line between the maria and the

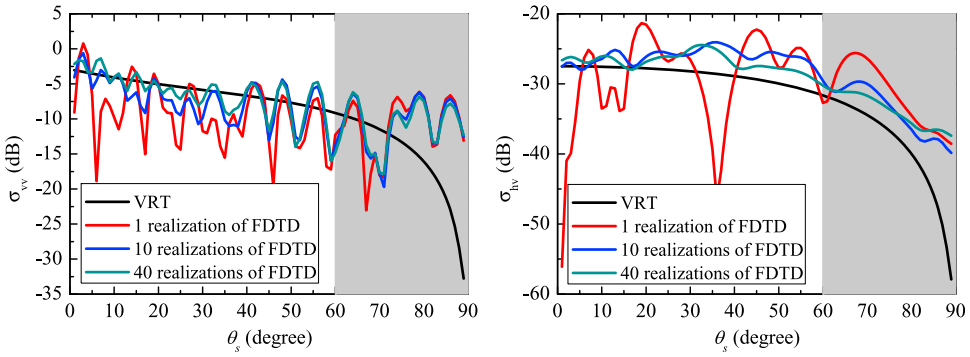

Figure 8. Comparison between one FDTD realization (red line), the average of 10 realizations (blue line), and the average of 40 realizations (dark cyan) with the VRT model (black line) of this study. (left) The vv polarization backscattering coefficient, and (right) hv polarization backscattering coefficient. The FDTD contribution from the vertical three absorbing layers becomes larger as the scattering angle increases beyond about 40°, and this contribution makes the results unreliable for scattering angles greater than about 60° (gray shaded area). The incident angle θ_i is 35° and (θ_s = 35°, ϕ_s = 180°) corresponds to the backscattering direction. The regolith thickness is d = 0.85 m, RMS heights and correlation lengths of the surface and subsurface are δ_1 = 0.15 m, l_1 = 0.1 m, δ_2 = 0.1 m, and l_2 = 0.1 m, the semimajor and semiminor axes of buried rock are c = 0.03 m and a = 0.015 m, the dielectric permittivity of the regolith, buried rocks, and underlying bedrocks are ε_1 = 2.7 + i0.003, ε_s = 6.0 + i0.01, and ε_2 = 6.0 + i0.05, respectively.

highlands, the average radar backscattering coefficients for each of these terrains as a function of incidence angle were compared with the predictions of our VRT model.

[49] Statistical results of the 70 cm Arecibo radar data show that, for both global and regional areas, the backscattering coefficients follow a lognormal distribution at any given incidence angle. Simulated radar images of impact craters, which change the local incidence angle of the radar wave (as will be discussed in section 6.6), also show that the backscattering coefficients are lognormally distributed about the value for a flat surface. Since the effect of local incidence angles is not taken into account in the processing of the Arecibo radar data, the average value of the backscattering coefficient is hence obtained by averaging the logarithm of the backscattering coefficients (in dB) instead of the backscattering coefficient itself. Taking the average of the backscattering coefficients in absolute units would bias the average value upward from that of a flat surface by about 3–5 dB.

[50] The black squares in Figure 9 show the incident angle–averaged polarized (opposite sense) and depolarized (same sense) radar backscattering coefficients of all the data for the maria (Figure 9, top) and highlands (Figure 9, bottom). We found that the same sense radar echoes are more sensitive to multiple scattering processes (such as rocks on the lunar surface or within the regolith). In particular, multiple scattering yields high CPRs [e.g., *Campbell et al.*, 2009], and the blue squares show the incident angle behavior for all pixels where the CPR is less than 0.25. As can be seen, the average of the depolarized backscattering coefficients with low CPRs is in general about 3–5 dB lower than the average of all the data for incidence angle greater than 30°. In contrast, for the polarized data, the incidence angle dependence is the same, regardless of the value chosen for the CPR cutoff value, indicating that the polarized returns are relatively insensitive to multiple scattering processes. Since we cannot easily remove the multiple scattering signals from the observed depolarized same sense data, we will only compare the polarized opposite sense backscattering coefficients with our VRT model.

[51] The imaginary part of the dielectric constant of the regolith for our VRT calculations was calculated from equation (1) using the FeO+TiO_2 abundances from the Lunar Prospector gamma ray spectrometer [*Prettyman et al.*, 2006] with a regolith bulk density of 1.5 g/cm^3 (corresponding to ε_1' = 2.7). The dielectric constants of buried rocks and bedrock were taken to be ε_s = 8.0 + i0.01 and ε_2 = 8.0 + i0.05, respectively. The regolith thickness over the lunar nearside was taken from the Chang-E 1 radiometer inversion of *Fa and Jin* [2010], and an exponential correlation function was used for both the lunar surface and subsurface, with a subsurface RMS slope equal to 1° (as will be shown in the following section this value does not change the radar echo significantly). As will be discussed in section 6, surface roughness and the fractional volume and size distribution of buried rocks are the two main factors that affect the radar echo strengths. Since information about these two parameters at a scale of 400 m (the spatial resolution of Arecibo radar image) over the lunar nearside is not available, best fitting values were obtained from an exhaustive search of surface RMS slopes between 1° and 10°, fraction volume of buried rocks from 0.0005 to 0.01, and semimajor and semiminor axes of the buried rocks from 0.01λ to 0.2λ (corresponding from 0.7 cm to 14 cm). The red line in Figure 9 shows one of the best fits to the polarized opposite sense radar echoes strengths. For the maria, the RMS slope is 4°, the fractional volume of buried rocks is equal to 0.0065, and the semimajor and semiminor axes are 0.01λ and 0.2λ. For the highlands, the RMS slope is 3°, the fractional volume of buried rocks is 0.001, and the semimajor and minor axes are 0.1λ and 0.01λ. We note that different combinations of fractional volume of buried rocks and average rock size can produce a similar radar echo, and that these values are hence not unique. For example, a small

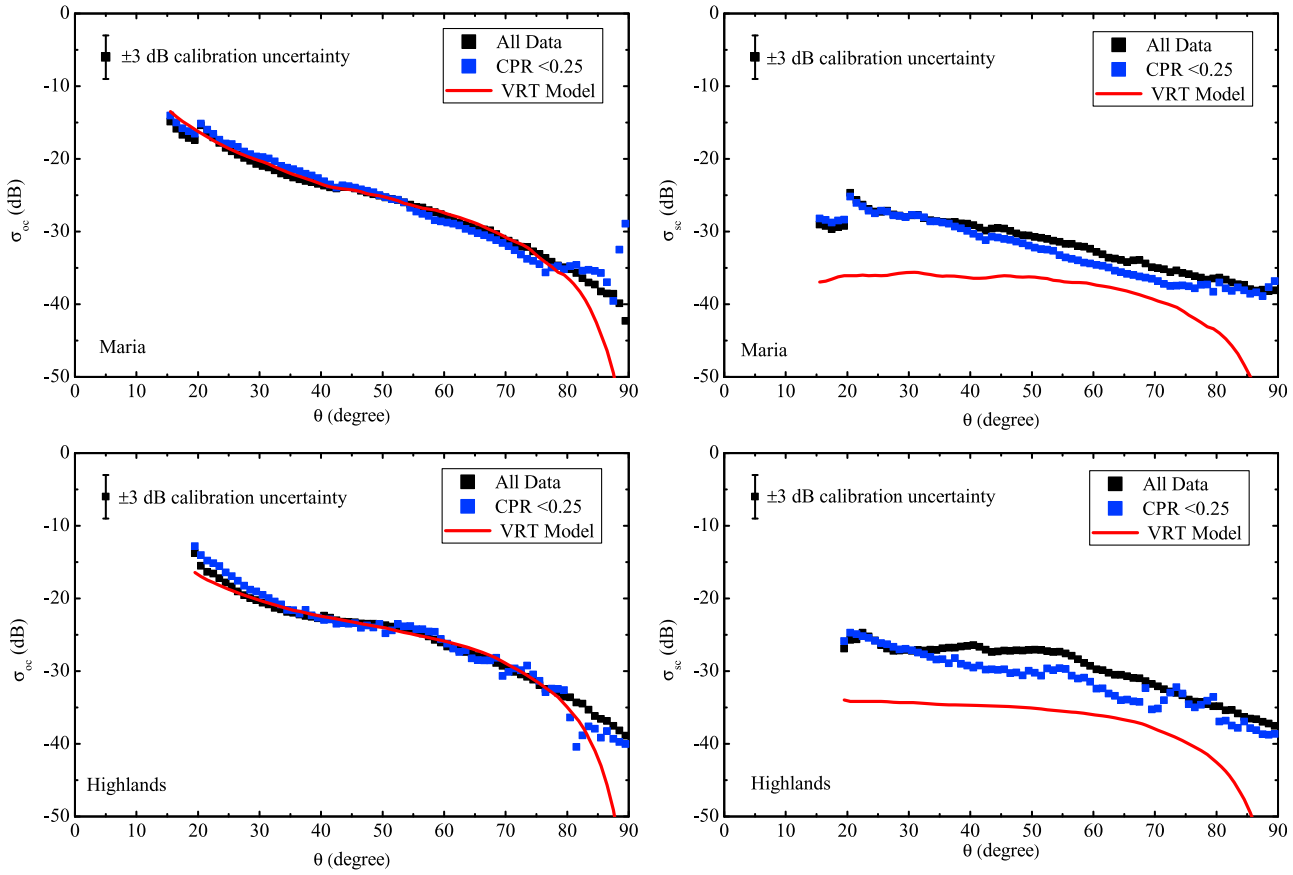

Figure 9. Comparison of (left) polarized (opposite circular, OC) and (right) depolarized (same circular, SC) radar backscattering coefficients as a function of incidence angle for the VRT model (red line) and Earth-based 70 cm Arecibo radar observations for (top) maria and (bottom) highlands. The black squares represent the average of the Arecibo data for a given incidence angle, whereas the blue squares represent the average of the data with circular polarization ratios (CPRs) less than 0.25. The average of the depolarized backscattering coefficients with CPR < 0.25 is about 3–5 dB smaller than the average of all data for incidence angles greater than 30°; for the polarized data the average is unchanged when the CPR < 0.25 values are calculated alone. VRT model parameters were chosen to provide best fit to the polarized OC data (left) since they are believed to include less multiple scattering. The calibration uncertainty of the Arecibo radar data is ±3 dB.

fractional volume combined with a large rock size would produce the same radar echoes as for a large fractional volume with small rock sizes.

[52] As can be seen, given our prior information on regolith properties, the VRT model shows a good comparison with the polarized opposite sense backscattering coefficients for both maria and highlands for incidence angles smaller than 80°. Better fits could be obtained if the RMS slopes, rock abundances, and rock shapes were allowed to vary with position. Nevertheless, the predicted depolarized radar echo strengths from the VRT model are roughly 6–8 dB smaller than the average Earth-based Arecibo 70 cm radar data. Parameters could be found that fit the depolarized same sense radar data as well as the opposite sense data, but in this case, the predicted polarized opposite sense echo strengths would be 6–8 dB higher than the observations. It was not possible to find acceptable parameter values that fit both the opposite and same sense data simultaneously. The most probable reason for this, as discussed above, is that the VRT model does not take into account multiple scattering between buried rocks or surface rocks, and that this is much more sensitive to the same sense radar echoes [*Pollack and Whitehill*, 1972; *Baron et al.*, 1996; *Campbell et al.*, 2009]. Another possible reason could be the calibration of the Arecibo data. In particular, we note that for observations at the same wavelength made by *Evans and Pettengill* [1963], the ratio of the polarized to depolarized radar echo strengths is more than 10 dB at incidence angle 30°, whereas it is only 5 dB for the newly acquired Arecibo radar data. Another reason might be the Faraday rotation effect that is caused by the Earth's ionosphere at P band frequencies (this effect can be ignored at higher frequencies, such as S band), and which could enhance the depolarized radar echo strength and reduce the polarized radar echo strength [e.g., *Qi and Jin*, 2007]. Though Faraday rotation has little or no effect on circular polarized radar wave, as for the transmitted wave from the Arecibo telescope, the reflected radar wave from the lunar surface is not circular any more. The reflected radar signal with elliptical polarization could be affected by Faraday rotation as it passes through the Earth's ionosphere.

[53] We also note that our VRT model is inconsistent with the observations at large incidence angles (>80°) and this is probably because the VRT model does not take into account the shadowing effect of scattering from rough surfaces, which becomes increasingly important at large incidence angles [*Fung*, 1994, chap. 4; *Jin*, 1994, chap. 9; *Tsang et al.*, 2000, chap. 9]. For this reason, our VRT model should probably be considered accurate only at incidence angles less than about 80°.

[54] We also compared the opposite sense Earth-based radar data of the lunar nearside from *Hagfors* [1970] at wavelengths of 3.8, 23 and 68 cm with our VRT model. Simulation results show that these multifrequency data are best fit using a lunar surface that is described by an exponential correlation function in comparison to a Gaussian correlation function [see also *Hagfors*, 1970; *Shepard and Campbell*, 1999]. With a set of typical input parameters in our VRT model, a lunar surface with an exponential correlation function matches the polarized (opposite sense) backscattering coefficients with a difference of 1 dB for incidence angles less than 60°. In contrast, a lunar surface with a Gaussian correlation function overestimates the backscattering coefficients by about 2–3 dB for incidence angles less than 20° and underestimates the backscattering coefficients by about 2–5 dB for incidence angles beyond 20°. This is consistent with the previous studies of *Hagfors* [1970] (at 23 cm and 68 cm) and *Thompson* [1978] (at 7.5 m). Thus, for the following calculations, we will use an exponential correlation function to describe the lunar surface.

6. Simulation Results and Analysis

[55] In the calculations that follow, if not mentioned specifically we will use a radar frequency of 2.38 GHz (corresponding to the 12.6 cm wavelength of the Chandrayaan-1 Mini-SAR) with a transmitted right circular polarization and an incidence angle of 35°, and the radar echo will be received in both left-hand (opposite sense) and right-hand (same sense) polarizations. Furthermore, we will use RMS slopes of the surface and subsurface of 5° and 1°, respectively, the fractional volume of the buried rocks will be set to 0.001 (similar to that of the Surveyor 5 landing site), the semimajor and semiminor axes of the buried rocks will be set equal to 0.1λ and 0.05λ (corresponding to 1.26 and 0.63 cm), a regolith thickness of 5 m will be assumed, and the dielectric constants of the regolith, buried rock and underlying bedrock will be set to $\varepsilon_1 = 2.7 + i0.003$, $\varepsilon_s = 6.0 + i0.01$ and $\varepsilon_2 = 6.0 + i0.05$, respectively. The following results for the polarized (OC) and depolarized (SC) radar echoes, as well as the CPR, will be calculated in the backscattering direction, although we note that our model can also calculate the bistatic radar scattering coefficient with an arbitrary transmit/receive polarization state.

[56] For a given frequency of the incident radar wave, the radar backscattering from a rough surface is highly dependent on the surface roughness, which is proportional to the ratio of RMS height and correlation length δ/l (a larger value indicates a rougher surface). As information concerning the RMS height and correlation length on the scale of the Mini-SAR spatial resolution (about 100 m) is not yet available, we will assume that the correlation length is equal to the wavelength of the incident radar wave, and then obtain different surface roughness by changing the RMS height. In the following simulations, the exponential correlation function is chosen as the correlation function for both the lunar surface and subsurface, since it matches the Earth-based observations better than a Gaussian correlation function. We note that for a rough surface with an exponential correlation function, the relation of $s = \sqrt{2}\delta/l$ between RMS slope s, RMS height δ and the correlation length l does not hold. Nevertheless, for comparative purposes we here use this relation to describe the roughness.

6.1. Incidence Angle

[57] Figure 10 shows the polarized (OC) and depolarized (SC) radar backscattering coefficient and the corresponding CPR as a function of incidence angle for each of the five scattering terms (the vertical gray areas indicate the range of incidence angles expected for the Mini-RF data on Chandrayaan-1 (~35°) and LRO (~49°)). In Figure 10, the black line indicates the total contribution, the red line indicates the contribution from the lunar surface, the blue line indicates the contribution from the interface between regolith and underlying bedrock, the dark cyan line indicates the contribution from the buried rocks, and the magenta line indicates the contribution from the interaction of buried inclusions (in this case rocks) with the subsurface, i.e., subsurface-volume and volume-subsurface scattering terms. From a statistical viewpoint, we note that the backscattering coefficients for the interactions of rocks with the subsurface are identical and the magenta line (labeled as "subsurface-volume") is thus the sum contribution of these two scattering mechanisms. It can be seen that as the incidence angle increases, the polarized radar echo from the entire lunar regolith layer decreases, while the depolarized radar echo only increases slightly, and that this causes the CPR to increase with increasing incidence angle.

[58] For the polarized (OC) radar echo in Figure 10a, all five of the scattering terms decrease with increasing incidence angle. The polarized radar echo is dominated by surface scattering at small incidence angles (<20° in Figure 10a), while it is dominated by scattering from buried rocks (i.e., volume scattering) at larger incidence angles. At the smallest incidence angles (<7° in Figure 10a), scattering from the base of the regolith layer is even more important than volume scattering, though the subsurface scattering contribution drops dramatically with increasing incidence angles. Because the path of the radar wave in the regolith becomes larger with increasing incidence angles, this causes the radar wave to become increasingly attenuated for all subsurface scattering mechanisms. Since the subsurface volume interaction terms involve more than one scattering process, the scattering contribution of these terms is small.

[59] The depolarized radar echo is dominated by scattering from buried rocks at all incidence angles. Both surface and subsurface scattering are negligible at incidence angles near 0° but they increase somewhat with increasing incidence angle, and then decrease with incidence angles beyond 50°.

[60] The CPR increases with increasing incidence angle for all five of the scattering terms. The CPR resulting solely from the subsurface-volume (or volume-subsurface) interaction term is the largest among the five scattering terms for incidence angles less than 67°. Nevertheless, it should be noted that the backscattering coefficients associated with

this scattering mechanism are small, so this makes only a small contribution to the total CPR. CPRs corresponding to the surface and subsurface scattering terms are extremely small at incidence angles near 0°, but increase dramatically with increasing incidence angle. The volume scattering term has the second largest CPR value at small incidence angles (<27° in Figure 10c), and then becomes the smallest among the five terms at larger incidence angles. We note that the subsurface-volume and volume-subsurface interactions that involve multiple scattering of the incident radar wave has a large CPR value because of the reallocation of power that occurs each time a scattering process occurs. We also note that when the CPR corresponding to either the surface, subsurface, volume-subsurface or subsurface-volume interaction is taken in isolation, that it can be larger than the total CPR. This is simply because the total CPR is not a simple addition of the component CPRs, but is rather the ratio of the entire depolarized radar echo to the polarized radar echo.

[61] As the penetration depth of the radar wave at X band frequencies is smaller than that at S band frequencies, the contributions from subsurface scattering will be relatively smaller for X band observations. On the other hand, volume scattering from the smaller-sized inclusions, which are invisible at longer wavelengths, will increase as the radar frequency increases. It can thus be expected that surface and volume scattering will also be the two dominant scattering terms for X band observations. We note that the incidence angle behaviors of the polarized and depolarized radar echo strengths and CPR at X band frequencies are similar to those at S band frequencies, which is consistent with Earth-based observations of the Moon [*Thompson*, 1987].

6.2. Regolith Thickness

[62] Figures 11a–11c show how the polarized (OC) and depolarized (SC) radar backscattering coefficients and associated CPR vary with regolith thickness for the five scattering terms shown in Figure 6 for an incidence angle of 35°. As can be seen, both polarized and depolarized backscattering coefficients increase as regolith thickness increases, approaching an asymptotic value for thickness beyond about 10 m. This behavior is mainly caused by the increased contribution of volume scattering, since the number of buried rocks increases as the regolith thickness increases. In a similar manner, as the regolith thickness increases, the contribution from the subsurface-volume (or volume-subsurface) scattering mechanisms increases as well. Nevertheless, the subsurface-volume (or volume-subsurface) contribution is seen to eventually decrease with increasing regolith thickness as the radar wave eventually becomes attenuated as it traverses the thick regolith layer. Because of these two factors, scattering resulting from the subsurface-volume (or volume-subsurface) interaction first increases and then decreases with increasing regolith thickness. As shown in Figure 11c, the CPR of each term is insensitive to regolith thickness. Regardless, the CPR of the entire

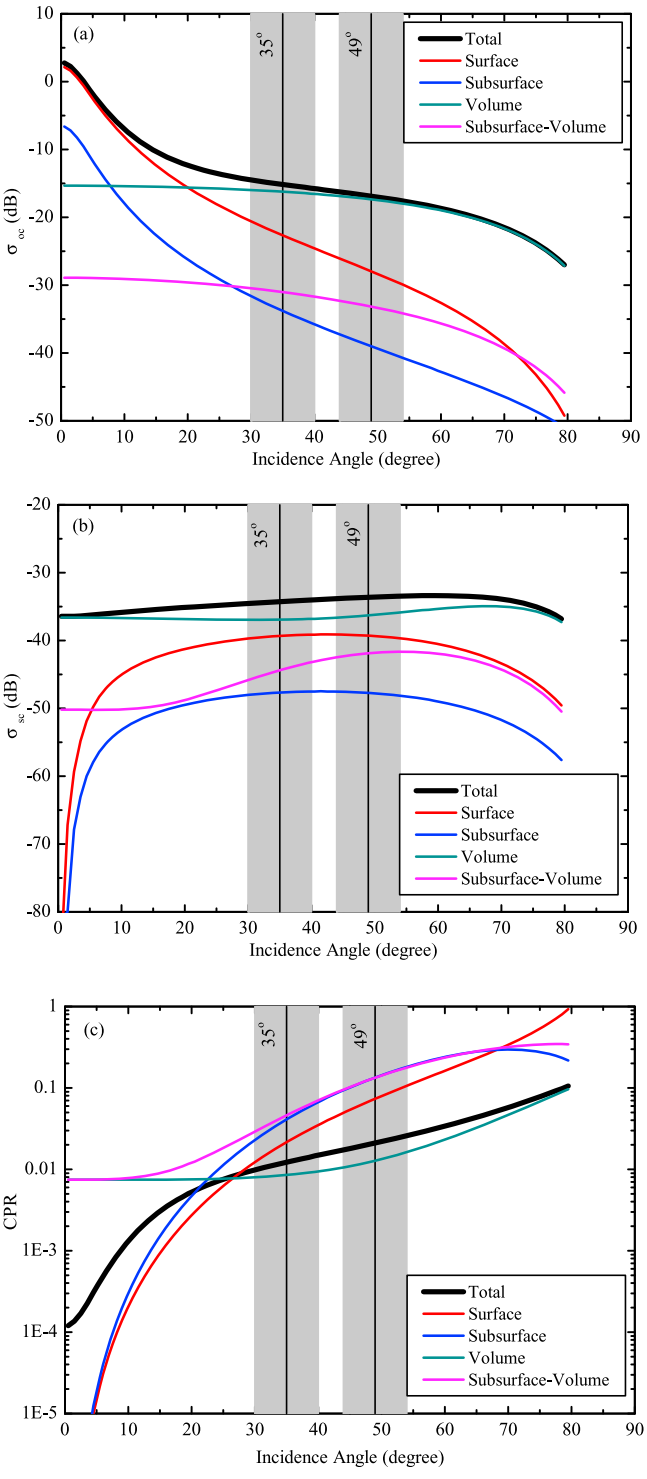

Figure 10. Plot of the (a) polarized and (b) depolarized radar backscattering coefficients and (c) the corresponding CPR as a function of radar incidence angle for each of the five scattering terms. The vertical gray areas indicate the range of expected Mini-SAR incidence angles (approximately 35° for Chandrayaan-1 and 49° for LRO). The black line indicates the total contribution of the five terms, the red line indicates the contribution from the lunar surface, the blue line indicates the contribution from the interface between regolith and underlying bedrock, the dark cyan line indicates the contribution from the buried rocks, and the magenta line is the summed contribution from both interactions of buried rocks with the subsurface (compare with Figure 6).

regolith layer (black line in Figure 11c) decreases with increasing regolith thickness.

[63] Both the polarized and depolarized radar echoes increase as the regolith thickness increases, while the CPR decreases slightly with increasing thickness of the regolith. As a result of this, the lunar highlands, whose regolith thickness is greater than the maria by about a factor of two, should have relatively strong radar echoes and a relatively small CPR when compared to the mare. This is consistent with the difference in radar echo strengths observed between the mare and highland from Earth-based radar images of the Moon [*Thompson*, 1987; *Campbell et al.*, 2007].

6.3. Regolith Dielectric Permittivity

[64] The polarized (OC) and depolarized (SC) backscattering coefficients and CPR are shown in Figures 11d–11f as a function of the real part of the complex dielectric permittivity of the regolith, ε_1'. In Figures 11d–11f, ε_1' varies from 2.0 to 6.0 (corresponding to a regolith bulk density from 1.1 to 2.8 g/cm^3) for a fixed imaginary part of 0.003. Since the Fresnel reflection coefficient increases with increasing ε_1', surface scattering is seen to increase with increasing dielectric permittivity ε_1'. As ε_1' increases, less radar energy penetrates into the subsurface, and the dielectric contrast between the regolith and the buried rocks also decreases. Therefore, both volume scattering and subsurface-volume interactions decrease with increasing ε_1'. As a result of these two factors, the polarized radar echo strength decreases slightly with increasing ε_1', while the depolarized echo strength at first decreases and then increases with increasing ε_1'. The total CPR decreases with increasing ε_1', obtaining a minimum value near $\varepsilon_1' = 3.0$, and then increases with increasing ε_1'.

[65] The loss tangent of the lunar regolith increases as the abundance of $FeO+TiO_2$ increases, and this causes an increase in the attenuation of the radar wave and hence a corresponding decrease of the received radar echo strength. The polarized (OC) and depolarized (SC) backscattering coefficients and CPR are shown in Figures 11g–11i as a function of the abundance of $FeO+TiO_2$, where the dielectric constant of the regolith is calculated from equation (1) using a bulk density of 1.5 g/cm^3 (corresponding to $\varepsilon_1' = 2.7$). Surface scattering shows no sensitivity to the $FeO+TiO_2$ content, since the surface reflectivity only correlates with the real part of the dielectric constant of the regolith. As the $FeO+TiO_2$ content increases, the increased attenuation causes a decrease of the volume, subsurface, subsurface-volume, and volume-subsurface scattering. These factors cause a decrease of the received radar echoes and an increase of the CPR. Therefore, the mare, with high $FeO+TiO_2$ content, will have lower radar echoes and higher CPRs than the highlands, which is consistent with Earth-based radar observations [*Thompson* 1987; *Campbell et al.*, 2007].

6.4. Buried Rocks

[66] Figures 11j–11l show how the polarized (OC) and depolarized (SC) radar backscattering coefficients and the CPR vary as a function of the fractional volume of buried rocks for the five scattering terms. The fractional volume of buried rocks here varies from 0 to 0.1, as implied by the observed rock population at the Surveyor landing sites as shown in Figure 2, and volume scattering is seen to be the dominant scattering mechanism. Scattering from the buried rocks increases as the rock abundance increases and eventually reaches a saturation value. Increasing the rock abundance causes an increase in the scattering loss of the radar wave, and therefore scattering from the subsurface is reduced (blue line of in Figures 11g and 11h). By the influence of these two factors, the subsurface-volume (or volume-subsurface) interaction first increases and then decreases with increasing fractional volume of buried rocks. Also, as can be seen, the number of buried rocks does not change the CPR for each individual scattering term. Under the condition of single scattering from rocks, the total radar echo strength increases as the abundance of buried rocks increase, while the CPR decreases only slightly as the rock abundance increases.

[67] Polarimetric radar scattering is sensitive to the shape and orientation of the subsurface rocks. The polarized (OC) and depolarized (SC) radar backscattering coefficients and CPR are shown in Figures 11m–11o as a function of the shape of the buried rocks, indicated by c/a (the ratio of the semimajor and semiminor axes of the buried rocks). A value of c/a of unity indicates a sphere, whereas a value greater than one indicates a prolate spheroid and a value less than one represents an oblate spheroid. As can be seen, the shape of the rocks mainly affects the volume scattering, subsurface-volume and volume-subsurface interactions. The polarized radar echo arising solely from the buried rocks is a monotonically increasing function of c/a, whereas the depolarized radar echo is relative constant for c/a less than 1, and increases sharply for c/a greater than 1. Both the polarized and depolarized radar echoes from the subsurface-volume (or volume-subsurface) interactions increase with increasing c/a. The CPR resulting solely from scattering by the buried rocks is a minimum for spherical particles, and increases with increasing rock oblateness, and the CPR resulting solely from the subsurface-volume (or volume-subsurface) interactions has a similar behavior. The total polarized backscattering coefficient is seen to monotonically increase with increasing c/a, whereas for the depolarized signal, the backscattering coefficient only varies slightly for c/a less than 1 and increases for c/a greater than 1. As a result of this behavior, the total CPR has a distinct minimum for spherical rocks.

6.5. Surface and Subsurface Roughness

[68] As the surface roughness increases, more radar energy is reflected in the backscattering direction. Figures 12a–12c show the polarized (OC) and depolarized (SC) radar backscattering coefficients and CPR as a function of surface RMS slope for the five scattering terms, where the RMS slope of the subsurface has been set to 1°. It can be seen that both the radar echoes and CPR increase with increasing surface roughness. As surface roughness increases, less energy penetrates into the regolith layer, and therefore scattering from the buried rocks and surface-volume interaction decreases.

[69] Figures 12d–12e show the variation of the polarized (OC) and depolarized (SC) radar backscattering coefficients and CPR as a function of the subsurface roughness for the five scattering terms, where the RMS slope of the surface

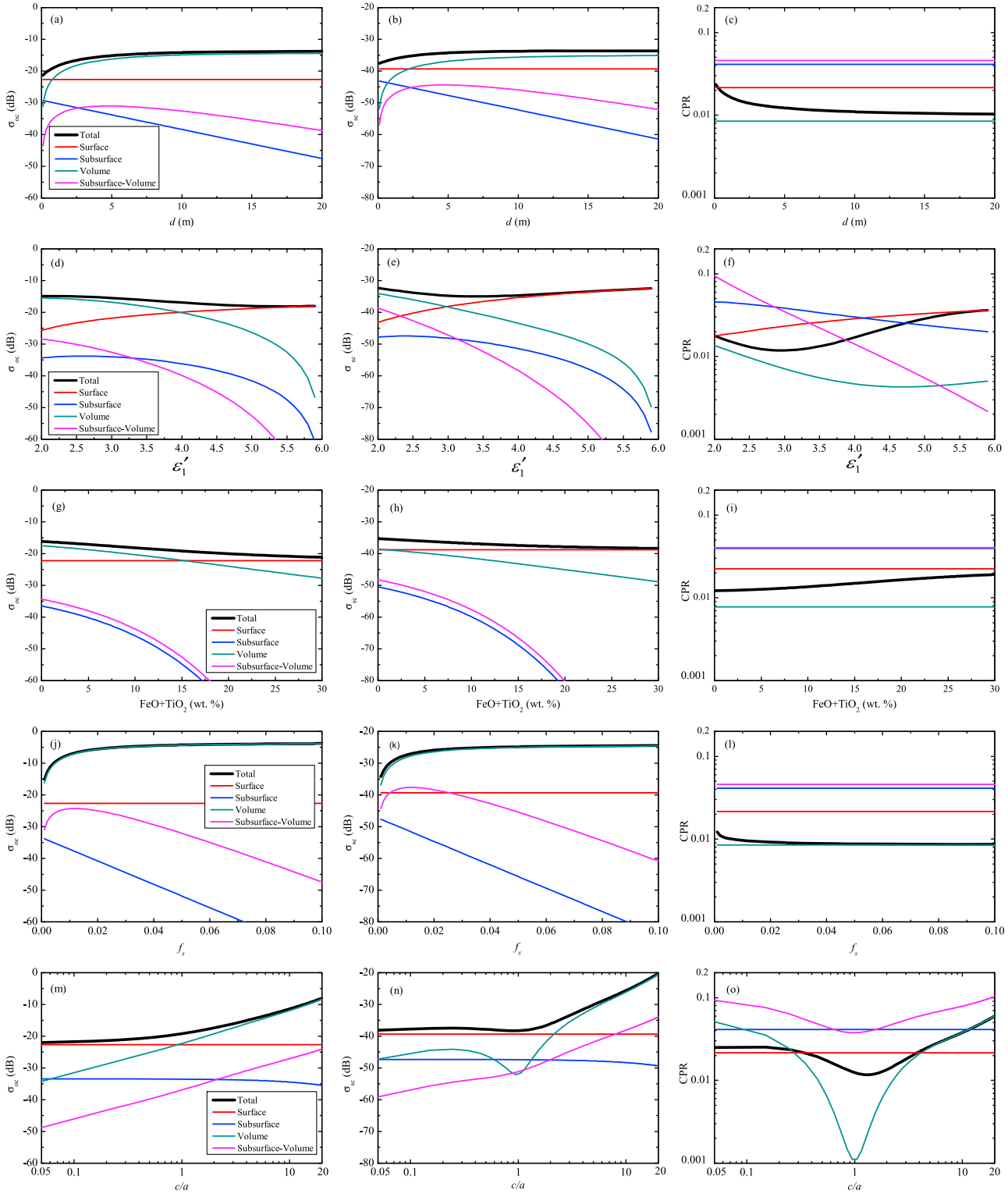

Figure 11. Polarized (σ_{oc}) and depolarized (σ_{sc}) radar backscattering coefficients and the CPR as a function of (a–c) regolith thickness, (d–f) real part of the dielectric permittivity, (g–i) the abundance of $FeO+TiO_2$, (j–l) the fractional volume of buried rocks, and (m–o) the shape of the buried rocks. The model calculations were carried out in the backscattering direction with an incidence angle 35°. The black lines indicate the total contribution from the five scattering terms, the red line indicates the contribution from the lunar surface, the blue line indicates the contribution from the interface between regolith and underlying bedrock, the dark cyan line indicates the contribution from the buried rocks, and the magenta line is the summed contribution from both interactions of buried rocks with the subsurface (compare with Figure 6).

has been set to 1°. It can be seen that both polarized and depolarized radar echo strengths from the subsurface increase as subsurface roughness increases, whereas radar echo strengths from the surface-volume interaction strongly decreases with increasing subsurface roughness. The CPR resulting solely from the subsurface decreases with increasing subsurface roughness, and this causes the CPR from the entire regolith layer to decrease with increasing subsurface roughness. Regardless it should be noted that the backscattering contribution from the subsurface is generally very small, and that this makes only a minor contribution to the total signal except for an extremely rough subsurface.

6.6. Surface Slope

[70] Since large-scale surface slopes change the local incidence angle and polarization state of the incident radar wave, they also modulate the received radar echoes and CPRs. We define the plane of incidence as the plane formed by the normal to the principle coordinates of the lunar surface $\hat{z}$ and the incident direction of the radar wave $\bar{I}_0$ (see Figure 1), and define θ_l as the large-scale surface slope in the plane of incidence, and ϕ_l as the large-scale surface slope perpendicular to this plane. Figures 12g–12i show how the polarized (OC) and depolarized (SC) radar backscattering coefficients and CPR vary with surface slope in the plane of incidence for the five scattering terms, where a positive surface slope indicates a local surface tilted toward the radar antenna and a negative value indicates a local surface tilted away from the antenna. As can be seen, areas with regional tilts toward the radar will have a stronger polarized echo strength and a weaker depolarized radar echo strength, and therefore a smaller CPR. The opposite behavior occurs for regions that are titled away from the radar antenna.

[71] As to be expected, the influence on radar echo strength caused by slopes perpendicular to the radar incidence plane ϕ_l is symmetrical with respect to $\phi_l = 0$. The variation of the polarized (OC) and depolarized (SC) radar echo strength and CPR as a function of ϕ_l is shown in Figures 12j–12l. Compared with radar echoes for no out of plane slopes, a nonnegative slope produces only a slightly smaller polarized radar echo and a slightly larger depolarized radar echo, which causes a very small increase of the CPR. Compared to in plane slopes, out of plane slopes have little effect on the received echo strengths.

[72] Impact craters are common features of the lunar surface that give rise to variations in surface slope, especially within the older highlands. Craters walls will create highlights and lowlights in the radar images that depend on the incident direction of the radar wave and the local slope of the crater walls. As an example, Figure 13a shows the surface topography of an idealized bowl-shaped crater with a radius of 3 km (generated as in *Fa et al.* [2009]). For the case where the radar moves in the vertical y direction (along track) and transmits radar waves in the x direction (cross track), Figures 13b, 13c, and 13d show our simulated polarized (OC), depolarized (SC) and CPR images associated with this crater, respectively. The surface slope at the crater center is 0, therefore a direct comparison between this and any other point shows how the local surface slopes influence the radar echo strengths and CPR. As can be seen, portions of the crater wall that tilt toward the radar have a large polarized radar echo strength and a small depolarized radar echo strength, and therefore a small CPR. The situation is opposite for those portions of the crater wall that tilt away from the radar.

[73] Figure 13a is an idealized bowl-shaped crater, and no geometric distortion effects (i.e., foreshortening, layover and shadowing) have been considered in generating Figures 13b, 13c, and 13d. For a bowl-shaped crater, shadowing effects should occur only for the incidence angles greater than 65° [*Fa et al.*, 2009]. Since most surface slopes are less than 30°, the incidence angles associated with the Chandrayaan-1 and LRO Mini-SARs are not large enough to cause shadowing effects for typical lunar features. Radar images of actual craters are expected to be much more complicated than that of Figure 13, since the distribution of buried rocks and surface roughness are expected to correlate with position in the crater as well. Finally, we note that the distribution of backscattering coefficients associated with our simple geometric crater appears to be lognormally distributed about the average value expected for a flat plane. This implies that the effects of surface slopes resulting from impact craters larger than the radar's spatial resolution can be removed by taking the average of the backscattering coefficients in log units (or dB) over an extended region. Averaging the backscattering coefficients in absolute units would bias the average value upward in comparison to that of a flat plane.

6.7. Summary

[74] From the simulation results above, we find that the most important factor that influences the radar backscattering coefficients and CPR is the radar incidence angle. Other factors that affect primarily the radar backscattering coefficients are the abundance of buried rocks, rock shape, large-scale surface slope, regolith thickness, $FeO+TiO_2$ abundance, and surface roughness. Factors that influence primarily the returned CPR are rock shape, large-scale surface slope, real part of the dielectric constant of the regolith, surface roughness, regolith thickness, and $FeO+TiO_2$ abundances. The CPR resulting solely from buried rocks does not change with regolith thickness or rock abundance, and this implies that the CPR is not sensitive to the number of the buried rocks, but is sensitive rather to the shape of the rocks (also the orientation of the buried rocks, which is assumed to be random in this study).

[75] Note that in the above calculations, the radar frequency is 2.38 GHz (S band) and the incidence angle is 35°, and that in such a radar configuration, the subsurface, subsurface-volume and volume-subsurface scattering contributions are for the most part found to be insignificant. Neglecting these contributions would only affect the backscattering coefficients and CPR by a factor of no more than 10%. However, when considering a radar frequency of 430 MHz (P band) or near-nadir incidence angles, contributions from subsurface and subsurface-volume scattering will increase and cannot be neglected.

[76] For the analysis of Earth-based and orbital radar data, several regolith parameters can be estimated using other data sets. For example, the $FeO+TiO_2$ content (and hence the loss tangent) of the lunar regolith can be obtained from gamma ray, X-ray or optical spectroscopy data [*Lucey et al.*, 2000;

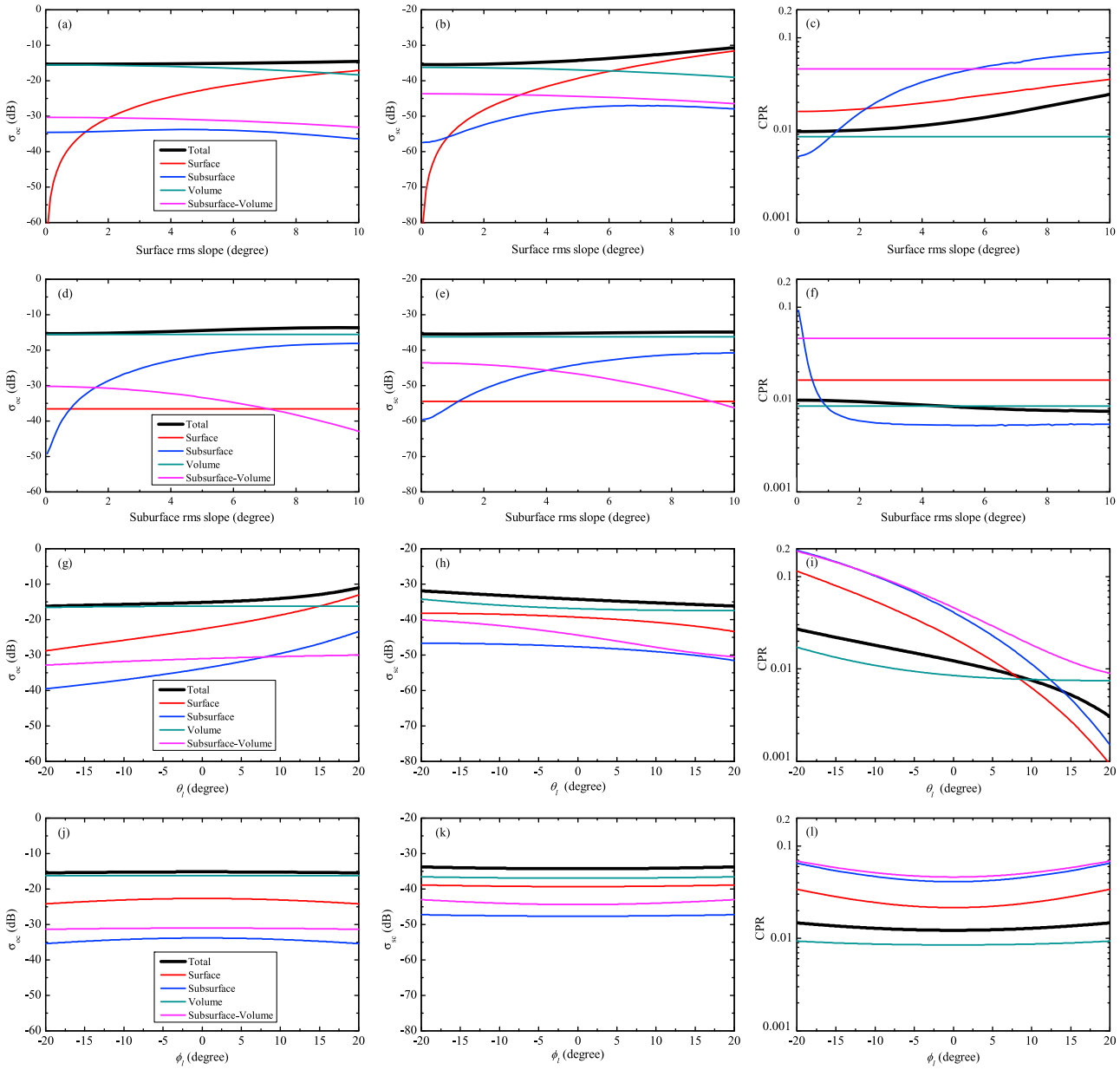

Figure 12. Plot of the polarized (σ_{oc}) and depolarized (σ_{sc}) radar backscattering coefficients and the CPR as a function of (a–c) surface roughness, (d–f) subsurface roughness, (g–i) regional in-plane surface slope θ_l, and (j–l) out-of-plane surface slope ϕ_l. The model calculations were carried out in the backscattering direction with an incidence angle 35°. The black line indicates the total contribution from the five scattering terms, the red line indicates the contribution from the lunar surface, the blue line indicates the contribution from the interface between regolith and underlying bedrock, the dark cyan line indicates the contribution from buried rocks, and the magenta line is the summed contribution from both interactions of buried rocks with the subsurface (compare with Figure 6).

Lawrence et al., 2002; *Grande et al.*, 2009], and the large-scale surface slope and roughness can be obtained by high-resolution surface topography, such as from laser altimetry [*Araki et al.*, 2009; *Huang et al.*, 2010; *Smith et al.*, 2010]. The most difficult parameters to constrain from nonradar observations are the size-frequency distribution of buried rocks, the shape of the buried rocks, the subsurface roughness, and regolith thickness. It is the investigation of these parameters where radar investigations will be the most fruitful.

7. Implications for Ice Detection Using Polarimetric SAR

[77] To investigate the possible polarimetric signatures of ice in the polar permanently shadowed areas of the Moon

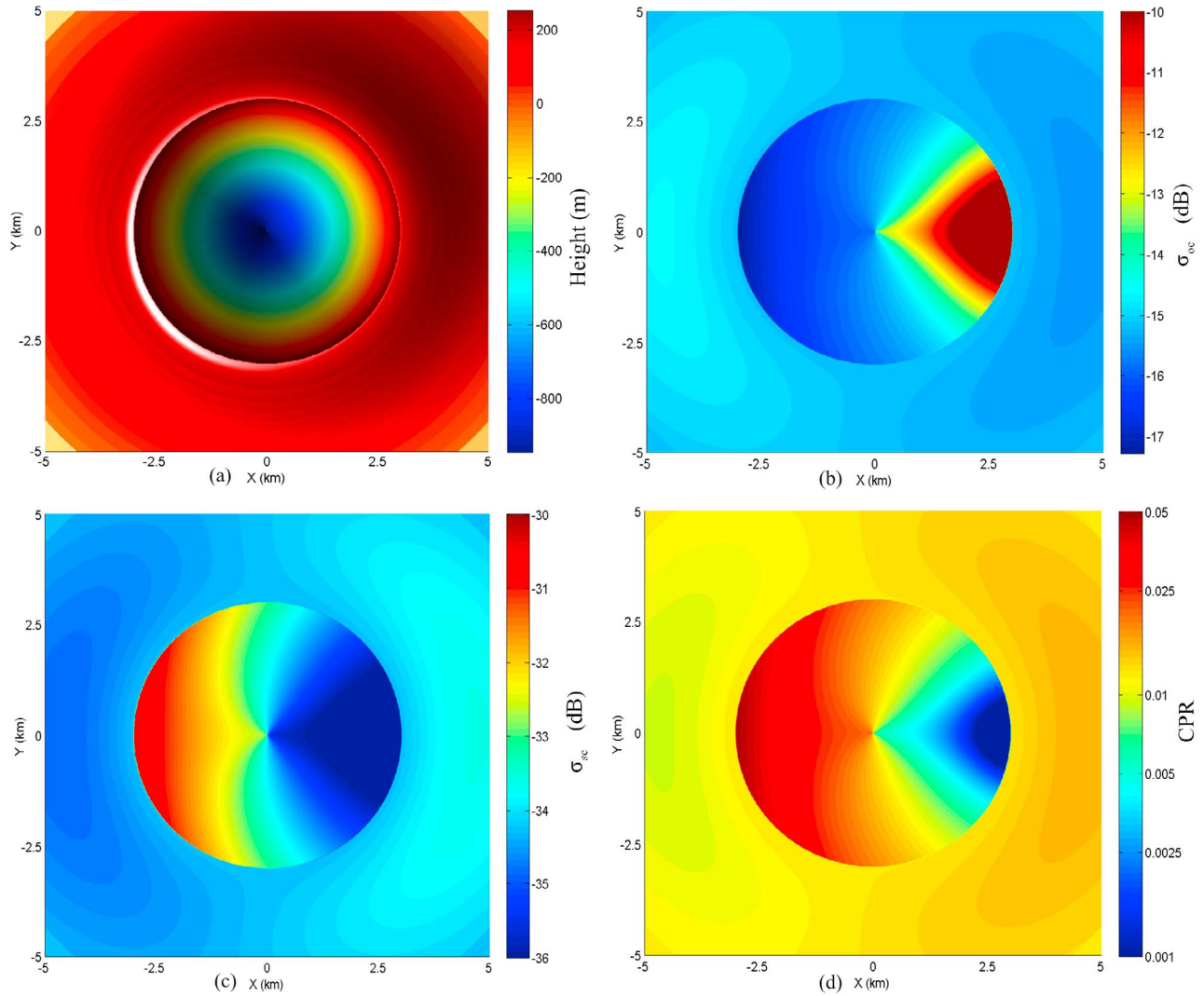

Figure 13. Influence of surface slope on radar signals for a bowl-shaped impact crater. (a) Shaded relief map of an idealized bowl-shaped crater with a 3 km radius (generated as in the work of *Fa et al.* [2009]), (b) polarized radar echo strength, (c) depolarized radar echo strength, and (d) circular polarization ratio. The radar signal is transmitted from left to right, and the model calculations were carried out in the backscattering direction with an incidence angle of 35°.

using orbital SAR, four parametric regolith models were considered. The first (nominal) model does not contain any ice, and is represented simply by a desiccated regolith with buried rocks overlying bedrock (Figure 14a). The second model contains an ice layer of thickness d with embedded rocks overlying bedrock (Figure 14b). The third model contains a regolith layer with buried rocks that overlays a pure homogenous ice "bedrock" (Figure 14c). The last model contains a regolith layer with buried ice "rocks" overlying bedrock (Figure 14d). For these models, we use a dielectric constant of $\varepsilon_{regolith} = 2.7 + i0.003$ for regolith, $\varepsilon_{ice} = 3.15 + i0.001$ for ice, and $\varepsilon_{rock} = 6.0 + i0.01$ for both buried rocks and bedrock.

[78] Figure 15 shows our predicted variations of the polarized and depolarized radar echo strengths and CPR as a function of radar incidence angle for the four different models. For the Mini-SAR instrument onboard LRO, the nominal incidence angle is 49°, whereas for the Mini-RF on Chandrayaan-1, the nominal incidence angle is 35°, as indicated by the vertical gray regions. As can be seen, given the small contrast of dielectric permittivity between ice and silicate regolith, it is difficult to discriminate the polarized and depolarized radar echoes and CPR for models shown in Figures 14a–14c. In other words, it is difficult to distinguish the nominal model where no ice is present from the model where ice is present as a thick layer with embedded rocks or the model where a regolith with embedded rocks overlays a pure ice layer. Nevertheless, if buried rocks in the regolith are simply replaced by "rocks" of ice of the same size, radar echo strengths will decrease whereas the CPR will increase at large incidence angles (>27°). While this model yields distinctive radar backscattering coefficients and CPRs, the difference between this model and the previous three is not due to the presence of ice, but rather the absence of rocks.

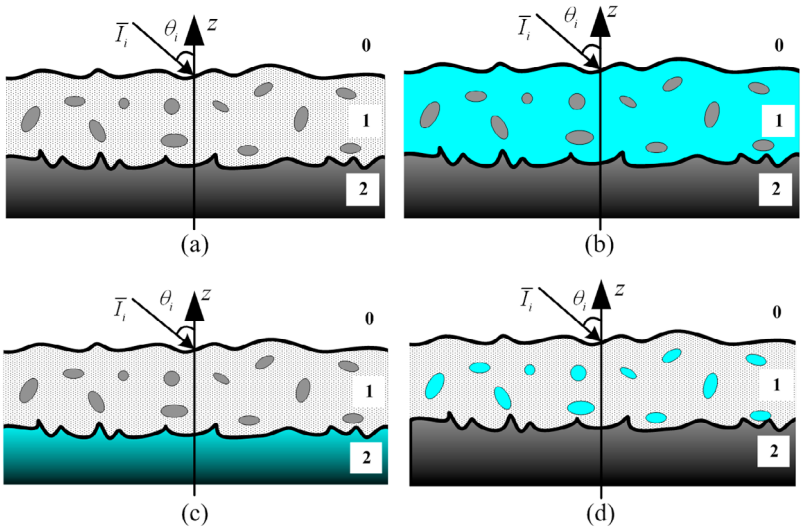

Figure 14. Four hypothetical regolith models: (a) a desiccated regolith layer with rock inclusions overlying bedrock, (b) an ice layer with rock inclusions overlying bedrock, (c) a desiccated regolith layer with rock inclusions that overlays pure homogenous ice, and (d) a regolith layer with ice inclusions overlying bedrock.

[79] Next we quantify how the dielectric constant and CPR vary as a function of the abundance of ice in the regolith for two different models. For our nominal model, the regolith is a 50:50 mixture of silicate grains and vacuum. For our first ice model, the surface layer is modeled as a pure ice layer that contains embedded silicate grains, whereas for our second ice model, the surface layer is a mixture of silicate grains, ice grains, and 50% vacuum. The size of the ice and silicate grains is assumed to be much smaller than the radar wavelength, and hence these components only act to change the effective dielectric permittivity of the regolith (or ice) layer (the effects of buried rocks will be quantified later). The complex dielectric permittivity of the mixture of ice, silicate, and vacuum ε_{mix} is calculated using Lichtenecker's mixing rule $\log\varepsilon_{\text{mix}} = \sum_{i=1}^{n} f_{vi} \log\varepsilon_i$, where ε_i and f_{vi} are the complex dielectric permittivity and fractional volume of the ith component, respectively [*Lichtenecker*, 1926; *Simpkin*, 2010]. The relative dielectric permittivity of vacuum is identically unity, and the dielectric permittivity of the ice and silicate grains is here set as $\varepsilon_{\text{ice}} = 3.15 + i0.001$ and $\varepsilon_{\text{silicate}} = 8.0 + i0.07$, respectively (the latter being the same as that of a solid rock with a density of 3.2 g/cm^3 with 5 wt.% FeO+TiO_2). Given that the maximum fractional volume that can be occupied by spherical particles is about 74% under hexagonal close packing conditions, for the mixture of pure ice and silicate grains, the minimum ice content considered is 26%.

[80] Figures 16a and 16b show the variation of the real and imaginary parts of the dielectric permittivity of the three mixtures as a function of the fractional volume of ice. The black line indicates the nominal ice-free model which is a 50:50 mixture of silicate grains and vacuum, the red line indicates the mixture of a pure ice layer with embedded silicate grains, and the blue line indicates the mixture of ice grains, silicate grains and 50% vacuum. Figure 16c shows the predicted CPRs of these three mixtures from our VRT model, for the case where there are no embedded rocks that can act as radar scatters. As can be seen, for the case of a mixture of ice grains, silicate grains and vacuum, the CPR first decreases by about 7% and then increases by a maximum of 32% as the fractional volume of ice grains increases. For the case of the mixture of a pure ice layer with silicate grains, the CPR is seen to be larger than the nominal ice-free model by 67% for 26% ice. The CPR decreases to only a 30% difference for a pure ice layer. Given the 2.5 dB uncertainty of the Mini-SAR data, and our maximum predicted signal of 67% in the CPR, the detection of ice will be challenging using the Mini-SAR data.

[81] Similar results are shown in Figure 16d, but for the case where buried rocks are also present. For these calculations, the fractional volume of the buried rocks is set to 0.1 and their size is set to 1.0 cm. The solid lines represent oblate spheroid rocks with c/a = 0.5, the dotted lines represent spherical rocks, and the dashed lines represent prolate rocks with c/a = 2.0. With large buried nonspherical rocks in a mixture of ice grains, silicate grains and 50% vacuum, the CPR increases with the fractional volume of ice grains, whereas the CPR decreases with the fractional volume of ice grains for spherical buried rocks. For the second ice model, if there are embedded nonspherical rocks, the CPRs first decrease and then increase with increasing abundances of ice, whereas the CPR monotonically decreases with the increasing of ice abundance for spherical rocks. Compared with the nominal ice-free model with a 50:50 mixture of silicate grains and vacuum, the presence of ice could cause an enhancement of CPR by several times when there are buried rocks. Nevertheless, since it is not easy to quantify the fractional volume, size and shape of buried rocks within the lunar regolith, identification of ice using solely radar CPRs will be difficult.

[82] Radar scattering from the icy Galilean satellites (Europa, Ganymede, and Callisto), the south polar ice cap of Mars, the poles of Mercury, and the Greenland ice sheet are

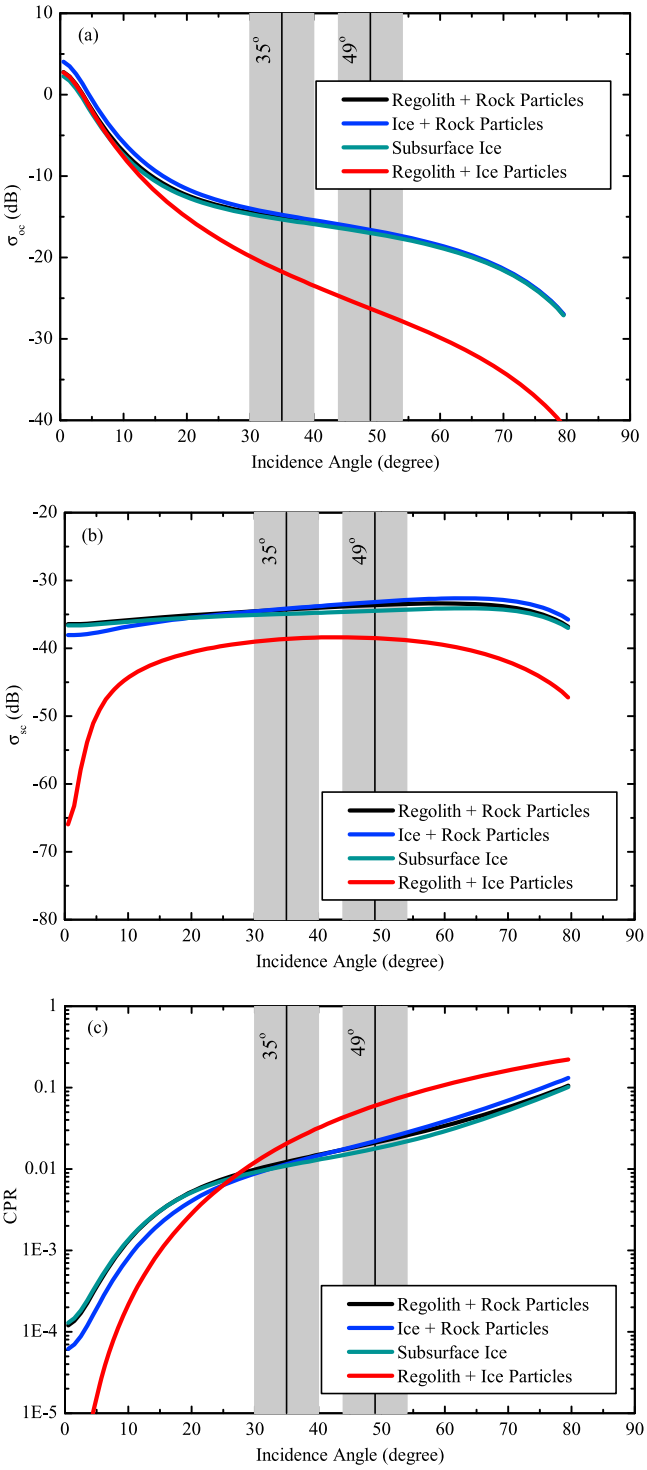

Figure 15. Radar backscattering coefficients and CPR as a function of radar incidence angle for the four regolith models shown in Figure 14: (a) polarized radar echo strength, (b) depolarized radar echo, and (c) CPR.

all characterized by unusual and unanticipated high backscattering coefficients and polarization ratios relative to the more familiar and extensively studied terrestrial planets [e.g., *Ostro and Shoemaker*, 1990; *Baron et al.*, 2003, and the references therein]. Among the various models that have been proposed to explain these "bizarre" phenomena, one of the most probable explanations is the coherent backscatter opposition effect (CBOE) that occurs near zero-phase backscattering conditions [e.g., *Hapke*, 1990; *Jin and Lax*, 1990; *Peters*, 1992]. The coherent backscatter opposition effect is traditionally explained as being caused by multiple scattering from subsurface heterogeneities that add coherently near zero-phase angles [*Hapke*, 1990]. In particular, as radar waves propagate in a weakly absorbing medium with random scatterers (such as rocks imbedded in an icy matrix, or a regolith consisting of voids), those waves that undergo random scattering along identical paths, but in opposite directions, add coherently, resulting in (at most) a twofold power increase over the diffuse background near the backscattering direction [*Hapke*, 1990]. A critical prediction of the CBOE model is that the depolarized radar return will be enhanced by no more than a factor of two at zero-phase backscattering conditions, resulting in CPRs as high as two. A test of this model would be to observe the bistatic scattering properties of the lunar surface, such as by using a radar transmitter in lunar orbit in combination with a terrestrial receiver (or vice versus). Such an experiment was attempted with the Clementine mission [*Nozette et al.*, 1996], but the interpretations of these results are ambiguous [*Simpson and Tyler*, 1999].

[83] Double scattering from a rough surface can also give rise to a coherent backscatter effect near zero-phase angles [e.g., *Jin and Lax*, 1990]. Since double scattering from a sufficiently rough surface can also account for high CPRs, the presence of CPRs higher than 1 does not necessarily imply thick deposits of nearly pure ice. Even with the CBOE effect, it will still not be easy to discriminate a coherent ice layer with a rough surface at the permanently shadowed area at the poles of the Moon. Nevertheless, by comparing the statistical properties of radar data acquired over permanently shadowed craters near the poles with more equatorial craters, it might be possible to detect an ice signature [e.g., *Spudis et al.*, 2010].

[84] Since multiple scattering between buried inclusions has not been considered in this study, our VRT model cannot account for any coherent backscatter opposition effect. Despite not taking into account multiple scattering, our model suggests that it will be very difficult for radar to detect ice mixed into the regolith. To improve our ability to detect concentrations of ices, both the radar backscattering coefficients and CPR should be analyzed simultaneously (as opposed to solely the CPR, as in the work of *Campbell et al.* [2006] and *Spudis et al.* [2010]). Fully polarimetric radar scattering theory might be another alternative to detect ice since it contains all the scattering information for any arbitrary polarization state (e.g., circular, linear and hybrid modes), which also contains more information than a single parameter of the CPR. Moreover, the use of remote sensing data sets, such as laser altimeter data and radiometer data, will be crucial to constraining the ambiguities in detecting ice.

8. Discussion and Applications

8.1. Discussion on Regolith Model

[85] In this study, the regolith was modeled as a homogeneous fine-grained layer possessing rough upper and lower interfaces, with buried rocks smaller than one wave-

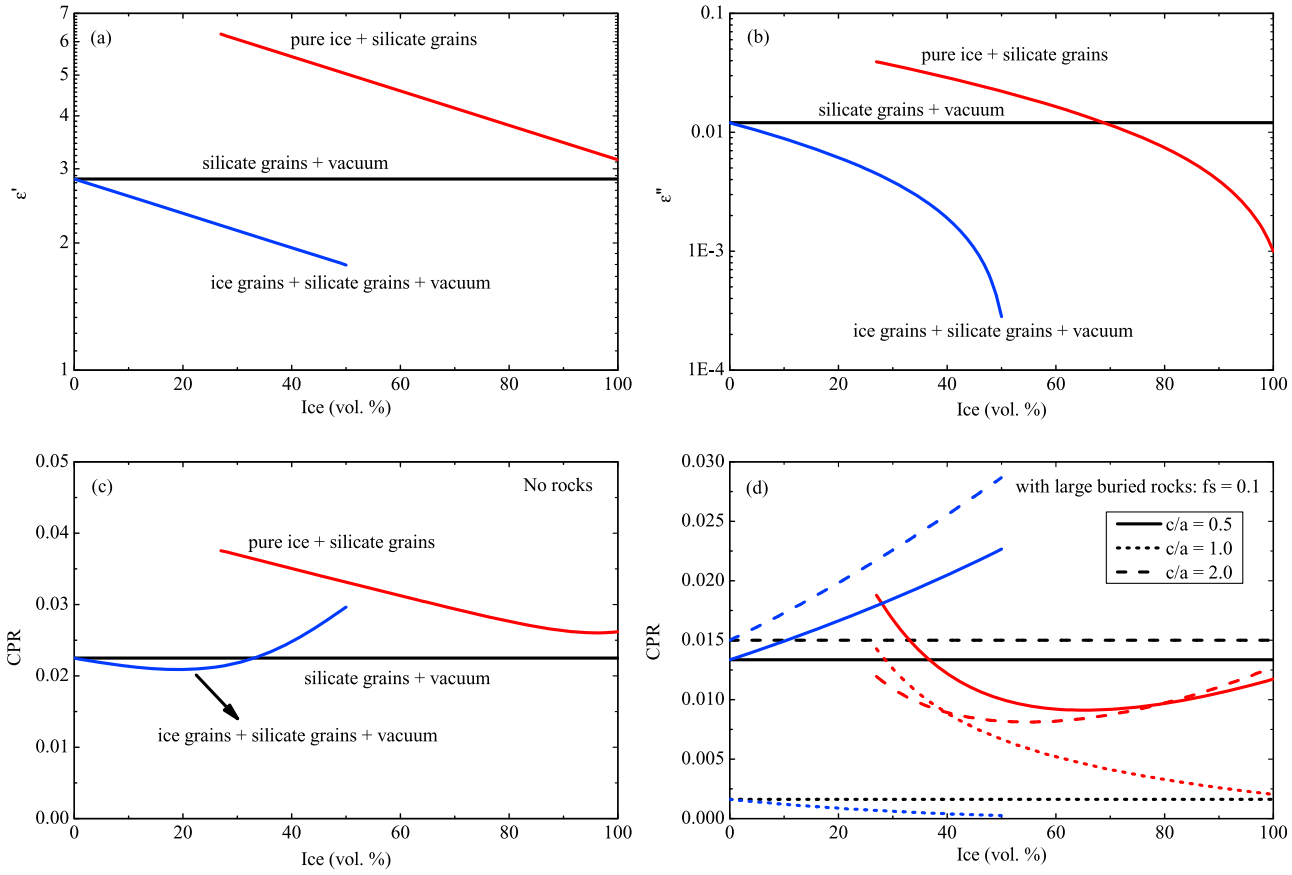

Figure 16. (a) Real and (b) imaginary parts of the dielectric permittivity as a function of ice abundance for a 50:50 mixture of silicate grains and vacuum with no ice (black line); a mixture of pure ice and silicate grains (red line); and a mixture of ice grains, silicate grains, and 50% vacuum (blue line). The complex dielectric permittivity of the mixtures is calculated using Lichtenecker's mixing rule [*Lichtenecker*, 1926; *Simpkin*, 2010]. (c) CPR of the three mixtures as a function of ice abundance and (d) CPR of the three mixtures as a function of ice abundances with the presence of buried rocks. For the latter, the fractional volume of buried rocks is 0.1 and the size of the buried rocks is 1.0 cm. The solid lines represent oblate spheroid rocks with c/a = 0.5, the dotted lines represent spherical rocks, and the dashed lines represent rocks prolate with c/a = 2.0.

length. This idealized two-layer model could be criticized in two regards. First, the lower interface between the regolith and the underlying bedrock might not be distinct, especially for the lunar highlands where a deeper megaregolith may exist [*Heiken et al.*, 1991, Figure 4.22], and second the buried rocks in the regolith layer might have a distribution of sizes, with some being comparable in size or larger than the radar wavelength. With regard to the first point, we note that scattering from the subsurface layer, as well as the scattering between rocks and the subsurface layer, generally only makes a small contribution to the observed signals. As for the second point, it would be a simple matter to include a size-frequency distribution of rocks in our model if they were all smaller than the radar wavelength. Nevertheless, for larger rock sizes, our T-matrix approach under the Rayleigh approximation [*Tsang et al.*, 2000, chap. 2] is no longer appropriate for modeling scattering from rocks, and numerical approaches, such as FDTD or MoM would have to be used.

[86] We note that most previous radar scattering models only consider either surface or volume scattering [e.g., *Hagfors*, 1964; *Campbell et al.*, 1997]. Though our model is still an idealization, it is more realistic than previous models, and in many cases can reproduce the results of these simpler scattering models. For example, if only scattering from a rough surface was considered, the integral equation model (IEM) that we used is in fact more accurate than the physical optics model of *Hagfors* [1964]. If there were no rocks buried in the regolith layer, our model would be very similar to the model of *Shkuratov and Bondarenko* [2001]. For a thick regolith layer or a higher radar frequency, the incident radar wave would not reach the subsurface. In this case, our model would be similar to the scattering model of *Campbell and Hawke* [2005], although we noticed that different approaches are used to take into account the scattering from buried rocks.

[87] Analyses of the Apollo and Luna core samples show that the majority of regolith grains fall in a relatively narrow range of sizes, with a mean particle size of 70 μm [e.g., *McKay et al.*, 1991]. At S and X band, the regolith particles are too small to act as good radar scatterers. In our model, the scattering amplitude matrix for rocks in equation (6) is

calculated using T-matrix approach under the Rayleigh approximation, which requires the rock size to be smaller than one wavelength. For the case of rocks with sizes comparable to the wavelength, the scattering amplitude function in equation (6) would have to be obtained using numerical approaches such as FDTD or the Method of Moments, though all the other parts in our VRT method would remain the same. It is to be expected that a large buried rock will enhance the radar echo strength, but that the polarization state of the received echo and therefore the CPR value would remain the same as a smaller rock with the same shape. On the other hand, if the sizes of the buried rocks were much larger than the incident wavelength, buried rocks would act as a part of regolith substrate, and their scattering behaviors could be approximated as that from a rough subsurface.

[88] If the lunar regolith contains a size-frequency distribution of buried inclusions represented by the factional volume of size f_{si}, the Mueller matrix can be written as the weighted sum of Mueller matrices for each rock size [*Jin*, 1994, chap. 4]

$$\overline{\overline{M}} = \sum_{i=1}^{n} \frac{f_{si}}{f_{st}} \overline{\overline{M}}_i \tag{21}$$

where $f_{st} = \sum_{i=1}^{n} f_{si}$ and $\overline{\overline{M}}_i$ is the Mueller matrix of the ith type of inclusions that can be calculated from equation (13), and n is the number of types of inclusions. This equation is only valid under the condition of independent scattering (the scatterers are uncorrelated and the interactions of the scattering fields can be ignored), which requires that $f_{si} < 0.1$.

[89] As we do not consider rocks that are perched on the lunar surface and multiple scattering from buried rocks in this study, the predictions of the radar echo strength from our model for young craters that possess a large number of near-surface rocks could be incorrect. It is very difficult to deal with half-buried rocks on the lunar surface using an analytical approach, and the only method that can accurately account for this is a numerical approach such as in the work of *Baron et al.* [1996] and *Ye and Jin* [2010]. Though we can treat perched rocks approximately by increasing the surface roughness in our models, our model cannot explicitly account for a difference in dielectric constant between these rocks and the underlying regolith.

[90] Our radar scattering model is based on vector radiative transfer theory and the Mueller matrix solution of equation (13) is of first order, which means that it only takes into account the scattering from the surface, the subsurface, buried inclusions in the upper layer and surface-rock interactions. Usually, these first-order scattering terms dominate the observed radar echoes, but higher-order scattering that involves more than one scattering event could possible change the polarization state of radar wave and hence the CPR (Note that in our simulations the surface-volume interaction has a high CPR value). To treat double (or multiple) scattering from a rough surface or buried rocks, we would need to derive a higher-order Mueller matrix solution using the same approach as in Appendix B. In this case, however, the Mueller matrix would be very cumbersome. The only feasible approach would be to solve numerically the VRT equation [*Liang and Jin*, 2003], which is somewhat time consuming. Since the fractional volume of buried rocks in the lunar regolith is generally less than 0.1 (except in the most extreme cases) as shown in Figure 2, multiple scattering can be ignored under the assumption of independent scattering [*Tsang et al.*, 1985, chap. 2; *Jin* 1994, chap. 8], especially for the opposite sense radar backscattering coefficient. Therefore, it is probably safe to apply this first-order scattering model to the majority of the lunar surface. However, when considering young rocky craters, the fractional volume of buried rocks can be larger than 0.1 (e.g., Surveyor 7 landing site, which is close to Tycho Crater), and our first-order solution will underestimate the radar echo strength.

8.2. Future Applications

[91] Of the various techniques used in lunar exploration, radar is by far one of the most powerful tools for obtaining lunar subsurface properties because of its superior penetration. Recently, with a renewed interest in lunar exploration, a variety of radar instruments, including the Earth-based Arecibo radar [*Campbell et al.*, 2007], the Kaguya lunar radar sounder (LRS) [*Ono et al.*, 2009], and the Mini-SARs onboard Chandrayaan-1 and LRO [*Bussey et al.*, 2007; *Spudis et al.*, 2010], with different radar techniques, frequencies and polarizations, have been used to investigate the lunar surface and subsurface properties. With the radar scattering model developed in this study, a significant range of lunar surface and subsurface properties can be studied quantitatively, such as lunar surface roughness, subsurface rock abundance, regolith thickness, and regolith dielectric properties. By quantifying these properties, it will be possible to address important geologic questions, such as the origin of dark haloed craters [*Ghent et al.*, 2005], the thickness of pyroclastic deposits [*Carter et al.*, 2009], and the distribution of impact melt on the lunar surface [*Campbell et al.*, 2010].

[92] Knowledge of the regolith thickness is important for several other reasons as well. Regolith thickness is an indication of the age of lunar surface [*McKay et al.*, 1991; *Shkuratov and Bondarenko*, 2001], the regolith contains potentially valuable resources and volatiles (helium-3) [*Fa and Jin*, 2007], and all future human activates will use regolith as building materials and shielding. Furthermore, heat flow experiments need to drill or penetrate several meters below lunar surface and this is only possible to do in the regolith. One potential application of our model is to investigate the surface roughness and subsurface rock abundance at the Apollo landing sites, where the regolith thickness and composition are known [e.g., *Nakamura et al.*, 1975]. From these estimated parameters it will be possible to invert globally for the regolith thickness using Earth-based 70 cm radar or Mini-SAR data. Although *Shkuratov and Bondarenko* [2001] obtained a global regolith map for the lunar nearside using the Earth-based Arecibo 70 cm radar image, the uncertainty in the calibration of these data combined with their simplified regolith model (it did not consider buried rocks) have limited the applicability of this technique [*Campbell*, 2002]. With newly acquired well-calibrated radar data combined with our radar scattering model, it should be possible to obtain a much more accurate regolith thickness map with higher spatial resolution.

[93] Knowledge of the variation of dielectric properties over the lunar surface and its role in surface scattering and subsurface penetration is crucial for the interpretation of radar data, radar sensor design, and landing site selection for future missions. Most of our previous knowledge about lunar dielectric properties is based on laboratory measurements of the lunar regolith samples, which were collected at only a few sites on the lunar nearside [*Olhoeft and Strangway*, 1975; *Carrier et al.*, 1991], and inferences from Earth-based and bistatic radar and radio emission observations [*Hagfors*, 1970; *Tyler and Howard*, 1973]. For smooth lunar regions with few buried rocks, such as pyroclastic deposits, the ratio of the radar echo strengths in orthogonal polarizations is sensitive to the real part of the dielectric constant. In combination with our model, the real part of the dielectric constant could potentially be estimated over large regions from orbit. The loss tangent of the same regions could then be obtained from radar observations at two different frequencies. With the derived dielectric properties, it might be possible to study how FeO and TiO_2 abundances vary with depth, which is not easily investigated using other remote sensing techniques.

[94] In summary, with the radar scattering model developed in this study and the radar data from the current missions, a variety of surface and subsurface properties can be investigated quantitatively. As other complementary geophysical and ground truth information becomes available, they can be incorporated into this model, increasing the accuracy and robustness of the results.

9. Conclusions

[95] In this study, we have developed a quantitative radar scattering model that is applicable to planetary regoliths using the vector radiative transfer (VRT) theory of random media. From this model, the transmission, attenuation, reflection and scattering of radar waves at both the lunar surface and the base of the regolith, scattering from buried rocks, and the interaction between rocks with the surface and subsurface have been taken into account. Using this model, both the radar backscattering coefficients and the circular polarization ratio (CPR) can be predicted analytically as a function of regolith parameters. Our results imply the following:

[96] 1. Polarized radar backscattering coefficients at S and X band frequencies are mostly dominated by scattering from the surface and shallow buried rocks, while the depolarized radar backscattering coefficients are dominated by scattering from buried rocks.

[97] 2. Both the polarized and depolarized radar backscattering coefficients increase as the regolith thickness increases, while the CPR decreases with an increase of regolith thickness. As a result of this, the lunar highlands, whose regolith thickness is greater by about a factor of two than the maria, should have relatively stronger radar backscattering coefficients and a relatively smaller CPR when compared to the maria, which is consistent with observations [*Thompson*, 1987; *Campbell et al.*, 2007].

[98] 3. The loss tangent of the lunar regolith increases as the abundance of $FeO+TiO_2$ increases, and this causes a decrease of the radar backscattering coefficients and an increase in the CPR. Therefore, the maria, with high $FeO+TiO_2$ content, will have relatively lower radar backscattering coefficients and higher CPRs than the highlands, which is consistent with observations.

[99] 4. Under the condition of single scattering from buried rocks, the radar backscattering coefficients increase as the abundance of buried rocks increase, while the CPR decreases as rock abundances increase.

[100] 5. Areas with regional tilts toward the radar antenna will have stronger backscattering coefficients and smaller CPRs than regions that are titled away from the radar antenna.

[101] 6. Both radar backscattering coefficients and the CPR increase as surface roughness increases. In contrast, the radar backscattering coefficients increase and the CPR decreases as subsurface roughness increases.

[102] 7. Simulation results suggest that it will be a difficult task to identify ice mixed in the lunar regolith given the small contrast of dielectric permittivity between ice and the silicate regolith.

[103] The radar scattering model in this paper will be helpful in the analysis of both Earth-based and orbital radar data, including the study of the physical properties of the lunar surface and the possible detection of ice inclusions in the permanently shadowed area at the lunar poles. The radar scattering model can be applied also to the analysis of radar data obtained from Mercury, Venus, Mars and Titan.

Appendix A: Scattering Matrix for a Rough Surface Based on IEM

[104] Analytical approaches for random rough surface scattering are usually based on Huygens' principle, where the scattering field at an observation point can be expressed in terms of fields at the boundary surface. According to the magnitude of roughness (i.e., the RMS height and correlation length) compared to the radar wavelength, two traditional approaches are the Kirchhoff approximation (KA) that is valid for gently undulating surfaces with radius of curvature larger than a wavelength and the small perturbation method (SPM) that is valid for a slightly rough surface with RMS height much smaller than the wavelength. The first approach approximates the surface fields using the tangent plane approximation, that is, the surface fields at any point of the surface are approximated by the field that would be present on the tangent plane at that point [*Tsang et al.*, 1985; *Jin*, 1994]. In SPM, the surface fields are expanded as a perturbation series, which can be obtained from the boundary conditions under the Rayleigh hypothesis [*Tsang et al.*, 1985, 2000]. The KA solution is usually applied to high-frequency waves with small incident angles, and the SPA solution is generally applied to low frequencies with large incident angles. One of the most comprehensive models to date is the integral equation method (IEM), which unites the small perturbation model for slightly rough surfaces with the Kirchhoff approximation for very rough surfaces.

[105] In the integral equation method for rough surface scattering, the tangential surface fields are split to the standard Kirchhoff surface field (the same as in the physical optics approximation) and a complementary surface field, from which the far-zone scattered field can be calculated with the Stratton-Chu integral [*Fung et al.*, 1992]. With the introduction of the complementary surface field, the tangential

surface fields are more general and accurate than the traditional physical optics approximation. According to *Fung* [1994], the bistatic single-scatter scattering coefficient matrix in the upper medium is given by

$$\bar{\bar{R}}(\theta_s,\phi_s;\pi-\theta_i,\phi_i)=\begin{bmatrix} \langle|S_{vv}|^2\rangle & \langle|S_{vh}|^2\rangle & \mathrm{Re}\langle S_{vv}S_{vh}^*\rangle & -\mathrm{Im}\langle S_{vv}S_{vh}^*\rangle \\ \langle|S_{hv}|^2\rangle & \langle|S_{hh}|^2\rangle & \mathrm{Re}\langle S_{hv}S_{hh}^*\rangle & -\mathrm{Im}\langle S_{hv}S_{hh}^*\rangle \\ 2\,\mathrm{Re}\langle S_{vv}S_{hv}^*\rangle & 2\,\mathrm{Re}\langle S_{vh}S_{hh}^*\rangle & \mathrm{Re}\langle S_{vv}S_{hh}^*+S_{vh}S_{hv}^*\rangle & \mathrm{Im}\langle S_{vh}S_{hv}^*-S_{vv}S_{hh}^*\rangle \\ 2\,\mathrm{Im}\langle S_{vv}S_{hv}^*\rangle & 2\,\mathrm{Im}\langle S_{vh}S_{hh}^*\rangle & \mathrm{Im}\langle S_{vv}S_{hh}^*+S_{vh}S_{hv}^*\rangle & \mathrm{Re}\langle S_{vv}S_{hh}^*-S_{vh}S_{hv}^*\rangle \end{bmatrix} \tag{A1}$$

where the incidence angle $\pi-\theta_i$ is defined with respected to $\hat{z}$ in Figure 1. Each of the above matrix elements has the form [*Fung*, 1994, chap. 4]

$$\langle S_{qp}S_{rs}^*\rangle=\frac{k^2}{8\pi}\exp\left[-\delta^2\left(k_z^2+k_{sz}^2\right)\right]\cdot\sum_{n=1}^{\infty}\delta^{2n}\left(I_{qp}^n I_{rs}^{n*}\right)\frac{W^{(n)}\left(k_{sx}-k_x,k_{sy}-k_y\right)}{n!} \tag{A2}$$

where

$$I_{\alpha\beta}^n=(k_{sz}+k_z)^n f_{\alpha\beta}\exp\left(-\delta^2k_zk_{sz}\right)+\frac{(k_{sz})^nF_{\alpha\beta}\left(-k_x,-k_y\right)+(k_z)^nF_{\alpha\beta}\left(-k_{sx},-k_{sy}\right)}{2} \tag{A3}$$

and where q, p, r, s, α, and β are either v or h for vertical polarization and horizontal polarization, respectively. In equation (A3), $f_{\alpha\beta}$ and $F_{\alpha\beta}$ are the Kirchhoff and the complementary field coefficients, which are used to calculate the Kirchhoff and the complementary surface fields (see *Fung et al.* [1992] for more details about their calculation). δ denotes the RMS height of the rough surface, k_x, k_y, k_z are the components of the incident wave number k in x, y and z directions, and k_{sx}, k_{sy}, k_{sz} are the components of the scattered wave number k_s in x, y and z directions. $W^{(n)}(K_x, K_y)$ is the Fourier transform of the nth power of the surface correlation function. For a Gaussian correlation function

$$C(x,y)=\exp\left(-\frac{x^2}{l_x^2}-\frac{y^2}{l_y^2}\right) \tag{A4}$$

the nth power spectrum is [*Fung*, 1994, chap. 2]

$$W^{(n)}\left(K_x,K_y\right)=\frac{l_xl_y}{2n}\exp\left(-\frac{K_x^2l_x^2+K_y^2l_y^2}{4n}\right) \tag{A5}$$

where l_x and l_y are the correlation lengths in the x and y directions, respectively. For an exponential correlation function

$$C(x,y)=\exp\left(-\frac{|x|}{l_x}-\frac{|y|}{l_y}\right) \tag{A6}$$

the nth power spectrum is [*Fung*, 1994, chap. 2]

$$W^{(n)}\left(K_x,K_y\right)=\frac{l_xl_y}{n^2}\left(1+\frac{K_x^2l_x^2+K_y^2l_y^2}{n^2}\right)^{-1.5} \tag{A7}$$

The transmission matrix $\bar{\bar{T}}$ has a similar set of expressions as equation (A1). For more discussion on the derivation of these equations, see *Fung* [1994].

Appendix B: Derivation of Five Scattering Mechanism Terms of Equation (9)

[106] The extinction matrix $\bar{\bar{\kappa}}_e(\theta, \phi)$ in equation (4) is in general not diagonal for nonspherical particles (for a sphere, the matrix $\bar{\bar{\kappa}}_e(\theta, \phi)$ reduces to a scalar κ_e). It is desirable to find a matrix $\bar{\bar{E}}(\theta, \phi)$ and its inverse matrix $\bar{\bar{E}}^{-1}(\theta, \phi)$ that diagonalize $\bar{\bar{\kappa}}_e(\theta, \phi)$ as follows [*Jin*, 1994, chap. 4]:

$$\bar{\bar{\beta}}(\theta,\phi)=\bar{\bar{E}}^{-1}(\theta,\phi)\cdot\bar{\bar{\kappa}}_e(\theta,\phi)\cdot\bar{\bar{E}}(\theta,\phi) \tag{B1}$$

where the *ith* diagonal element of $\bar{\bar{\beta}}$, which is the eigenvalue of $\bar{\bar{\kappa}}_e$, is denoted as β_i, and the matrix $\bar{\bar{E}}$ is composed of the eigenvectors of $\bar{\bar{\kappa}}_e$ [e.g., *Jin*, 1994, chap. 4].

[107] By multiplying $\bar{\bar{E}}(\theta, \phi)$ with equation (4), the vector radiative transfer equation can be expressed as

$$\cos\theta\frac{d}{dz}\bar{I}^E(\theta,\phi,z)=-\bar{\bar{\beta}}(\theta,\phi,z)\cdot\bar{I}^E(\theta,\phi,z)+\int_0^{\pi}d\theta'\sin\theta'\int_0^{2\pi}d\phi'\,\bar{\bar{P}}^E(\theta,\phi;\theta',\phi',z)\cdot\bar{I}^E(\theta',\phi',z) \tag{B2}$$

where

$$\bar{I}^E=\bar{\bar{E}}^{-1}\cdot\bar{I}\qquad\bar{\bar{P}}^E=\bar{\bar{E}}^{-1}\cdot\bar{\bar{P}}\cdot\bar{\bar{E}} \tag{B3}$$

[108] Next, we split the Stokes vector $\bar{I}^E(\theta, \phi, z)$ into the upward going $\bar{I}^E(\theta, \phi, z)$ and downward going vectors $\bar{I}^E(\pi - \theta, \phi, z)$, respectively, where $0 \le \theta \le \pi/2$, which allows equation (B2) to be written as

$$\cos\theta\frac{d}{dz}\bar{I}^E(\theta,\phi,z)=-\bar{\bar{\beta}}(\theta,\phi,z)\cdot\bar{I}^E(\theta,\phi,z)+\int_0^{\pi/2}d\theta'\sin\theta'\cdot\int_0^{2\pi}d\phi'\left[\bar{\bar{P}}^E(\theta,\phi;\theta',\phi')\cdot\bar{I}^E(\theta',\phi',z)+\bar{\bar{P}}^E(\theta,\phi;\pi-\theta',\phi')\cdot\bar{I}^E(\pi-\theta',\phi',z)\right] \tag{B4a}$$

$$-\cos\theta\frac{d}{dz}\bar{I}^E(\pi-\theta,\phi,z)=-\bar{\bar{\beta}}(\pi-\theta,\phi,z)\cdot\bar{I}^E(\pi-\theta,\phi,z)+\int_0^{\pi/2}d\theta'\sin\theta'\cdot\int_0^{2\pi}d\phi'\Big[\bar{\bar{P}}^E(\pi-\theta,\phi;\theta',\phi')\cdot\bar{I}^E(\theta',\phi',z)+\bar{\bar{P}}^E(\pi-\theta,\phi;\pi-\theta',\phi')\cdot\bar{I}^E(\pi-\theta',\phi',z)\Big] \quad \text{(B4b)}$$

We solve this equation by noting that the ordinary differential equation

$$\frac{d}{ds}I=-p(s)I+q(s) \quad \text{(B5)}$$

has the solution

$$I=Ae^{-\int p(s)ds}+e^{-\int p(s)ds}\int^s q(s')e^{\int^{s'}p(t)dt}ds' \quad \text{(B6)}$$

where A is an unknown coefficient to be determined by the boundary conditions.

[109] According to equation (B6), the upward going and downward going Stokes vectors can be written as

$$\bar{I}(\theta,\phi,z)=\bar{\bar{E}}(\theta,\phi)\bar{\bar{D}}[-\sec\theta\beta(\theta,\phi)z]\bar{A}+\sec\theta\bar{\bar{E}}(\theta,\phi)\bar{\bar{D}}[-\sec\theta\beta(\theta,\phi)z]\cdot\int_{-d}^{z}dz'\bar{\bar{D}}[\sec\theta\beta(\theta,\phi)z']\cdot\bar{\bar{E}}^{-1}(\theta,\phi)\int_0^{2\pi}d\phi'\int_0^{\pi/2}d\theta'\sin\theta'\cdot\Big[\bar{\bar{P}}(\theta,\phi;\theta',\phi')\cdot\bar{I}(\theta',\phi',z')+\bar{\bar{P}}(\theta,\phi;\pi-\theta',\phi')\cdot\bar{I}(\pi-\theta',\phi',z')\Big] \quad \text{(B7a)}$$

$$\bar{I}(\pi-\theta,\phi,z)=\bar{\bar{E}}(\pi-\theta,\phi)\bar{\bar{D}}[\sec\theta\beta(\pi-\theta,\phi)z]\bar{B}-\sec\theta\bar{\bar{E}}(\pi-\theta,\phi)\bar{\bar{D}}[\sec\theta\beta(\pi-\theta,\phi)z]\cdot\int_0^{z}dz'\bar{\bar{D}}[-\sec\theta\beta(\pi-\theta,\phi)z']\cdot\bar{\bar{E}}^{-1}(\pi-\theta,\phi)\int_0^{2\pi}d\phi'\int_0^{\pi/2}d\theta'\sin\theta'\cdot\Big[\bar{\bar{P}}(\pi-\theta,\phi;\theta',\phi')\cdot\bar{I}(\theta',\phi',z')+\bar{\bar{P}}(\pi-\theta,\phi;\pi-\theta',\phi')\cdot\bar{I}(\pi-\theta',\phi',z')\Big] \quad \text{(B7b)}$$

where $\bar{A}$ and $\bar{B}$ are unknown coefficients (four-column vectors) to be determined by the boundary conditions. Using the boundary condition (7a) and (7b), $\bar{A}$ and $\bar{B}$ can be written as

$$\bar{A}=\bar{\bar{D}}[-\sec\theta\beta(\theta,\phi)d]\bar{\bar{E}}^{-1}(\theta,\phi)\cdot\int_0^{2\pi}d\phi'\int_0^{\pi/2}d\theta'\sin\theta'\bar{\bar{R}}_{12}(\theta,\phi;\theta',\phi')\cdot\bar{I}(\pi-\theta',\phi',z=-d) \quad \text{(B8a)}$$

$$\bar{B}=\bar{\bar{E}}^{-1}(\pi-\theta,\phi)\bar{\bar{T}}_{01}(\theta,\phi;\theta_i,\phi_i)\bar{I}_0+\bar{\bar{E}}^{-1}(\pi-\theta,\phi)\int_0^{2\pi}d\phi'\int_0^{\pi/2}d\theta'\sin\theta'\cdot\bar{\bar{R}}_{10}(\theta,\phi;\theta',\phi')\cdot\bar{I}(\theta',\phi',z=0) \quad \text{(B8b)}$$

and the upward going and downward going Stokes vectors can be expressed as

$$\bar{I}(\theta,\phi,z)=\bar{\bar{E}}(\theta,\phi)\bar{\bar{D}}[-\sec\theta\beta(\theta,\phi)(z+d)]\cdot\bar{\bar{E}}^{-1}(\theta,\phi)\cdot\int_0^{2\pi}d\phi'\int_0^{\pi/2}d\theta'\sin\theta'\bar{\bar{R}}_{12}(\theta,\phi;\theta',\phi')\cdot\bar{I}(\pi-\theta',\phi',z=-d)+\sec\theta\bar{\bar{E}}(\theta,\phi)\bar{\bar{D}}[-\sec\theta\beta(\theta,\phi)z]\cdot\int_{-d}^{z}dz'\bar{\bar{D}}[\sec\theta\beta(\theta,\phi)z']\cdot\bar{\bar{E}}^{-1}(\theta,\phi)\int_0^{2\pi}d\phi'\int_0^{\pi/2}d\theta'\sin\theta'\cdot\Big[\bar{\bar{P}}(\theta,\phi;\theta',\phi')\cdot\bar{I}(\theta',\phi',z')+\bar{\bar{P}}(\theta,\phi;\pi-\theta',\phi')\cdot\bar{I}(\pi-\theta',\phi',z')\Big] \quad \text{(B9a)}$$

$$\bar{I}(\pi-\theta,\phi,z)=\bar{\bar{E}}(\pi-\theta,\phi)\bar{\bar{D}}[\sec\theta\beta(\pi-\theta,\phi)z]\cdot\bar{\bar{E}}^{-1}(\pi-\theta,\phi)\bar{\bar{T}}_{01}(\theta,\phi;\theta_i,\phi_i)\bar{I}_0+\bar{\bar{E}}(\pi-\theta,\phi)\bar{\bar{D}}[\sec\theta\beta(\pi-\theta,\phi)z]\bar{\bar{E}}^{-1}(\pi-\theta,\phi)\cdot\int_0^{2\pi}d\phi'\int_0^{\pi/2}d\theta'\sin\theta'\bar{\bar{R}}_{10}(\theta,\phi;\theta',\phi')\cdot\bar{I}(\theta',\phi',z=0)-\sec\theta\bar{\bar{E}}(\pi-\theta,\phi)\bar{\bar{D}}[\sec\theta\beta(\pi-\theta,\phi)z]\cdot\int_0^{z}dz'\bar{\bar{D}}[-\sec\theta\beta(\pi-\theta,\phi)z']\cdot\bar{\bar{E}}^{-1}(\pi-\theta,\phi)\int_0^{2\pi}d\phi'\int_0^{\pi/2}d\theta'\sin\theta'\cdot\Big[\bar{\bar{P}}(\pi-\theta,\phi;\theta',\phi')\cdot\bar{I}(\theta',\phi',z')+\bar{\bar{P}}(\pi-\theta,\phi;\pi-\theta',\phi')\cdot\bar{I}(\pi-\theta',\phi',z')\Big] \quad \text{(B9b)}$$

[110] Neglecting multiple scattering terms in equation (B8), the zeroth-order coefficients are obtained as

$$\bar{A}^0=\bar{\bar{D}}[-\sec\theta\beta(\theta,\phi)d]\bar{\bar{E}}^{-1}(\theta,\phi)\cdot\int_0^{2\pi}d\phi'\int_0^{\pi/2}d\theta'\sin\theta'\bar{\bar{R}}_{12}(\theta,\phi;\theta',\phi')\cdot\bar{\bar{E}}(\pi-\theta',\phi')\bar{\bar{D}}[-d\sec\theta'\beta(\pi-\theta',\phi')]\cdot\bar{\bar{E}}^{-1}(\pi-\theta',\phi')\bar{\bar{T}}_{01}(\theta',\phi';\theta_i,\phi_i)\bar{I}_0 \quad \text{(B10a)}$$

$$\bar{B}^0=\bar{\bar{E}}^{-1}(\pi-\theta,\phi)\bar{\bar{T}}_{01}(\theta,\phi;\theta_i,\phi_i)\bar{I}_i \quad \text{(B10b)}$$

Taking the first term of equation (B9b) as the zeroth-order solution for the downward going Stokes vector,

$$\bar{I}^0(\pi-\theta,\phi,z)=\bar{\bar{E}}(\pi-\theta,\phi)\bar{\bar{D}}[\sec\theta\beta(\pi-\theta,\phi)z]\cdot\bar{\bar{E}}^{-1}(\pi-\theta,\phi)\bar{\bar{T}}_{01}(\theta,\phi;\theta_i,\phi_i)\bar{I}_i \tag{B11a}$$

and the zeroth-order upward going Stokes vector can be obtained from equation (B9a) as

$$\begin{aligned}\bar{I}^0(\theta,\phi,z)=&\bar{\bar{E}}(\theta,\phi)\bar{\bar{D}}[-\sec\theta\beta(\theta,\phi)(z+d)]\bar{\bar{E}}^{-1}(\theta,\phi)\\&\cdot\int_0^{2\pi}d\phi'\int_0^{\pi/2}d\theta'\sin\theta'\bar{\bar{R}}_{12}(\theta,\phi;\theta',\phi')\\&\cdot\bar{\bar{E}}(\pi-\theta',\phi')\cdot\bar{\bar{D}}[-\sec\theta'\beta(\pi-\theta',\phi')d]\\&\cdot\bar{\bar{E}}^{-1}(\pi-\theta',\phi')\bar{\bar{T}}_{01}(\theta',\phi';\theta_i,\phi_i)\bar{I}_i\end{aligned} \tag{B11b}$$

Inserting equation (B10) into (B9a), we get the first-order coefficient $\bar{A}^1$ as

$$\begin{aligned}\bar{A}^1=&\bar{\bar{D}}[-\sec\theta\beta(\theta,\phi)d]\bar{\bar{E}}^{-1}(\theta,\phi)\\&\cdot\int_0^{2\pi}d\phi'\int_0^{\pi/2}d\theta'\sin\theta'\bar{\bar{R}}_{12}(\theta,\phi;\theta',\phi')\sec\theta'\bar{\bar{E}}(\pi-\theta',\phi')\\&\cdot\int_{-d}^{0}dz'\bar{\bar{D}}[-\sec\theta'\beta(\pi-\theta',\phi')(d+z')]\\&\cdot\bar{\bar{E}}^{-1}(\pi-\theta',\phi')\int_0^{2\pi}d\phi''\int_0^{\pi/2}d\theta''\sin\theta''\\&\cdot\Big[\bar{\bar{P}}(\pi-\theta',\phi';\theta'',\phi'')\cdot\bar{I}^0(\theta'',\phi'',z')\\&+\bar{\bar{P}}(\pi-\theta',\phi';\pi-\theta'',\phi'')\cdot\bar{I}^0(\pi-\theta'',\phi'',z')\Big]\end{aligned} \tag{B12}$$

and the first-order solution

$$\begin{aligned}\bar{I}^1(\theta,\phi,z)=&\bar{\bar{E}}(\theta,\phi)\bar{\bar{D}}[-\sec\theta\beta(\theta,\phi)z]\bar{A}^1\\&+\sec\theta\bar{\bar{E}}(\theta,\phi)\bar{\bar{D}}[-\sec\theta\beta(\theta,\phi)z]\\&\cdot\int_{-d}^{z}dz'\bar{\bar{D}}[\sec\theta\beta(\theta,\phi)z']\bar{\bar{E}}^{-1}(\theta,\phi)\\&\cdot\int_0^{2\pi}d\phi'\int_0^{\pi/2}d\theta'\sin\theta'\\&\cdot\Big[\bar{\bar{P}}(\theta,\phi;\theta',\phi')\cdot\bar{I}^0(\theta',\phi',z')\\&+\bar{\bar{P}}(\theta,\phi;\pi-\theta',\phi')\cdot\bar{I}^0(\pi-\theta',\phi',z')\Big]\end{aligned} \tag{B13}$$

The scattered Stokes vector at $z = 0$ in the regolith layer is thus

$$\begin{aligned}\bar{I}_s(\theta,\phi,z=0)=&\bar{I}^0(\theta,\phi,z=0)+\bar{I}^1(\theta,\phi,z=0)\\=&\bar{\bar{E}}(\theta,\phi)\bar{\bar{D}}[-\sec\theta\beta(\theta,\phi)d]\bar{\bar{E}}^{-1}(\theta,\phi)\\&\cdot\int_0^{2\pi}d\phi'\int_0^{\pi/2}d\theta'\sin\theta'\bar{\bar{R}}_{12}(\theta,\phi;\theta',\phi')\\&\cdot\bar{\bar{E}}(\pi-\theta',\phi')\bar{\bar{D}}[-\sec\theta'\beta(\pi-\theta',\phi')d]\\&\cdot\bar{\bar{E}}^{-1}(\pi-\theta',\phi')\bar{\bar{T}}_{01}(\theta',\phi';\theta_i,\phi_i)\bar{I}_i\\&+\bar{\bar{E}}(\theta,\phi)\bar{\bar{D}}[-\sec\theta\beta(\theta,\phi)d]\bar{\bar{E}}^{-1}(\theta,\phi)\\&\cdot\int_0^{2\pi}d\phi'\int_0^{\pi/2}d\theta'\sin\theta'\bar{\bar{R}}_{12}(\theta,\phi;\theta',\phi')\\&\cdot\sec\theta'\bar{\bar{E}}(\pi-\theta',\phi')\\&\cdot\int_{-d}^{0}dz'\bar{\bar{D}}[-\sec\theta'\beta(\pi-\theta',\phi')(d+z')]\\&\cdot\bar{\bar{E}}^{-1}(\pi-\theta',\phi')\int_0^{2\pi}d\phi''\int_0^{\pi/2}d\theta''\sin\theta''\\&\cdot\bar{\bar{P}}(\pi-\theta',\phi';\theta'',\phi'')\bar{\bar{E}}(\theta'',\phi'')\\&\cdot\bar{\bar{D}}[-\sec\theta''\beta(\theta'',\phi'')(z'+d)]\\&\cdot\bar{\bar{E}}^{-1}(\theta'',\phi'')\int_0^{2\pi}d\phi'''\int_0^{\pi/2}d\theta'''\sin\theta'''\\&\cdot\bar{\bar{R}}_{12}(\theta'',\phi'';\theta''',\phi''')\bar{\bar{E}}(\pi-\theta''',\phi''')\\&\cdot\bar{\bar{D}}[-\sec\theta'''\beta(\pi-\theta''',\phi''')d]\\&\cdot\bar{\bar{E}}^{-1}(\pi-\theta''',\phi''')\bar{\bar{T}}_{01}(\theta''',\phi''';\theta_i,\phi_i)\bar{I}_i\\&+\bar{\bar{E}}(\theta,\phi)\bar{\bar{D}}[-\sec\theta\beta(\theta,\phi)d]\\&\cdot\bar{\bar{E}}^{-1}(\theta,\phi)\int_0^{2\pi}d\phi'\int_0^{\pi/2}d\theta'\sin\theta'\bar{\bar{R}}_{12}(\theta,\phi;\theta',\phi')\\&\cdot\sec\theta'\int_{-d}^{0}dz\bar{\bar{E}}(\pi-\theta',\phi')\\&\cdot\bar{\bar{D}}[-\sec\theta'\beta(\pi-\theta',\phi')(d+z)]\bar{\bar{E}}^{-1}(\pi-\theta',\phi')\\&\cdot\int_0^{2\pi}d\phi''\int_0^{\pi/2}d\theta''\sin\theta''\bar{\bar{P}}(\pi-\theta',\phi';\pi-\theta'',\phi'')\\&\cdot\bar{\bar{E}}(\pi-\theta'',\phi'')\cdot\bar{\bar{D}}[\sec\theta''\beta(\pi-\theta'',\phi'')z]\\&\cdot\bar{\bar{E}}^{-1}(\pi-\theta'',\phi'')\bar{\bar{T}}_{01}(\theta'',\phi'';\theta_i,\phi_i)\bar{I}_i\\&+\sec\theta\bar{\bar{E}}(\theta,\phi)\int_{-d}^{0}dz'\bar{\bar{D}}[\sec\theta\beta(\theta,\phi)z']\bar{\bar{E}}^{-1}(\theta,\phi)\\&\cdot\int_0^{2\pi}d\phi'\int_0^{\pi/2}d\theta'\sin\theta'\bar{\bar{P}}(\theta,\phi;\theta',\phi')\bar{\bar{E}}(\theta',\phi')\\&\cdot\bar{\bar{D}}[-\sec\theta'\beta(\theta',\phi')(z'+d)]\\&\cdot\bar{\bar{E}}^{-1}(\theta',\phi')\int_0^{2\pi}d\phi''\int_0^{\pi/2}d\theta''\sin\theta''\\&\cdot\bar{\bar{R}}_{12}(\theta',\phi';\theta'',\phi'')\cdot\bar{\bar{E}}(\pi-\theta'',\phi'')\\&\cdot\bar{\bar{D}}[-\sec\theta''\beta(\pi-\theta'',\phi'')d]\bar{\bar{E}}^{-1}(\pi-\theta'',\phi'')\\&\cdot\bar{\bar{T}}_{01}(\theta'',\phi'';\theta_i,\phi_i)\bar{I}_i\\&+\sec\theta\bar{\bar{E}}(\theta,\phi)\int_{-d}^{0}dz\bar{\bar{D}}[\sec\theta\beta(\theta,\phi)z]\bar{\bar{E}}^{-1}(\theta,\phi)\\&\cdot\int_0^{2\pi}d\phi'\int_0^{2\pi}d\theta'\sin\theta'\bar{\bar{P}}(\theta,\phi;\pi-\theta',\phi')\\&\cdot\bar{\bar{E}}(\pi-\theta',\phi')\cdot\bar{\bar{D}}[\sec\theta'\beta(\pi-\theta',\phi')z]\\&\cdot\bar{\bar{E}}^{-1}(\pi-\theta',\phi')\bar{\bar{T}}_{01}(\theta',\phi';\theta_i,\phi_i)\bar{I}_i\end{aligned} \tag{B14}$$

Finally inserting equation (B14) into equation (8), we obtain the first-order upward going Stokes vector that is measured

by the radar antenna as equation (9). Theoretically, the higher-order upward going Stokes vector could be obtained using the same approach. Nevertheless, in practice, the expression would be too complicated and the only feasible way to obtain it would be numerically [*Liang and Jin*, 2003].

Appendix C: Expression of Mueller Matrix

[111] In this appendix, we give the expressions of the Muller matrices for the five scattering terms in equation (13).

$$\overline{\overline{M}}_{sur}(\theta,\phi;\pi-\theta_i,\phi_i)=\overline{\overline{R}}_{01}(\theta,\phi;\theta_i,\phi_i) \tag{C1}$$

$$\begin{aligned}\overline{\overline{M}}_{bedrock}(\theta,\phi;\pi-\theta_i,\phi_i)=&\,\overline{\overline{T}}^{n}_{10}\left(\theta,\phi;\theta_i^+,\phi_i^+\right)\overline{\overline{E}}\left(\theta_i^+,\phi_i^+\right)\\&\cdot\overline{\overline{D}}\left[-\beta\left(\theta_i^+,\phi_i^+\right)d\sec\theta_i^+\right]\\&\cdot\overline{\overline{E}}^{-1}\left(\theta_i^+,\phi_i^+\right)\overline{\overline{R}}^{c}_{12}\left(\theta_i^+,\phi_i^+;\theta_i^+,\phi_i^+\right)\\&\cdot\overline{\overline{E}}\left(\pi-\theta_i^+,\phi_i^+\right)\\&\cdot\overline{\overline{D}}\left[-\beta\left(\pi-\theta_i^+,\phi_i^+\right)d\sec\theta_i^+\right]\\&\cdot\overline{\overline{E}}^{-1}\left(\pi-\theta_i^+,\phi_i^+\right)\overline{\overline{T}}^{c}_{01}\left(\theta_i^+,\phi_i^+;\theta_i,\phi_i\right)\\&+\overline{\overline{T}}^{c}_{10}(\theta,\phi;\theta^-,\phi^-)\overline{\overline{E}}(\theta^-,\phi^-)\\&\cdot\overline{\overline{D}}[-\beta(\theta^-,\phi^-)d\sec\theta^-]\\&\cdot\overline{\overline{E}}^{-1}(\theta^-,\phi^-)\overline{\overline{R}}^{n}_{12}\left(\theta^-,\phi^-;\theta_i^+,\phi_i^+\right)\\&\cdot\overline{\overline{E}}\left(\pi-\theta_i^+,\phi_i^+\right)\\&\cdot\overline{\overline{D}}\left[-\beta\left(\pi-\theta_i^+,\phi_i^+\right)d\sec\theta_i^+\right]\\&\cdot\overline{\overline{E}}^{-1}\left(\pi-\theta_i^+,\phi_i^+\right)\overline{\overline{T}}^{c}_{01}\left(\theta_i^+,\phi_i^+;\theta_i,\phi_i\right)\\&+\overline{\overline{T}}^{c}_{10}(\theta,\phi;\theta^-,\phi^-)\overline{\overline{E}}(\theta^-,\phi^-)\\&\cdot\overline{\overline{D}}[-\beta(\theta^-,\phi^-)d\sec\theta^-]\\&\cdot\overline{\overline{E}}^{-1}(\theta^-,\phi^-)\overline{\overline{R}}^{c}_{12}(\theta^-,\phi^-;\theta^-,\phi^-)\\&\cdot\overline{\overline{E}}(\pi-\theta^-,\phi^-)\\&\cdot\overline{\overline{D}}[-\beta(\pi-\theta^-,\phi^-)d\sec\theta^-]\\&\cdot\overline{\overline{E}}^{-1}(\pi-\theta^-,\phi^-)\overline{\overline{T}}^{n}_{01}(\theta^-,\phi^-;\theta_i,\phi_i)\end{aligned} \tag{C2}$$

$$\begin{aligned}\overline{\overline{M}}_{vol}(\theta,\phi;\pi-\theta_i,\phi_i)=&\,\overline{\overline{T}}^{c}_{10}(\theta,\phi;\theta^-,\phi^-)\sec\theta^-\int_{-d}^{0}dz'\overline{\overline{E}}(\theta^-,\phi^-)\\&\cdot\overline{\overline{D}}[\beta(\theta^-,\phi^-)z'\sec\theta^-]\\&\cdot\overline{\overline{E}}^{-1}(\theta^-,\phi^-)\overline{\overline{P}}\left(\theta^-,\phi^-;\pi-\theta_i^+,\phi_i^+\right)\\&\cdot\overline{\overline{E}}\left(\pi-\theta_i^+,\phi_i^+\right)\\&\cdot\overline{\overline{D}}\left[\beta\left(\pi-\theta_i^+,\phi_i^+\right)z'\sec\theta_i^+\right]\\&\cdot\overline{\overline{E}}^{-1}\left(\pi-\theta_i^+,\phi_i^+\right)\overline{\overline{T}}^{c}_{01}\left(\theta_i^+,\phi_i^+;\theta_i,\phi_i\right)\end{aligned} \tag{C3}$$

$$\begin{aligned}\overline{\overline{M}}_{bedrock\_vol}(\theta,\phi;\pi-\theta_i,\phi_i)=&\,\overline{\overline{T}}^{c}_{10}(\theta,\phi;\theta^-,\phi^-)\sec\theta^-\int_{-d}^{0}dz'\\&\cdot\overline{\overline{E}}(\theta^-,\phi^-)\overline{\overline{D}}[\beta(\theta^-,\phi^-)z'\sec\theta^-]\\&\cdot\overline{\overline{E}}^{-1}(\theta^-,\phi^-)\overline{\overline{P}}\left(\theta^-,\phi^-;\theta_i^+,\phi_i^+\right)\\&\cdot\overline{\overline{E}}\left(\theta_i^+,\phi_i^+\right)\\&\cdot\overline{\overline{D}}\left[-\beta\left(\theta_i^+,\phi_i^+\right)(z'+d)\sec\theta_i^+\right]\\&\cdot\overline{\overline{E}}^{-1}\left(\theta_i^+,\phi_i^+\right)\cdot\overline{\overline{R}}^{c}_{12}\left(\theta_i^+,\phi_i^+;\theta_i^+,\phi_i^+\right)\\&\cdot\overline{\overline{E}}\left(\pi-\theta_i^+,\phi_i^+\right)\\&\cdot\overline{\overline{D}}\left[-\beta\left(\pi-\theta_i^+,\phi_i^+\right)d\sec\theta_i^+\right]\\&\cdot\overline{\overline{E}}^{-1}\left(\pi-\theta_i^+,\phi_i^+\right)\\&\cdot\overline{\overline{T}}^{c}_{01}\left(\theta_i^+,\phi_i^+;\theta_i,\phi_i\right)\end{aligned} \tag{C4}$$

$$\begin{aligned}\overline{\overline{M}}_{vol\_bedrock}(\theta,\phi;\pi-\theta_i,\phi_i)=&\,\overline{\overline{T}}^{c}_{10}(\theta,\phi;\theta^-,\phi^-)\overline{\overline{E}}(\theta^-,\phi^-)\\&\cdot\overline{\overline{D}}[-\beta(\theta^-,\phi^-)d\sec\theta^-]\\&\cdot\overline{\overline{E}}^{-1}(\theta^-,\phi^-)\overline{\overline{R}}^{c}_{12}(\theta^-,\phi^-;\theta^-,\phi^-)\\&\cdot\sec\theta^-\int_{-d}^{0}dz'\overline{\overline{E}}(\pi-\theta^-,\phi^-)\\&\cdot\overline{\overline{D}}[-\beta(\pi-\theta^-,\phi^-)(z'+d)\sec\theta^-]\\&\cdot\overline{\overline{E}}^{-1}(\pi-\theta^-,\phi^-)\\&\cdot\overline{\overline{P}}\left(\pi-\theta^-,\phi^-;\pi-\theta_i^+,\phi_i^+\right)\\&\cdot\overline{\overline{E}}\left(\pi-\theta_i^+,\phi_i^+\right)\\&\cdot\overline{\overline{D}}\left[\beta\left(\pi-\theta_i^+,\phi_i^+\right)z'\sec\theta_i^+\right]\\&\cdot\overline{\overline{E}}^{-1}\left(\pi-\theta_i^+,\phi_i^+\right)\overline{\overline{T}}^{c}_{01}\left(\theta_i^+,\phi_i^+;\theta_i,\phi_i\right)\end{aligned} \tag{C5}$$

where the angles (θ^-, ϕ^-) are defined to be the diffraction angle of incident wave (θ, ϕ).

Appendix D: Mueller Matrix of an Arbitrarily Oriented Rough Surface

[112] As shown in Figure D1, the reference lunar surface is given by the principal coordinate system ($\hat{x}$, $\hat{y}$, $\hat{z}$) and the tilted lunar surface is described using the local coordinates ($\hat{x}_l$, $\hat{y}_l$, $\hat{z}_l$). The relation between these two coordinate frames is described by the Euler angles (α, β, γ) [*Tsang et al.*, 1985, chap. 2; *Jin*, 1994, chap. 2], which are defined as (1) a rotation $\alpha(0 \le \alpha \le 2\pi)$ of ($\hat{x}_l$, $\hat{y}_l$) about $\hat{z}_l$, where the $\hat{y}_l$ axis becomes $\hat{y}'_l$ on the plane ($\hat{x}$, $\hat{y}$), (2) a rotation $\beta(0 \le \beta \le \pi)$ about $\hat{y}'_l$, where the $\hat{z}_l$ axis becomes $\hat{z}$ and (3) a rotation $\gamma(0 \le \gamma \le 2\pi)$ about $\hat{z}$, and the ($\hat{x}_l$, $\hat{y}_l$, $\hat{z}_l$) is rotated to ($\hat{x}$, $\hat{y}$, $\hat{z}$). In the principal coordinates, the incident wave vector is $\hat{k}_i$ with the incident angles θ_i and ϕ_i, the scattered wave vector is $\hat{k}_s$ with the scattered angles θ_s and ϕ_s. The corresponding horizontal and vertical polarization bases are $\hat{h}_i$, $\hat{v}_i$ and $\hat{h}_s$, $\hat{v}_s$, respectively. For simplicity and without loss of generality, suppose $\hat{y}_l$ lies in the plane *xoy*, and therefore $\alpha = 0$.

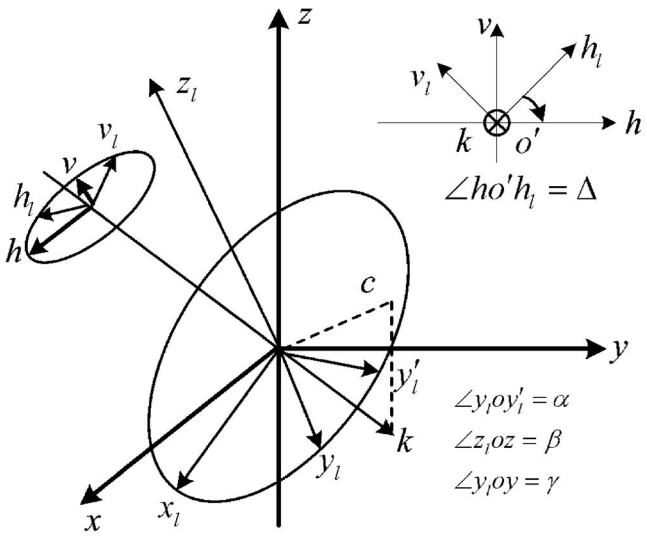

Figure D1. Rotation of polarization bases from principle coordinates ($\hat{x}$, $\hat{y}$, $\hat{z}$) to local coordinates ($\hat{x}_l$, $\hat{y}_l$, $\hat{z}_l$).

[113] In the principal and local coordinates, the incident wave vector $\hat{k}_i$ can be written as

$$\begin{aligned}\hat{k}_i &= \sin\theta_i\cos\phi_i\hat{x} + \sin\theta_i\sin\phi_i\hat{y} + \cos\theta_i\hat{z}\\ \hat{k}_i &= \sin\theta_{li}\cos\phi_{li}\hat{x} + \sin\theta_{li}\sin\phi_{li}\hat{y} + \cos\theta_{li}\hat{z}\end{aligned} \tag{D1}$$

where θ_{li} and ϕ_{li} are the incidence angles in the local coordinate system. From the geometry in Figure D1 and equation (D1), the local incident angle can be calculated as

$$\cos\theta_{li} = -\hat{k}_i\cdot\hat{z} \tag{D2}$$

$$\begin{aligned}\cos\phi_{li} = (&\sin\theta_i\cos\phi_i\cos\beta\cos\gamma - \sin\theta_i\sin\phi_i\cos\beta\sin\gamma\\ &+ \sin\beta\cos\theta_i)/\sin\theta_{li}\end{aligned} \tag{D3}$$

[114] In the principal and local coordinates, the horizontal and vertical polarization bases are defined as

$$\hat{h}_i = \frac{\hat{k}_i\times\hat{z}}{\left|\hat{k}_i\times\hat{z}\right|}, \qquad \hat{v}_i = \hat{h}_i\times\hat{k}_i \tag{D4}$$

$$\hat{h}_{li} = \frac{\hat{k}_i\times\hat{z}_l}{\left|\hat{k}_i\times\hat{z}_l\right|}, \qquad \hat{v}_{li} = \hat{h}_{li}\times\hat{k}_i \tag{D5}$$

Let Δ_i denote the angle between the different bases in the two coordinates. It can be derived from the geometrical relationships in Figure D1 that

$$\cos\Delta_i = \hat{h}\cdot\hat{h}_l = \frac{\left(\hat{k}_i\times\hat{z}\right)\left(\hat{k}_i\times\hat{z}_l\right)}{\left|\hat{k}_i\times\hat{z}\right|\left|\hat{k}_i\times\hat{z}_l\right|} = \frac{\cos\beta - \cos\theta_i\cos\theta_{li}}{\sin\theta_i\sin\theta_{li}} \tag{D6}$$

$$\mathrm{sgn}(\Delta_i) = \mathrm{sgn}\left[\left(\hat{h}_l\times\hat{h}\right)\cdot\hat{k}_i\right] = \mathrm{sgn}[\sin(\phi_i+\gamma)] \tag{D7}$$

For the scattered wave, the subscript should be changed to *s*.

[115] **Acknowledgments.** This work was supported by a CNES post-doctoral research fellowship awarded to W. Fa. The FDTD simulations were supported by NASA Planetary Geology and Geophysics Program, grant NNG05GL11G awarded to E. Heggy. The authors thank Y. Lasne at the Jet Propulsion Laboratory for providing code to generate the geometry files for our FDTD simulations, the Mini-SAR science team for many helpful discussions, and R. A. Simpson at Stanford University and an anonymous reviewer for helpful comments on the manuscript. This is IPGP contribution 2652.

References

Araki, J., et al. (2009), Lunar global shape and polar topography derived from Kaguya-LALT laser altimetry, *Science*, *323*, 897–900, doi:10.1126/science.1164146.

Baron, J. E., R. A. Simpson, and G. L. Tyler (1996), Radiowave scattering from surface and subsurface heterogeneities, *Icarus*, *122*, 383–396, doi:10.1006/icar.1996.0131.

Baron, J. E., G. L. Tyler, and R. A. Simpson (2003), Three-dimensional numerical modeling of refraction and reflection scattering from icy galilean satellites, *Icarus*, *164*, 404–417, doi:10.1016/S0019-1035(03)00124-6.

Burns, A. A. (1969), Diffuse component of lunar radar echoes, *J. Geophys. Res.*, *74*, 6553–6566, doi:10.1029/JB074i027p06553.

Bussey, D. B. J., P. D. Spudis, S. Nozette, C. L. Lichtenberg, R. K. Raney, W. Marinelli, and H. L. Winters (2007), Mini-RF: Imaging radars for exploring the lunar poles, *Lunar Planet. Sci.*, *XXXVIII*, Abstract 1610.

Campbell, B. A. (2002), Comment on "Regolith layer thickness mapping of the Moon by radar and optical data" by Y. G. Shkuratov and N. V. Bondarenko, *Icarus*, *158*, 560–561, doi:10.1006/icar.2001.6807.

Campbell, B. A., and B. R. Hawke (2005), Radar mapping of lunar cryptomaria east of Orientale basin, *J. Geophys. Res.*, *110*, E09002, doi:10.1029/2005JE002425.

Campbell, B. A., B. R. Hawke, and T. W. Thompson (1997), Regolith composition and structure in the lunar maria: Result from long-wavelength radar studies, *J. Geophys. Res.*, *102*, 19,307–19,320, doi:10.1029/97JE00858.

Campbell, B. A., D. B. Campbell, J. F. Chandler, A. A. Hine, M. C. Nolan, and P. J. Perillat (2003), Radar imaging of the lunar poles, *Nature*, *426*, 137–138, doi:10.1038/426137a.

Campbell, B. A., D. B. Campbell, J. L. Margot, R. R. Ghent, M. Nolan, J. Chandler, L. M. Carter, and N. J. S. Stacy (2007), Focused 70-cm radar mapping of the Moon, *IEEE Trans. Geosci. Remote Sens.*, *45*, 4032–4042, doi:10.1109/TGRS.2007.906582.

Campbell, B. A., B. R. Hawke, and D. B. Campbell (2009), Surface morphology of domes in the Marius Hills and Mons Rümker regions of the Moon from Earth-based radar data, *J. Geophys. Res.*, *114*, E01001, doi:10.1029/2008JE003253.

Campbell, B. A., L. M. Carter, D. B. Campbell, M. Nolan, J. Chandler, R. R. Ghent, B. R. Hawke, R. F. Anderson, and K. Wells (2010), Earth-based 12.6-cm wavelength radar mapping of the Moon: New views of impact melt distribution and mare physical properties, *Icarus*, *208*, 565–573, doi:10.1016/j.icarus.2010.03.011.

Campbell, D. B., B. A. Campbell, L. M. Carter, J. L. Margot, and N. J. S. Stacy (2006), Lunar polar ice: No evidence for thick deposits at the South Pole, *Nature*, *443*, 835–837, doi:10.1038/nature05167.

Carrier, W. D., G. R. Olhoeft, and W. Mendell (1991), Physical properties of the lunar surface, in *Lunar Source-Book: A User's Guide to the Moon*, edited by G. H. Heiken et al., pp. 530–552, Cambridge Univ. Press, New York.

Carter, L. M., B. A. Campbell, B. R. Hawke, D. B. Campbell, and M. C. Nolan (2009), Radar remote sensing of pyroclastic deposits in the Mare Serenitatis and Mare Vaporum regions of the Moon, *J. Geophys. Res.*, *114*, E11004, doi:10.1029/2009JE003406.

Cumming, W. A. (1952), The dielectric properties of ice and snow at 3.2 cm, *J. Appl. Phys.*, *23*, 768–773, doi:10.1063/1.1702299.

Evans, J. V., and T. Hagfors (1964), On the interpretation of radar reflections from the Moon, *Icarus*, *3*, 151–160, doi:10.1016/0019-1035(64)90056-9.

Evans, J. V., and G. H. Pettengill (1963), The scattering behavior of the Moon at wavelengths of 3.6, 68 and 784 centimeters, *J. Geophys. Res.*, *68*(2), 423–447, doi:10.1029/JZ068i002p00423.

Evans, S. (1965), Dielectric properties of ice and snow-a review, *J. Glaciol.*, *5*, 773–792.

Fa, W., and Y.-Q. Jin (2007), Quantitative estimation of helium-3 spatial distribution in the lunar regolith layer, *Icarus*, *190*, 15–23, doi:10.1016/j.icarus.2007.03.014.

Fa, W., and Y.-Q. Jin (2010), A primary analysis of microwave brightness temperature of lunar surface from Chang-E 1 multi-channel radiometer

observation and inversion of regolith layer thickness, *Icarus*, *207*, 605–615, doi:10.1016/j.icarus.2009.11.034.

Fa, W., F. Xu, and Y.-Q. Jin (2009), SAR imaging simulation for an inhomogeneous undulated lunar surface based on triangulated irregular network, *Sci. China, Ser. F*, *52*(4), 559–574, doi:10.1007/s11432-009-0065-1.

Fung, A. K. (1994), *Microwave Scattering and Emission Models and Their Applications*, Artech House, Boston.

Fung, A. K., Z. Li, and K. S. Chen (1992), Backscattering from a randomly rough dielectric surface, *IEEE Trans. Antennas Propag.*, *30*(2), 356–369.

Ghent, R. R., D. W. Leverington, B. A. Campbell, B. R. Hawke, and D. B. Campbell (2005), Earth-based observations of radar-dark crater haloes on the Moon: Implications for regolith properties, *J. Geophys. Res.*, *110*, E02005, doi:10.1029/2004JE002366.

Grande, M., et al. (2009), The C1XS X-ray spectrometer on Chandrayaan-1, *Planet. Space Sci.*, *57*, 717–724, doi:10.1016/j.pss.2009.01.016.

Hagfors, T. (1964), Backscattering from an undulating surface with applications to radar returns from the Moon, *J. Geophys. Res.*, *69*, 3779–3784, doi:10.1029/JZ069i018p03779.

Hagfors, T. (1967), A study of the depolarization of lunar radar echoes, *Radio Sci.*, *2*, 445–465.

Hagfors, T. (1970), Remote sensing probing of the Moon by microwave emissions and by radar, *Radio Sci.*, *5*, 189–227, doi:10.1029/RS005i002p00189.

Hapke, B. (1990), Coherent backscatter and the radar characteristics of outer planet satellites, *Icarus*, *88*, 407–417, doi:10.1016/0019-1035(90)90091-M.

Harrington, R. F. (1993), *Field Computation by Moment Methods*, IEEE Press, New York, doi:10.1109/9780470544631.

Heggy, E., S. M. Clifford, R. E. Grimm, C. L. Dinwiddie, D. Y. Wyrick, and B. E. Hill (2006), Ground-penetrating radar sounding in mafic lava flows: Assessing attenuation and scattering losses in Mars-analog volcanic terrains, *J. Geophys. Res.*, *111*, E06S04, doi:10.1029/2005JE002589.

Heiken, G. H., D. T. Vaniman, and B. M. French (Eds.) (1991), *Lunar Source-Book: A User's Guide to the Moon*, Cambridge Univ. Press, New York.

Huang, Q., J. S. Ping, M. A. Wieczorek, J. G. Yan, and X. L. Su (2010), Improved global lunar topographic model by Chang'E-1 laser altimetry data, *Lunar Planet. Sci.*, *XLI*, Abstract 1265.

Jin, Y.-Q. (1994), *Electromagnetic Scattering Modelling for Quantitative Remote Sensing*, World Sci., Hackensack, N. J.

Jin, Y.-Q. (2005), *Theory and Approach of Information Retrievals From Electromagnetic Scattering and Remote Sensing*, Springer, New York.

Jin, Y.-Q., and M. Lax (1990), Backscattering enhancement from a randomly rough surface, *Phys. Rev. B*, *42*(16), 9819–9829, doi:10.1103/PhysRevB.42.9819.

Jin, Y.-Q., F. Xu, and W. Fa (2007), Numerical simulation of polarimetric radar pulse echoes from lunar regolith layer with scatter inhomogeneity and rough interfaces, *Radio Sci.*, *42*, RS3007, doi:10.1029/2006RS003523.

Kong, J. A. (2008), *Electromagnetic Wave Theory*, EMW Publ., Cambridge, Mass.

Kuang, L., and Y.-Q. Jin (2007), Bistatic scattering from a three-dimensional object over a randomly rough surface using the FDTD algorithm, *IEEE Trans. Antennas Propag.*, *55*(8), 2302–2312, doi:10.1109/TAP.2007.901846.

Lawrence, D. J., W. C. Feldman, R. C. Elphic, R. C. Little, T. H. Prettyman, S. Maurice, P. G. Lucey, and A. B. Binder (2002), Iron abundances on the lunar surface as measured by the Lunar Prospector gamma-ray and neutron spectrometers, *J. Geophys. Res.*, *107*(E12), 5130, doi:10.1029/2001JE001530.

Liang, Z., and Y.-Q. Jin (2003), Iterative approach of high-order scattering solution for vector radiative transfer of inhomogeneous random media, *J. Quant. Spectrosc. Radiat. Transfer*, *77*(1), 1–12, doi:10.1016/S0022-4073(02)00070-5.

Lichtenecker, K. (1926), Die Dielektrizitätskonstante natürlicher und künstlicher Mischkörper, *Phys. Z.*, *27*, 115–158.

Lucey, P. G., D. T. Blewett, and B. L. Jolliff (2000), Lunar iron and titanium abundance algorithms based on final processing of Clementine ultraviolet-visible images, *J. Geophys. Res.*, *105*, 20,297–20,305, doi:10.1029/1999JE001117.

Margot, J. L., D. B. Campbell, R. F. Jurgens, and M. A. Slade (1999), Topography of the lunar poles from radar interferometry: A survey of cold trap locations, *Science*, *284*, 1658–1660, doi:10.1126/science.284.5420.1658.

McKay, D., G. Heiken, A. Basu, G. Blanford, S. Simon, R. Reedy, B. French, and J. Papike (1991), The lunar regolith, in *Lunar Source-Book: A User's Guide to the Moon*, edited by G. H. Heiken et al., pp. 285–356, Cambridge Univ. Press, New York.

Nakamura, Y., J. Dorman, F. Duennebier, D. Lammlein, and G. Latham (1975), Shallow lunar structure determined from the passive seismic experiment, *Earth Moon Planets*, *13*, 57–66, doi:10.1007/BF00567507.

Nozette, S., C. L. Lichtenberg, P. Spudis, R. Bonner, W. Ort, E. Malaret, M. Robinson, and E. M. Shoemaker (1996), The Clementine bistatic radar experiment, *Science*, *274*, 1495–1498, doi:10.1126/science.274.5292.1495.

Oberbeck, V. R., and W. L. Quaide (1967), Estimated thickness of a fragmental surface layer of Oceanus Procellarum, *J. Geophys. Res.*, *72*, 4697–4704, doi:10.1029/JZ072i018p04697.

Oberbeck, V. R., and W. L. Quaide (1968), Genetic implications of lunar regolith thickness variations, *Icarus*, *9*, 446–465, doi:10.1016/0019-1035(68)90039-0.

Olhoeft, G. R., and D. W. Strangway (1975), Dielectric properties of the first 100 meters of the Moon, *Earth Planet. Sci. Lett.*, *24*, 394–404, doi:10.1016/0012-821X(75)90146-6.

Ono, T., A. Kumamoto, H. Nakagawa, Y. Yamaguchi, S. Oshigami, A. Yamaji, T. Kobayashi, Y. Kasahara, and H. Oya (2009), Lunar radar sounder observations of subsurface layer under the nearside maria of the Moon, *Science*, *323*, 909–912, doi:10.1126/science.1165988.

Ostro, S. J., and E. M. Shoemaker (1990), The extraordinary radar echoes from Europa, Ganymede, and Gallisto: A geological perspective, *Icarus*, *85*, 335–345, doi:10.1016/0019-1035(90)90121-O.

Peters, K. J. (1992), Coherent-backscatter effect: A vector formulation accounting for polarization and absorption effects and small or large scatterers, *Phys. Rev. B*, *46*(2), 801–812, doi:10.1103/PhysRevB.46.801.

Pollack, J. B., and L. Whitehill (1972), A multiple-scattering model of the diffuse component of lunar radar echoes, *J. Geophys. Res.*, *77*, 4289–4303, doi:10.1029/JB077i023p04289.

Prettyman, T. H., J. J. Hagerty, R. C. Elphic, W. C. Feldman, D. J. Lawrence, G. W. McKinney, and D. T. Vaniman (2006), Elemental composition of the lunar surface: Analysis of gamma ray spectroscopy data from Lunar Prospector, *J. Geophys. Res.*, *111*, E12007, doi:10.1029/2005JE002656.

Qi, R.-Y., and Y.-Q. Jin (2007), Analysis of the effects of Faraday rotation on spaceborne polarimetric SAR observation at P-band, *IEEE Trans. Geosci. Remote Sens.*, *45*(5), 1115–1122, doi:10.1109/TGRS.2007.892583.

Quaide, W. L., and V. R. Oberbeck (1968), Thickness determinations of the lunar surface layer from lunar impact craters, *J. Geophys. Res.*, *73*, 5247–5270, doi:10.1029/JB073i016p05247.

Raney, R. K. (2007), Hybrid-polarity SAR architecture, *IEEE Trans. Geosci. Remote Sens.*, *45*(11), 3397–3404, doi:10.1109/TGRS.2007.895883.

Ray, R. S. (1972), Broadband complex refractive indices of ice and water, *Appl. Opt.*, *11*, 1836–1844, doi:10.1364/AO.11.001836.

Rosiwal, A. (1898), *Uber Geometrische Gestemsanalysen*, *Verh. Kaiserliche Konigliche*, Geol. Reichsanst., Vienna.

Sadiku, M. N. (1985), Refractive index of snow at microwave frequency, *Appl. Opt.*, *24*(4), 572–575, doi:10.1364/AO.24.000572.

Schaber, G. G., T. W. Thompson, and S. H. Zisk (1975), Lava flows in Mare Imbrium: An evaluation of anomalously low Earth-based radar reflectivity, *Earth Moon Planets*, *13*, 395–423, doi:10.1007/BF02626384.

Shepard, M. K., and B. A. Campbell (1999), Radar scattering from a self-affine fractal surface: Near-nadir regime, *Icarus*, *141*, 156–171, doi:10.1006/icar.1999.6141.

Shepard, M., B. Campbell, M. Bulmer, T. Farr, L. Gaddis, and J. Plaut (2001), The roughness of natural terrain: A planetary and remote sensing perspective, *J. Geophys. Res.*, *106*, 32,777–32,795, doi:10.1029/2000JE001429.

Shkuratov, Y. G., and N. V. Bondarenko (2001), Regolith layer thickness mapping of the Moon by radar and optical data, *Icarus*, *149*, 329–338, doi:10.1006/icar.2000.6545.

Shoemaker, E. M., and E. C. Morris (1968), Size-frequency distribution of fragmental debris, in Surveyor project final report, Part 2. Science results, *Tech. Rep., 32–1265*, pp. 86–102, Jet Propul. Lab., Pasadena, Calif.

Simpkin, R. (2010), Derivation of Lichtenecker's logarithmic mixture formula from Maxwell's equations, *IEEE Trans. Microwave Theory Tech.*, *58*(3), 545–550, doi:10.1109/TMTT.2010.2040406.

Simpson, R. A., and G. L. Tyler (1999), Reanalysis of Clementine bistatic radar data from the lunar south pole, *J. Geophys. Res.*, *104*, 3845–3862, doi:10.1029/1998JE900038.

Smith, D. E., et al. (2010), Initial observations from the Lunar Orbiter Laser Altimeter (LOLA), *Geophys. Res. Lett.*, *37*, L18204, doi:10.1029/2010GL043751.

Spudis, P. D., et al. (2010), Initial results for the north pole of the Moon from Mini-SAR, Chandrayaan-1 mission, *Geophys. Res. Lett.*, *37*, L06204, doi:10.1029/2009GL042259.

Stacy, N. J. S., D. B. Campbell, and P. G. Ford (1997), Arecibo radar mapping of the lunar poles: A search for ice deposits, *Science*, *276*, 1527–1530, doi:10.1126/science.276.5318.1527.

Strangway, D., G. Pearce, and G. Olhoeft (1975), Magnetic and dielectric properties of lunar samples, in *Kosmochimiya Luny i Planet*, edited by A. P. Vinogradov, pp. 712–728, Nauka, Moscow.

Thompson, T. W. (1974), Atlas of lunar radar maps at 70-cm wavelength, *Earth Moon Planets*, *10*, 87–117, doi:10.1007/BF00562019.

Thompson, T. W. (1978), High-resolution lunar radar map at 7.5 meter wavelength, *Icarus*, *36*, 174–188, doi:10.1016/0019-1035(78)90102-1.

Thompson, T. W. (1987), High-resolution lunar radar map at 70-cm wavelength, *Earth Moon Planets*, *37*, 59–70, doi:10.1007/BF00054324.

Thompson, T. W., J. B. Pollack, M. J. Campbell, and B. T. O'Leary (1970), Radar maps of the moon at 70-cm wavelength and their interpretation, *Radio Sci.*, *5*, 253–262, doi:10.1029/RS005i002p00253.

Thompson, T. W., H. Masursky, R. W. Shorthill, G. L. Tyler, and S. H. Zisk (1974), A comparison of infrared, radar and geologic mapping of lunar craters, *Earth Moon Planets*, *10*, 87–117, doi:10.1007/BF00562019.

Thompson, T. W., E. A. Ustinov, and E. Heggy (2011), Modeling radar scattering from icy lunar regoliths at 13 cm and 4 cm wavelengths, *J. Geophys. Res.*, *116*, E01006, doi:10.1029/2009JE003368.

Tsang, L., J. A. Kong, and R. Shin (1985), *Theory of Microwave Remote Sensing*, Wiley Intersci., New York.

Tsang, L., J. A. Kong, and K. H. Ding (2000), *Scattering of Electromagnetic Waves*, vol. 1, *Theory and Applications*, Wiley Intersci., New York.

Tyler, G. L., and H. T. Howard (1973), Dual-frequency bistatic-radar investigations of the Moon with Apollos 14 and 15, *J. Geophys. Res.*, *78*, 4852–4874, doi:10.1029/JB078i023p04852.

Ye, H., and Y.-Q. Jin (2010), Dual GPOF/DCIM for fast computation of Sommerfeld integrals and EM scattering from an object partially embedded in dielectric half-space, *IEEE Trans. Antennas Propag.*, *58*(5), 1801–1807.

Yee, K. S. (1966), Numerical solution of initial boundary value problems involving Maxwell's equations in isotropic media, *IEEE Trans. Antennas Propag.*, *14*(3), 302–307, doi:10.1109/TAP.1966.1138693.

Zisk, S. H. (1972), A new, earth-based radar technique for the measurement of lunar topography, *Earth Moon Planets*, *4*, 296–306.

Zisk, S. H., G. H. Pettengill, and G. W. Catuna (1974), High-resolution radar maps of the lunar surface at 3.8 cm wavelength, *Earth Moon Planets*, *10*, 17–50, doi:10.1007/BF00562017.

Zisk, S. H., C. A. Hodges, H. J. Moore, R. W. Shorthill, T. W. Thompson, E. A. Whittaker, and D. E. Wilhelms (1977), The Aristarchus-Harbinger region of the Moon: Surface geology and history from recent remote sensing observations, *Earth Moon Planets*, *17*, 59–99, doi:10.1007/BF00566853.

W. Fa and M. A. Wieczorek, Institut de Physique du Globe de Paris, Sorbonne Paris Cité, 4 Ave. de Neptune, Saint Maur des Fossés, F-94100, France. (wzfa@ipgp.fr; wieczor@ipgp.fr)

E. Heggy, Jet Propulsion Laboratory, California Institute of Technology, 4800 Oak Grove Dr., Pasadena, CA 91109-8099, USA. (essam.heggy@jpl.nasa.gov)